
High repetition rate, phase-stable, infrared OPCPA for strong-field experiments

Harald Fuest



München 2017

High repetition rate, phase-stable, infrared OPCPA for strong-field experiments

Harald Fuest

Dissertation
an der Fakultät für Physik
der Ludwig–Maximilians–Universität
München

vorgelegt von
Harald Fuest
aus Wolfenbüttel

München, den 11.08.2017

Erstgutachter: Prof. Dr. Matthias F. Kling

Zweitgutachter: Prof. Dr. Jens Limpert

Tag der mündlichen Prüfung: 25.10.2017

Light thinks it travels faster than anything but it is wrong. No matter how fast light travels, it finds the darkness has always got there first, and is waiting for it.

-Reaper Man, Discworld, Terry Pratchett

Zusammenfassung

Wenig-Zyklen, Träger-Einhüllende-Phasen (CEP) stabile Laserpulse sind ein fundamentales Werkzeug zur Untersuchung von Licht-Materie-Wechselwirkungen. Die Schlüsseltechnologie zu ihrer Erzeugung in einem großen Wellenlängenbereich ist die optisch-parametrische Verstärkung geschirpter Pulse (OPCPA), gepumpt durch intensive 1 ps Pulse. Die meisten Entwicklungen des letzten Jahrzehnts zielten auf hohe Spitzenintensitäten bei geringer Wiederholrate im nahen Infrarotbereich ab.

Demgegenüber wurde in dieser Doktorarbeit ein OPCPA-System entwickelt, das Mikrojoule Pulsenergien bei langen Wellenlängen um 2 μm und hohen Repetitionsraten von 100 kHz erzeugt. Es überwindet Limitierungen üblicher OPCPA-Designs und erreicht dadurch einzigartige Laserpuls-Parameter. Die hohe Wiederholrate macht das System vorteilhaft für Experimente mit notwendiger Aufnahmestatistik oder limitierter Pulsenergie bei geringer Signalstärke. Die Arbeit beinhaltet den Aufbau eines starken Pumpasersystems bei 100 kHz, der auch den Seed für die OPCPA erzeugt. Dieser wird auf über 10 μJ verstärkt und auf 15.5 fs komprimiert. Die CEP-Stabilität liegt bei 103 mrad auf kurzen und 136 mrad auf langen Zeitskalen. Das Design kann für verschiedene Laserquellen angepasst werden, weshalb weitere Entwicklungsmöglichkeiten beschrieben werden, die das Potential des Ansatzes zeigen.

Im zweiten Teil der Dissertation wird zunächst die Anwendbarkeit des Systems demonstriert. Die Bedeutung solcher Strahlquellen wird anschließend anhand von Laser-induzierter Elektronenbeugungs (LIED) Experimenten verdeutlicht. Diese erlauben die Untersuchung von Molekülen in der Gasphase mit hoher zeitlicher und räumlicher Auflösung, die eine direkte Beobachtung von strukturellen Veränderungen ermöglicht. Die Experimente in dieser Arbeit untersuchten die Deformation des C_{60} Fulleren in starken Feldern. Theoretische Berechnungen sagten eine Deformation entlang der Polarisationsrichtung voraus, die im Experiment direkt beobachtet wurde. Damit ist C_{60} das größte Molekül, das bisher mit LIED untersucht wurde. Des Weiteren wurden erste Pump-Probe Untersuchun-

gen durchgeführt, um einen Film der Bewegung zu erzeugen. Diese zeigen die Notwendigkeit neuer Laserquellen wie derjenigen, die in dieser Arbeit entwickelt wurde.

Abstract

Few-cycle, carrier envelope-phase (CEP) stable laser pulses are the basic tool to investigate light-matter interactions. The key technology for their generation in a broad range of wavelengths is optical parametric chirped pulse amplification (OPCPA), pumped by intense near one picosecond pulses. Most developments of the last decade were aimed at high peak powers at low repetition rates, operating in the near infrared.

In this thesis an OPCPA-system is developed, generating microjoule pulse energies at long wavelength around 2 μm and a high repetition rate of 100 kHz. It overcomes common limitations of standard OPCPA designs, resulting in unique laser pulse parameters. The high repetition rate makes it beneficial especially for experiments with statistical requirements or limited pulse energy with low signal strength. The work includes the development of a powerful table-top pump laser system operating at 100 kHz, which is also used for the seed generation. This beam is amplified to more than 10 μJ and compressed down to 15.5 fs with a CEP stability of 103 mrad short and 136 mrad long-term. As the design is applicable to different laser sources, possible further developments are theoretically investigated, showing the full potential of this approach.

In the second part of the thesis, the applicability of the OPCPA system is demonstrated. Furthermore, the importance of such laser systems is elucidated by laser induced electron diffraction (LIED). LIED permits the investigation of molecules in the gas phase with high temporal and spatial resolution, to directly observe the structural changes of molecules. The experiments undertaken within this thesis aimed at the structural deformation of the buckminsterfullerene C_{60} in strong fields. Theoretical calculations predicted a deformation along the polarization axis, that could directly be observed in the present work. In addition, C_{60} is the largest molecule successfully studied with LIED so far. First pump-probe experiments are undertaken to create a molecular movie of the deformation. These experiments illustrate the necessity to develop new laser sources, like the one described in this thesis.

Contents

Zusammenfassung	vii
Abstract	ix
1 Introduction	1
2 Pump laser system	7
2.1 Seed laser requirements of the Innoslab amplifier	7
2.2 Oscillator	8
2.3 Theoretical foundations of chirped pulse amplification	9
2.3.1 Basic considerations	9
2.3.2 Stretcher and compressor design	10
2.4 Stretcher	11
2.5 Fiber amplifier	13
2.6 Innoslab amplifier	13
2.6.1 Design	13
2.6.2 Interlock system	16
2.7 Compressor	17
3 Seed generation by optical parametric amplification	19
3.1 Supercontinuum generation	21
3.1.1 Theory	21
3.1.2 Experiment	23
3.2 Coupled wave equation	27
3.3 Simulations with SISYFOS	31
3.4 Generation of broadband 2 μm pulses	31
3.4.1 Nonlinear Optical Parametric Amplifier	32
3.4.2 Difference Frequency Generation	35
3.5 Summary	39

4	Dispersion management and CEP stabilization	41
4.1	Dispersion control and measurement	42
4.1.1	Dispersion measurement in the seed beam	43
4.1.2	Dispersion management in the main amplification stage . .	45
4.2	CEP measurement and stabilization	53
4.2.1	Theory of CEP stability	54
4.2.2	Impact on the laser design	55
4.2.3	Slow feedback loop and CEP measurement	57
4.3	Summary	58
5	First photoionization experiments with the 100 kHz system	59
5.1	Theoretical background	59
5.2	Experimental setup	62
5.3	Results	63
5.3.1	Xenon gas	63
5.3.2	Nanotips	64
5.4	Discussion	67
6	Laser induced electron diffraction of the buckminsterfullerene C₆₀	69
6.1	Gas-phase electron diffraction	70
6.2	Laser induced electron diffraction	72
6.2.1	Tunneling	72
6.2.2	The returning electron	74
6.2.3	Fixed angle broadband electron scattering	77
6.2.4	Comparison of the methods and previous work	77
6.3	Buckminsterfullerene C ₆₀	78
6.4	Experimental setup	80
6.5	Results	81
6.5.1	Angular resolved laser induced electron diffraction	81
6.5.2	Fixed-angle broadband laser-driven electron scattering . .	85
6.5.3	Dynamics	87
6.6	Discussion	88
7	Upgrades and applications of the laser system	91
7.1	Upgrades of the laser system	91
7.1.1	Towards high energies	91
7.1.2	Towards high repetition rates	93

Contents	xiii
7.1.3 Towards shorter pulse durations	94
7.2 Experiments	95
7.2.1 Nanostructures	95
7.2.2 Pump-LIED probe experiments	97
8 Conclusions	99
Bibliography	101
Data Archiving	115
List of publications	116
Acknowledgements	118

List of Figures

2.1	Scheme of the laser setup	9
2.2	Spectra of the oscillator, stretcher and fiber amplifier.	10
2.3	Stretcher and compressor design	12
2.4	M^2 -measurement of the fiber amplifier	13
2.5	Cavity of an Innoslab amplifier	14
2.6	M^2 -measurements for the Innoslab at 100 kHz	14
2.7	Beam profiles of the Innoslab amplifier	15
2.8	Scheme of the interlock system	16
2.9	Autocorrelation measurement after the grating compressor	18
2.10	Stability of the laser system	18
3.1	Scheme of the complete OPCPA setup	20
3.2	Spectrum of the supercontinuum for OPA seeding	23
3.3	Spectrum of the supercontinuum at different input energies for 1.6 ps pulses	25
3.4	Stability of the supercontinuum	26
3.5	Supercontinuum filament and beam profile	26
3.6	Thermal images of the YAG-crystal and the NOPA setup	27
3.7	Phasematching matching for collinear and noncollinear geometry	30
3.8	Pump depletion of the 1030 nm beam in the SHG	33
3.9	Simulation of the NOPA	34
3.10	Spectrum of the NOPA	35
3.11	Chirp of the NOPA in the far-field for different wavelengths	35
3.12	Simulation of the DFG process	36
3.13	Spectrum of the DFG for different BBO thicknesses	37
3.14	Power and spectral dependencies of the DFG	38
4.1	Chirp scan measurement	44
4.2	Beam profiles of the OPCPA	46
4.3	Power dependences of the unoptimized OPCPA	46

4.4	Tunability of the OPCPA for unoptimized dispersion	47
4.5	Chirped mirror design	47
4.6	FROG measurement of the unoptimized OPCPA	48
4.7	Model of the OPCPA	49
4.8	Windowed FFT for different dispersions profiles for different amounts of material	50
4.9	OPCPA spectra for different amounts of fused silica	51
4.10	FROG measurement of the optimized OPCPA	52
4.11	Power dependence from the seed for the optimized OPCPA	53
4.12	Electric field of a laser pulse	54
4.13	Alternative setup design	56
4.14	Results of the CEP measurement	57
5.1	Schemes of multiphoton ionization and above-threshold-ionization	60
5.2	Spectrum of the first DFG stage	63
5.3	Experimental setup for the photoionization experiments	64
5.4	Results on xenon gas	65
5.5	Intensity dependent photoelectron spectra for the gold nanotips .	66
5.6	Theoretical results for the nanotips experiment	66
6.1	Principle of Gas-phase electron diffraction	70
6.2	Scheme for the rescattering process	75
6.3	Radial distribution of C_{60} , obtained by GED	79
6.4	Mass spectrum of C_{60}	81
6.5	2D momentum plot for C_{60}	82
6.6	Angular dependent DCS for ASLIED	82
6.7	Results for ASLIED at 100 eV	83
6.8	DCS for ASLIED at 70-90 eV	84
6.9	Results for FABLES	86
6.10	Theoretical results of the C_{60} deformation in the laser field	87
7.1	Simulation of a final OPCPA stage with a 3 mm BBO-crystal	92
7.2	Scheme of a multichannel OPCPA	94
7.3	Scheme of the delayed emission experiment	95
7.4	Results of the LIED pump-probe measurements	96

1 Introduction

Due to its unique properties, light is nowadays the ultimate tool to investigate the nature. On the one hand, it allows to look into the depths of the universe and into the past, close to the birth of the universe. On the other hand, it is used to measure smallest distances and shortest time durations with highest precision. Light produced by lasers is one of the main discoveries of the past 50 years. Since the advent of lasers in the beginning of the 60s [1], a lot of progress has been made. Nowadays, attosecond pulse durations are available [2, 3], as well as petawatt fields [4, 5]. Together with the development of lasers, their usage has spread not only in science, but also in industry [6, 7]: Modern telecommunication is based on optical fibers, photolithography is a key process in the production of integrated circuits and in the future, laser light will probably also play a key role in the development of autonomous cars. In the fabrication process of cars, it is already important due to the unbeatable precision in micromachining.

From a scientific point of view, the development of sub-picosecond laser pulses had a great impact [8], as they allowed to investigate molecules in motion [9]. This was fundamental for the understanding of inter- and intramolecular processes like bond breaking. In 1999 the Nobel Prize in Chemistry was awarded to A. H. Zewail "for his studies of the transition states of chemical reactions using femtosecond spectroscopy" [10]. The invention of titanium-doped sapphire (Ti:Sa) as ultrabroad gain medium [11] ranging from 660 nm to 1180 nm, Kerr-lens mode locking [12], and chirped pulse amplification [13] allowed researchers to easily generate femtosecond pulses with high energies.

Ultrafast spectroscopy nowadays is not anymore limited to femtoseconds, but to attoseconds or even zeptoseconds [14]. This development was enabled by incorporating high harmonic generation (HHG), where an intense few-cycle laser interacts with a usually gaseous medium, to generate an attosecond pulse (train) at short wavelengths [15–18]. This not only allows the investigation of molecular motion but also the one of electrons and their control [19–21].

The development in laser science was one of the driving forces for strong-field physics. One of the most prominent processes here is the recollision mechanism, whereas the (semiclassical) simple man's model (SMM) delivers an intuitive understanding [22]. In the first step an atom or molecule is ionized in the electric field of a laser pulse. Afterwards, the electron is driven away from the parent ion (step two) and recollides with it in the final third step. Besides the generation of an attosecond pulse, which is a result of the recombination between electron and ion, another important process can be observed - the emission of high-energy electrons due to elastic (re-)scattering. Similar to the photons in HHG, the electrons contain information about the interacting particles, allowing insights into the temporal dynamics of the sample as well as into its structure.

Examples, where the photoelectron spectroscopy are of special interest, are metallic surfaces and nanoparticles [23–25]. In these samples, near-fields have an important influence on the electron emission from the surface, as shown in this thesis.

For gaseous media it has been shown, that the process can be used to image molecules in a way similar to standard electron diffraction [26]. This technique is called laser-induced electron diffraction (LIED) [27, 28]. The key advantage in comparison to other techniques is the high temporal resolution in combination with the high spatial resolution of a diffraction technique. Within the framework of this thesis, LIED was used for the first time for a large molecule, the buckminsterfullerene (C_{60}), giving insights into its deformation in strong laser fields.

The electron in the simple man's model, also called three step model, is driven by the electric field of the laser. Therefore, a lot of effort has been undertaken to improve the laser sources by increasing the power of the pulses or decreasing the pulse duration. In the few-cycle regime, the electric field of the laser pulse becomes important, which is defined by the carrier-envelope phase (CEP) [29–31]. Hence, the control of the CEP is very crucial for these experiments. The frequency comb technique that permitted CEP stabilization was awarded with the Nobel Prize to Theodor Hänsch and John L. Hall in 2005 [32]. Nevertheless, it is still a challenging task for the experimentalists to control and improve the different laser parameters at once. Ti:Sa based systems, which were the first lasers offering CEP control, are still widely spread, especially due to their ability to generate broad bandwidth with pulse durations down to 5 fs, while the bandwidth can be improved by the use of hollow core fibers. Such a system has been used in

the investigation of the C_{60} , where also the main drawback of this technology can be illustrated: These lasers are limited in average power. Consequently, for high pulse energies, the repetition rate has to be small, resulting in bad statistics. To overcome this problem, Ti:Sa pulses are nowadays further amplified with a second pulse, often generated by Ytterbium:Yttrium aluminum garnet (Yb:YAG) based systems [33]. These lasers exhibit a relatively long pulse duration (usually around 1 ps), but very high average powers up to the kW level, delivering the pump pulses. The energy is then transferred by optical parametric amplification (OPA) to the Ti:Sa pulses, which are the seed pulses. Those laser systems are often limited to Ti:Sa wavelength, while for strong-field physics longer wavelengths are favorable, as the energy of the electrons scales with $\propto I_L \lambda_L^2$. The quadratic dependence on the wavelength thereby underlines the importance of longer laser wavelengths. Furthermore, this design needs several electronics, like an active synchronization between the pump and the seed laser, which are complex and expensive.

These are the reasons, why a lot of effort is undertaken to find alternative designs for long wavelengths based on OPA technology. Until now, these approaches are not fulfilling one of the following criteria:

1. high pulse energy
2. high repetition rate
3. few-cycle pulses
4. CEP-stability

The second point is of special importance, since the data acquisition of the experiments is limited to the stability of the laser system. Usually after a couple of days, the laser has to be realigned, which prevents further measurements. Since high statistics are important for many strong-field experiments as shown in chapter 6, this limits the signal-to-noise ratio in the experiments.

This can be exemplified by one system that has also been used within the framework of this thesis ([34, 35], see also chapter 7 for more details). It delivers adjustable output parameters around 3 μm . The shortest pulse was 32 fs at 3.1 μm with 2 μJ , whereas the high power parameters were 55 fs (5.4 optical cycles) at 20 μJ .

Very recently, another laser setup has been published [36]. Although being quite complex due to the use of an acousto-optic programmable dispersive filter (AOPDF), the pulses are long (38.3 fs at $3.1\text{ }\mu\text{m} \approx 3.7$ optical cycles), but high in energy 40 μJ . Both systems can not entirely be compared to the one shown here, due to the longer wavelength. High repetition rate sources at around $2\text{ }\mu\text{m}$ wavelength are uncommon. One has been shown by Homann et al. [37] with similar pulse parameters, but much lower pulse energy. Other systems at this wavelength are operating at lower repetition rates [38, 39].

This thesis shows, that the requirements mentioned above can be fulfilled in a comparatively compact and simple setup. In contrast to the Ti:Sa system described before, the laser system uses only a single laser output, delivering seed and pump to generate few-cycle, CEP-stable, mid-IR pulses, whereas few-microjoule pulses are obtained within this thesis.

Structure of the thesis

The thesis is divided into two parts. In the first part (chapters 2-4) the development of a μJ -level, CEP-stable, 100 kHz system at long wavelength is described.

Chapter 2 contains the description of the developed laser setup, pointing out the important details for a stable OPA operation.

Chapter 3 is dedicated to the first nonlinear stages of the setup, which generate the mid-IR seed laser for the main amplification. This includes the seed generation via supercontinuum generation (SCG), a noncollinear optical parametric amplifier (NOPA) setup and a difference frequency generation (DFG) stage. This part also describes the fundamental theory of OPA-design.

Chapter 4 gives an overview about the more difficult aspects of OPCPAs, necessary for building a high power, few-cycle CEP-stable laser setup. Therefore, a new dispersion measurement technique is presented in this thesis. Furthermore the important features and fundamental ideas of the OPCPA design are discussed, including dispersion management and CEP-stability.

The second part addresses some applications of the presented system and gives an overview of possible improvements of the laser and the experiments.

Chapter 5 provides information about the first experiments on nanotips undertaken with the laser system.

Chapter 6 is dedicated to the LIED experiments investigating the C_{60} molecule. This work was done in collaboration with the group of Prof. Louis DiMauro at the Ohio State University (OSU), Columbus.

Chapter 7 will present possible further developments, scaling wavelength, repetition rate and pulse energy. Furthermore information about future experiments will be given.

2 Pump laser system

Nowadays, ytterbium-doped laser crystals, especially Ytterbium Doped Yttrium Aluminum Garnet (Yb:YAG), are widely spread to generate picosecond high power laser pulses [40]. These crystals are the basis for three different designs, that are competing with each other: fibers, slabs and disks. They all are capable of generating kW powers [41–43] with sub-picosecond pulse durations. Each of them is working at different repetition rates, where the disks are usually operated at kilohertz and fibers at megahertz repetition rates. Recently an exception has been published [44], where a high power, kHz repetition rate source was achievable by the combination of several amplification channels.

Nevertheless, the slab design can be placed inbetween the other two designs: Built for MHz, it can also be operated at 100 kHz, as shown in this chapter. For this repetition rate the Innoslab amplifier is still one of the most powerful sources, delivering up to 500W.

2.1 Seed laser requirements of the Innoslab amplifier

Designing such a high-power, high-repetition-rate laser system exhibits a couple of different challenges that have to be addressed: First of all, laser safety becomes a serious issue. This not only requires proper safety equipment, but also a reliable design of the whole setup. For the front-end of such a laser system, it is also important to achieve stable operation to exclude damages to the main amplifier and to run the whole setup on long time scales. In case of the Innoslab system, which is used as the pump laser source for the following stages, another problem occurs: The 100 kHz repetition rate is at the lowest limit for the amplifier, since it is designed for MHz repetition rates. This results in higher requirements on the seed laser, due to the increased pulse energy. The parameters are:

1. bandwidth 1.5-3 nm FWHM
2. central wavelength 1030 nm

3. average power 5 W
4. beam quality at the entrance of the Innoslab amplifier: $M^2 < 1.2$; for an optimal output beam profile $M^2 < 1.1$
5. pointing error $< 1/10$ of the beam diameter for frequencies > 0.1 Hz
6. beam diameter and beam divergence should not vary on short and long timescales by more than 10 %
7. the stretching factor has to be at least 250 ps/nm, ideally 500 ps/nm

To reach the high average seed power around 1030 nm, an Yb:YAG based preamplification is best suited. In the beginning of this work, it was planned to use a Ti:Sa oscillator in combination with a highly nonlinear fiber to broaden the spectrum and to generate a 1030 nm seed beam. Afterwards the pulses would have been further amplified in a regenerative disk amplifier. It turned out, that the Ti:Sa oscillator together with the highly nonlinear fiber were not stable enough to ensure a robust operation of the high power amplifier. Furthermore, the regenerative amplifier itself is a complex system, which can further decrease the stability of the whole setup. Another difficulty is the temporal stretching to at least 250 ps/nm. This makes the stretcher more than 2 m long (for details see 2.3), which in turn affects the beam pointing stability.

To overcome these problems, a new seed laser was implemented, based on an Yb:YAG fiber oscillator, followed by a fiber amplifier, where the overall setup will be described in the following.

2.2 Oscillator

As shown in figure 2.1, a turn key oscillator (Active Fiber), delivering pulses of ~ 10 nJ within ~ 10 nm bandwidth (figure 2.2) with 5 ps pulse duration, is followed by the grating stretcher and a fiber preamplifier. It is passively q-switched by a semiconductor saturable absorber mirror (SESAM) delivering pulses at 18.5 MHz repetition rate. Due to the use of the fibers the beam pointing is inherently stable and the beam quality is high ($M^2 < 1.2$ in both directions). Afterwards, an Innoslab amplifier is used as final amplification stage and the pulses are recompressed in a grating compressor.

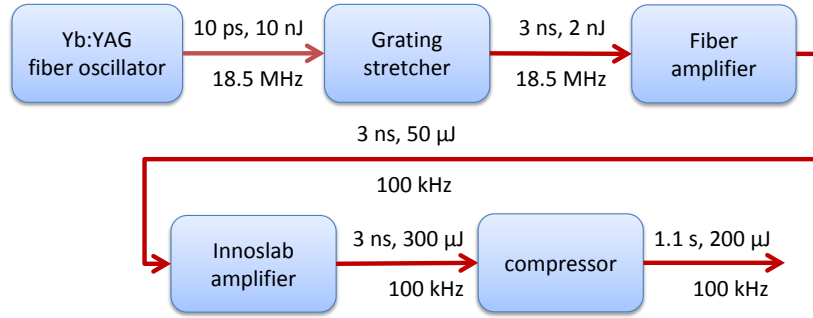


Figure 2.1: Scheme of the laser setup. The pulses of a turn-key fiber oscillator are stretched to 3 ns. These pulses are afterwards amplified in two stages: The fiber amplifier preamplifies the pulses for the Innoslab amplifier, which delivers about 300 μJ . These pulses are compressed again down to 1.1 ps.

2.3 Theoretical foundations of chirped pulse amplification

2.3.1 Basic considerations

Yb:YAG based systems deliver powerful ultrashort laser pulses. Due to the high intensities achievable within those systems, nonlinear effects have to be taken into account [45, 46]. This is described by the intensity, $I(t)$, dependent refractive index n :

$$n = n_0 + n_2 I(t), \quad (2.1)$$

where n_2 is the nonlinear refractive index. Going towards high intensities thereby leads to beam distortions due to effects like self-phase modulation (SPM) and self-focusing (SF), which will be described in more detail in chapter 3. The magnitude of these effects can be estimated by the B-Integral:

$$B = \frac{2\pi}{\lambda} \int_0^L n_2 I(z) dz, \quad (2.2)$$

which is a measure of the nonlinear phase, accumulated over propagation distance (L) of the laser pulse in the nonlinear medium. It should be kept below ~ 1 rad to avoid severe beam distortions. The value can be reduced if the peak

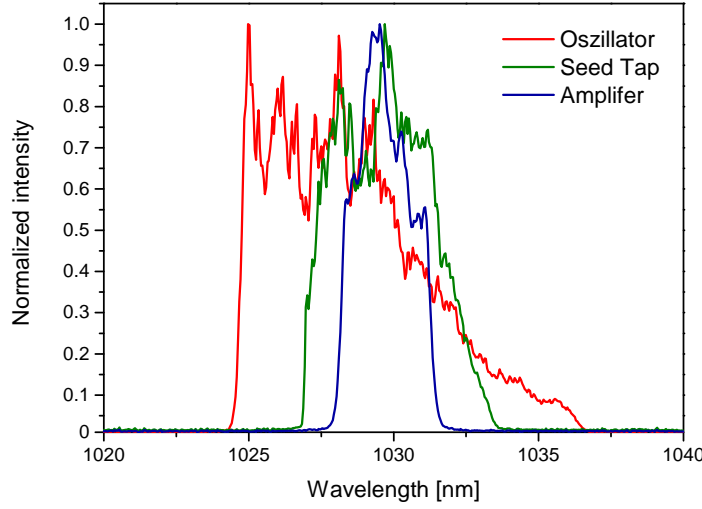


Figure 2.2: Normalized spectra of pulses from the oscillator (black), after the stretcher (red) and after the fiber amplifier (blue).

intensity is lowered, which is typically done by stretching the pulses in time. This can be achieved by modifying the phase velocity, either by introducing material into the beam path or changing the beam path length for different wavelengths. Afterwards the pulses are amplified and recompressed. This scheme is referred to as Chirped Pulse Amplification [13]. Both schemes are used in the setup, where the first one will be described in chapter 4.

The spectral phase (φ) at frequency ω can be written as a Taylor expansion:

$$\varphi(\omega) = \sum_{m=0}^{\infty} \frac{(\omega - \omega_0)^m}{m!} \left(\frac{\partial^m}{\partial \omega^m} \varphi(\omega) \right)_{\omega=\omega_0}. \quad (2.3)$$

The second term includes the so-called dispersion coefficients (D_m), where $D_1 = \frac{\partial \varphi}{\partial \omega} \big|_{\omega=\omega_0}$ is the group-delay (GD), $D_2 = \frac{\partial^2 \varphi}{\partial \omega^2} \big|_{\omega=\omega_0}$ is the group-delay dispersion (GDD) and $D_3 = \frac{\partial^3 \varphi}{\partial \omega^3} \big|_{\omega=\omega_0}$ is the third order dispersion (TOD). Higher orders are usually negligible.

2.3.2 Stretcher and compressor design

By diffracting the beam with a grating, the different wavelengths are separated. The GDD can reversibly be changed, as will be discussed in this section.

The first order diffraction of a grating is given by [47]:

$$\sin(\beta) + \sin(\alpha) = \frac{2N\pi c}{\omega}, \quad (2.4)$$

where α is the angle of incidence, β the diffraction angle, N the groove density and :

$$d = \frac{1}{N} \quad (2.5)$$

is the grating constant. If two gratings are separated by the distance b , it can be shown that the GDD for a given laser wavelength λ_l is given by:

$$GDD = -\frac{\lambda_l}{2\pi c^2} \left(\frac{\lambda_l}{d} \right)^2 \frac{b}{\cos\beta_l^3}. \quad (2.6)$$

In terms of the beam path length:

$$L_C = \frac{b}{\cos(\beta)}, \quad (2.7)$$

between the gratings it can be written as:

$$GDD = -\frac{\lambda_l}{2\pi c^2} \left(\frac{\lambda_l}{d} \right)^2 \frac{L_C}{\cos\beta_l^2}. \quad (2.8)$$

This configuration is referred to as Treacy-type compressor [48], which results in a longer beam path for longer wavelength. To reverse the GDD a telescope is used in a so called Martinez-type stretcher[49]. There the dispersion is determined by the offset (corresponding to L_C) from the focal planes of the telescope[50], as shown in figure 2.3. In this case the GDD is obtained by [46, 47]:

$$GDD = -\frac{\omega_l}{c} \left(\frac{2\pi c}{\omega_l^2 d \cos(\beta_l)} \right)^2 [L_S - 2(f_1 + f_2)] \left(\frac{f_1}{f_2} \right)^2. \quad (2.9)$$

2.4 Stretcher

As written in section 2.1, the laser pulses have to be stretched to 250 ps/nm with an optimum of 500 ps/nm, while a spectral bandwidth of 6 nm for the fiber amplifier was required. The achievable GDD was then limited by the size of the transmission grating (1740 lines/mm) and by the focal length of the lens ($f = 1,188$ m) to 1.8×10^8 fs². This corresponds to a pulse duration of 500 ps for

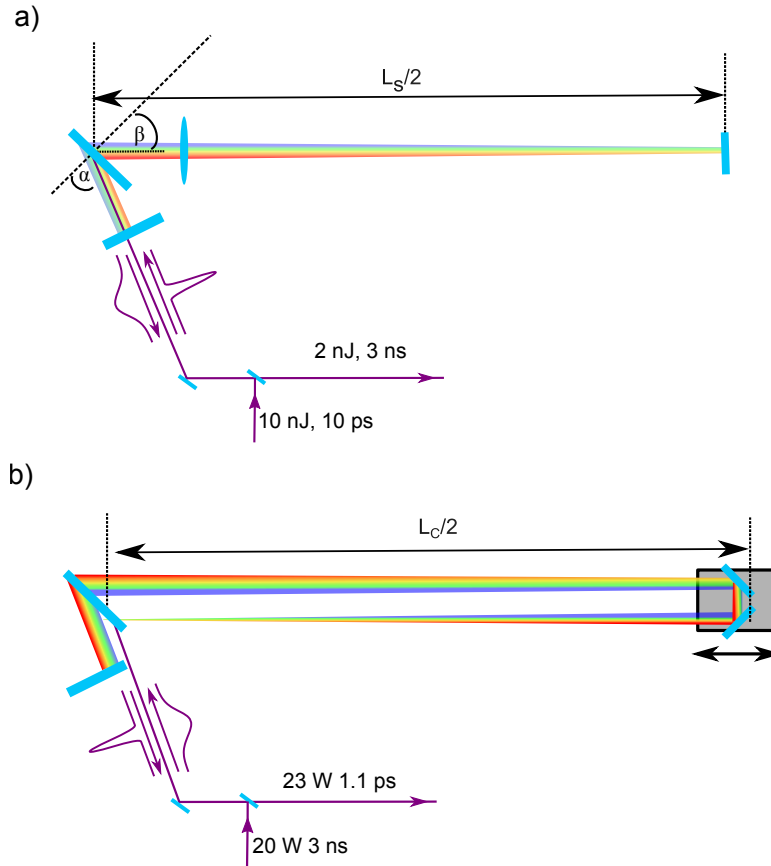


Figure 2.3: Stretcher and compressor design. a) the stretcher is shown in the folded geometry. This reduces the length of the stretcher by a factor of two. In b) the corresponding compressor is depicted.

1.5 nm bandwidth.

Due to the overall stretcher length of 2.6 m, the stretcher was folded to decrease its length, which also eliminates alignment errors between the two gratings. The incident angle was 59.5° , and the lens was placed 114 mm behind the grating. As shown in figure 2.2 the spectrum of the oscillator is cut within the stretcher. The additional bandwidth is not needed in the preamplifier and was thereby discarded to achieve a higher stretching factor. The excess bandwidth was therefore used for an interlock system, which had to be implemented during the development (for details, see section 2.6.2) as another requirement of the Innoslab amplifier.

2.5 Fiber amplifier

The stretched pulses with an energy of ~ 2 nJ are coupled with a single mode fiber into the fiber amplifier. There the pulses are first preamplified, the bandwidth is further cut and the repetition rate reduced by an acousto-optic modulator (AOM). A final amplification stage, realized in a large mode area (LMA) fiber, delivers pulse energies of up to 100 μ J at 100 kHz repetition rate, which exit the amplifier after another AOM.

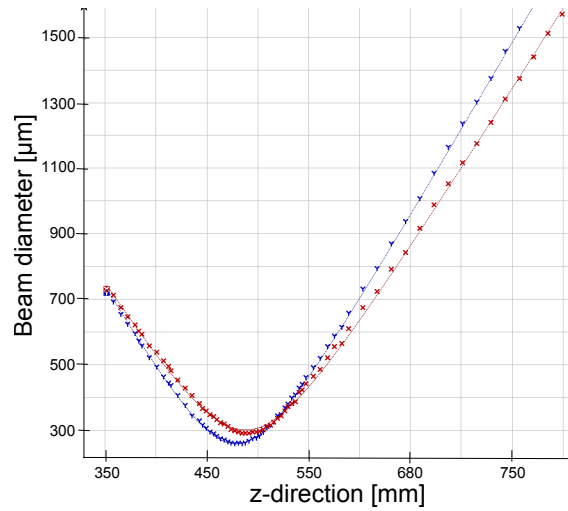


Figure 2.4: M^2 -measurement of the fiber amplifier. The measured values are 1.12 in x-direction and 1.06 in y-direction (x and y direction are indicated by the symbols).

As shown in figure 2.4, the M^2 is within the required value and the beam profile is round. The same applies to the beam stability, which was measured to be about 1/50 of the beam diameter at the position of the Innoslab crystal. It is worth to mention, that only the fiber incoupling after the stretcher has to be readjusted, less than once per week. Therefore, almost hands-off operation of the seed laser for the Innoslab is achieved.

2.6 Innoslab amplifier

2.6.1 Design

The Innoslab is a special slab laser design, initially developed by the Fraunhofer Institute for Laser Technology Aachen [51]. It delivers picosecond laser pulses at

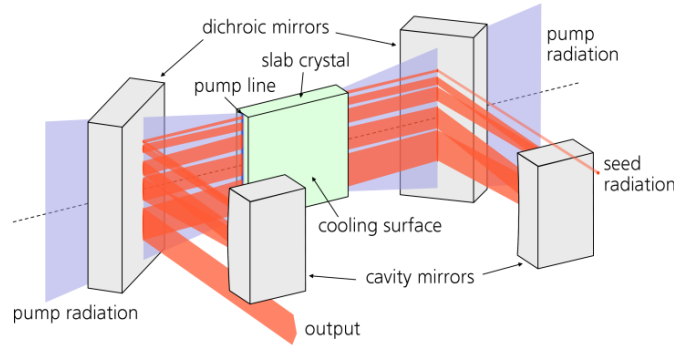


Figure 2.5: Cavity of an Innoslab amplifier: In comparison to other slab designs the pump and the seed are entering the crystal from the narrow (end) side. The seed laser is coupled in and out of the cavity by the sharp edge of the resonator mirrors, passing several times through the Yb:YAG crystal. The pump beam enters the cavity over dichroic mirrors. The picture is taken from [42].

high average power of up to 500 W. Initially developed for high repetition rates, it was reconfigured in the framework of this thesis for the operation at repetition rates down to 100 kHz.

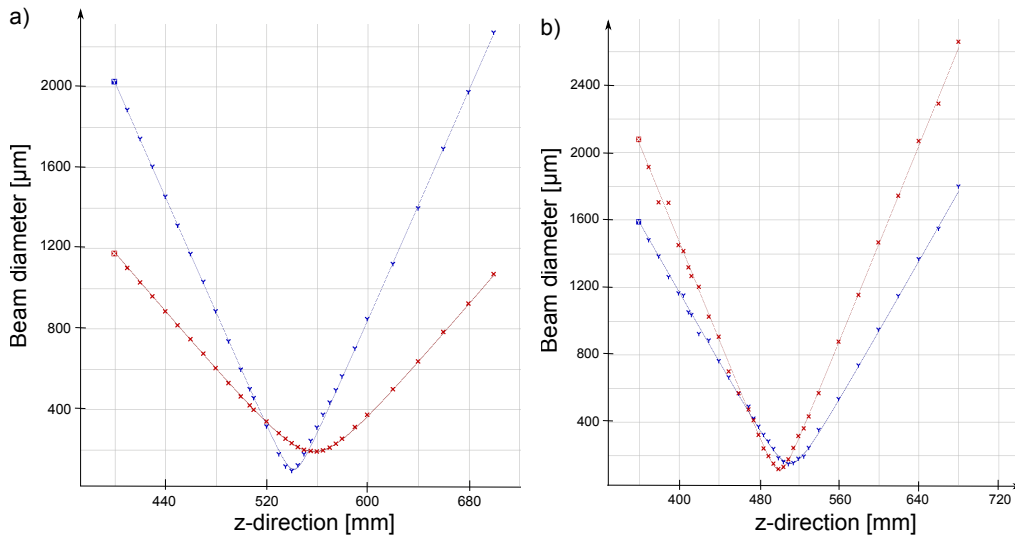


Figure 2.6: M^2 -measurements for the Innoslab at 100 kHz. The measured values for a) 30 W: x-direction: 1.08 and y-direction: 1.32 and for b) 332 W: x-direction: 1.30 and y-direction: 1.24, respectively. The left picture corresponds to the energy used in this thesis.

One specialty of the amplifier is the small cavity as shown in figure 2.5, which allows a very compact design of the system.

Furthermore, this slab-design has the advantage that the heat produced in the

crystal can be efficiently transported over a short length to the two cooling surface sides. This leads to a basically one-dimensional heat flow and thereby to a cylindrical thermal lensing effect, affecting the beam profile. It is thereby highly defined in the horizontal direction, which can be further improved by using the fast axis of the laser diode stacks [52] in this direction. The disadvantage of this design is consequently the missing beam guidance in the slow axis corresponding to the long edge of the crystal. In this direction the resonator is unstable and the beam is expanding. Nevertheless the expansion of the beam is used to keep the intensity increase of the pulses low, while working at constant saturation. This results in a very efficient design, but also a lower beam quality in the vertical direction, as shown in figure 2.6. The smaller thermal lens at lower pump energies is the reason for the astigmatism visible in the left picture.

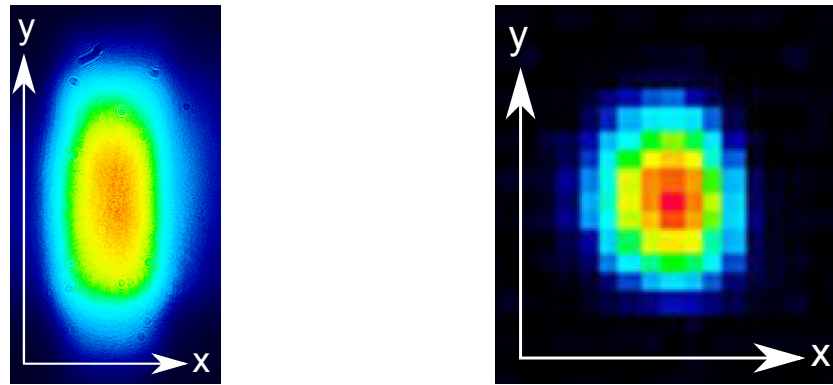


Figure 2.7: Beam profiles of the Innoslab amplifier in the near field (left) and the far field (right).

The quality in the slow axis can be improved by careful homogenization of the pump beam from the laser diode stacks. Nevertheless, a very high beam quality of the seeder is needed in this direction (for comparison, see 2.1) to obtain a good M^2 -value. Although the profile of the fiber amplifier is good, the beam profile of the Innoslab at low powers remains elongated, even after optimization in a three lens telescope (figure 2.7). More importantly for the following nonlinear stages the focus is round allowing a good amplification. In comparison to other designs, especially to regenerative amplifiers often used for disk lasers, the slab design exhibits a low B-Integral and a small amount of dispersion. Although the achievable output power higher, only 30 W were used for the OPA and first OPCPA stage.

2.6.2 Interlock system

To be able to operate the Innoslab amplifier at 100 kHz, it is crucial to implement a reliable interlock system to prevent damage to the laser. A missing pulse can potentially lead to the destruction of the system, due to the high population inversion that can built up. Therefore, the following pulse will be amplified more strongly, possibly destroying the optics or the crystal in the resonator. Similarly, also an insufficient stretching of the pulses leads to the destruction of the amplifier, due to the increased intensities of the pulses.

To avoid these problems, several seed laser parameters have to be monitored and the amplifier has to be protected from a restarting of the seed laser, after failure or stretcher misalignments. In case of the operation at 100 kHz that means, that the time between the detection of the missing pulse and the beam blocking is 100 μ s, way to short for mechanical shutters. The only possibility to block or redirect the beam are pockels-cells and AOMs, combined with fast electronics.

In the present case each pulse was monitored with photodiodes in the stretcher, as described above, at the entrance of the fiber amplifier and at its output. All photodiodes are compared to a threshold, ensuring the correct power levels of the system. The photodiodes in the stretcher thereby ensure the correct stretching of the pulses, whereas the other ones ensure the stable operation of the seed lasers. Furthermore, the beams are monitored by the Innoslab amplifier, which has its own additional interlock system.

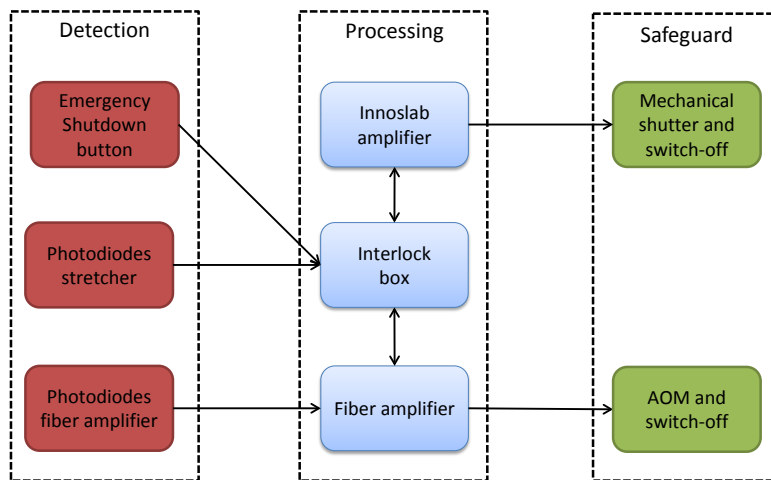


Figure 2.8: Scheme of the interlock system.

As shown in figure 2.8, the signal processing is done at three positions. The interlock box is of special importance, since it allows the communication between the different parts of the system. Nevertheless, the interlock systems of the Innoslab and fiber amplifier operate as standalone systems to increase the reliability of the setup. This solution also decreases the fast response time of the AOM, which is controlled by the fiber amplifier electronics. The system thereby controls the second AOM after the LMA fiber and allows a complete beam blocking.

In addition, the interlock box has several other input channels, including a movable emergency shutdown button to allow a fast response time, which is especially important when working with high average powers. Furthermore, this box can be used to build an automatic control system for the OPCPA and experiments in the future.

2.7 Compressor

After collimation of the beam, the Innoslab output is compressed, as depicted in figure 2.3. Like the stretcher, the compressor was folded to reduce its length down to ~ 1.1 m. A pulse duration of 1.1 ps FWHM was measured, which is close to the Fourier limit of 1.0 ps (figure 2.9). The overall energy throughput was measured to be 66%.

Due to the enclosed construction of the whole pump chain and the internal beam stabilization of the Innoslab, hands free operation of the setup is possible. Starting the system takes about 15 min, since no thermalization is needed.

Good values are also obtained for the beam-pointing and the peak-to-peak stability. Its noise can be kept below 1%, as shown in figure 2.10. The high stability of the laser chain is important for the following parametric amplification stages, since they are prone to beam instabilities, potentially leading to even higher fluctuations in the end.

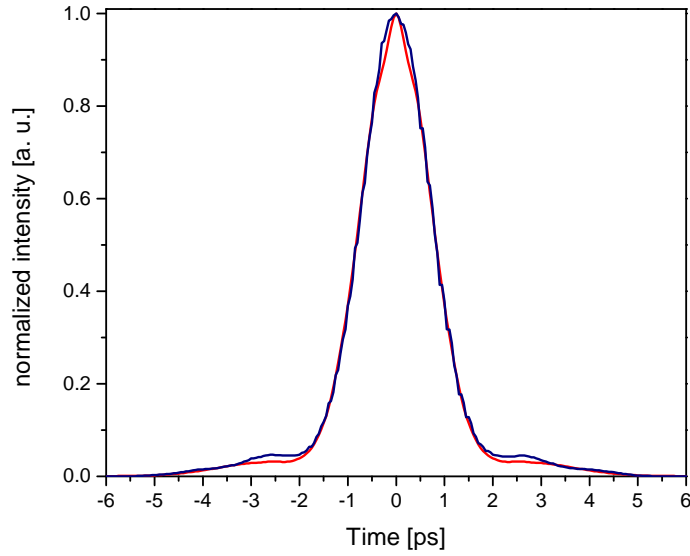


Figure 2.9: Autocorrelation measurement after the grating compressor. The measured trace (blue) fits nicely to the retrieved one (red) and corresponds to 1.1 ps FWHM.

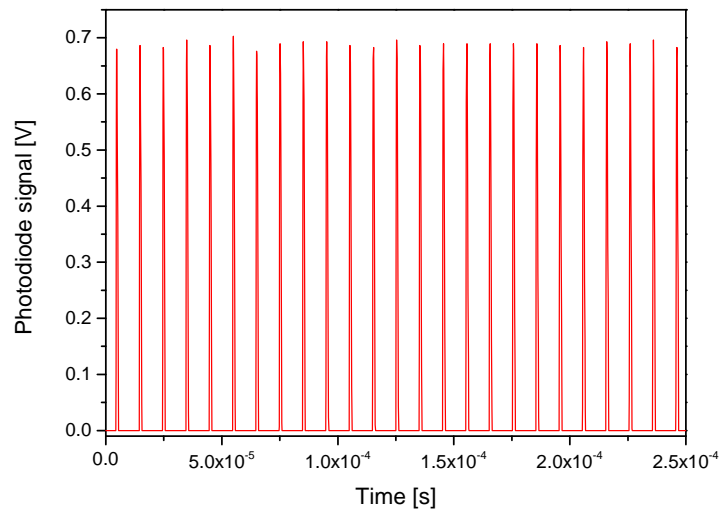


Figure 2.10: Stability of the laser system measured after the compressor. The peak to peak stability is below 1%. Similar results were obtained on long timescales.

3 Seed generation by optical parametric amplification

Optical parametric amplifiers (OPA) have a couple of advantages compared to laser amplifiers. The most important ones are:

1. The broad bandwidth, that can be achieved in different wavelength regions, when the geometry of the interaction and the crystal are chosen properly.
2. The gain, that can reach up to 6 orders of magnitude within a short crystal. An efficiency around 30% can be achieved [40].
3. The thermal load is significantly reduced.

These properties make OPAs an excellent tool for generating pulses for strong-field experiments. Especially in wavelength regions that are not accessible to laser amplification, intense few-cycle pulses can be obtained. In addition, OPAs can boost the energy of pulses generated in laser amplifiers, as it was shown in chapter 1 for Ti:Sa front-ends. Nevertheless, there are also some drawbacks to the parametric systems widely spread nowadays.

The main challenges for high power, few-cycle OPAs are usually the complex laser systems and the electronics. For example the usage of active synchronizations [53, 54] between pump and seed and the acousto-optic programmable dispersive filters (AOPDF) make the setups complicated and expensive. The latter one also limited the repetition rates until recently to less than 100 kHz.

Going towards higher repetition rates, typical techniques for broadband seed generation, like XPW [55, 56] and hollow core fibers (as described in the introduction) are not favorable due to their high demands on intensity. Additionally, these methods themselves don't lead to carrier envelope phase (CEP) stable pulses (for more details see chapter 4).

Nonetheless, high repetition rate OPCPAs have been published. Most of them are not CEP stabilized at all [57–59] or above 400 mrad on long time scales [60,

61]. Furthermore, the majority of them work at near-IR wavelength ($<1.5 \mu\text{m}$), while there is still a lack of lasers in the mid-IR for strong-field experiments. Long wavelength, high-repetition rate OPCPA's are rare and often too long in pulse duration, that CEP-effects can be observed in the experiments [34, 62]. An exception has recently been published, using a cutting-edge acousto-optic programmable dispersive filters (AOPDFs) [36]. Nevertheless, the pulses reported there are still relatively long (above three cycles).

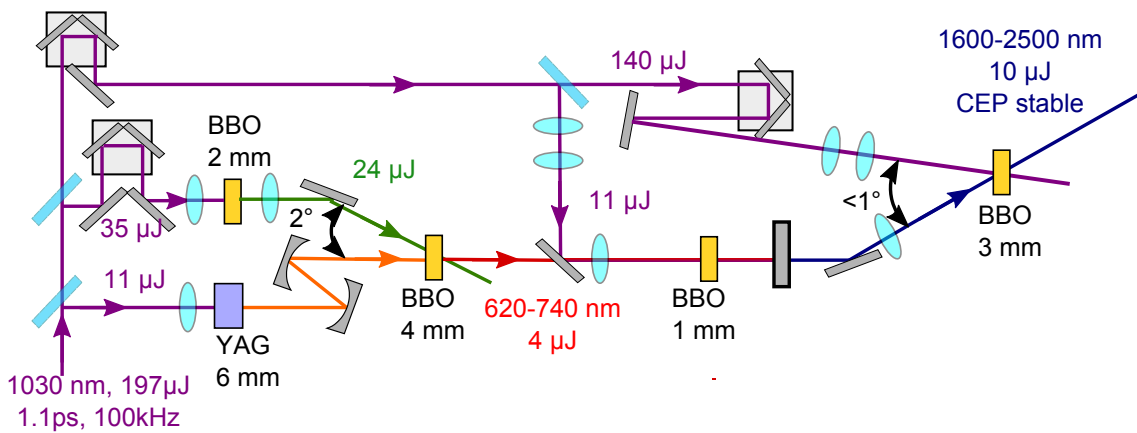


Figure 3.1: Scheme of the complete setup. In the beginning, the beam from the compressor is divided into four parts. 11 μJ generate a supercontinuum in a YAG crystal, which delivers the seed beam. 35 μJ are used for SHG, which is the pump beam for the NOPA stage (4 mm BBO). There the red part of the supercontinuum is amplified to 4 μJ . The mid-IR beam is generated in a DFG process (1 mm BBO) using another fraction (11 μJ) of the fundamental beam. The main part of the 1030 nm beam amplifies the mid-IR beam in a last OPA stage, generating 10 μJ of the mid-IR pulses. This will be discussed together with the pulse compression in the next chapter. Courtesy of M. Neuhaus.

In the first part of this work a reliable seed for the OPCPA had to be built, which allows to overcome these challenges. Consequently, the designed OPCPA follows a different scheme, as shown in figure 3.1. First of all, only a single amplifier output (fundamental) is used, which makes it applicable to a broad range of systems. A portion of the pulse energy is used to generate a supercontinuum in bulk material, which will be described in the first part of this chapter. Afterwards this seed beam is amplified by the second harmonic of the fundamental in a nonlinear OPA (NOPA) setup and overlapped with the fundamental in a difference frequency generation (DFG) process, which are described in the second part. Thereby, broadband, passively CEP-stable pulses are generated, which are further amplified in a

last OPA stage.

All presented stages are appropriately chirped. Pulse stretching and compression will be discussed together with the last amplification stage and the CEP stability in detail in chapter 4.

3.1 Supercontinuum generation

The first step in the OPA is the generation of spectral broad pulses. Different techniques have been developed to broaden the laser spectrum, where the most straight forward one, the supercontinuum generation (SCG) in bulk material has been chosen in the present setup. It is also referred to as white-light generation. As mentioned already in chapter 2.3 self phase modulation (SPM) and self focusing (SF) are the main driving forces of the frequency generation, as well as the main source of nonlinearities in the refractive index, which will be described in more detail in the next section.

3.1.1 Theory

When a linear polarized laser pulse travels through an isotropic medium, it distorts the atomic motion and thereby introduces birefringence [63]. This effect is called optical Kerr effect (equation 2.1). The disturbance usually leads to a positive nonlinear refractive index n_2 . This changes the phase velocity v_p , which is given by:

$$v_p = \frac{c}{n(I)}. \quad (3.1)$$

For a Gaussian beam the phase front gets curved, when the energy of the pulse reaches a threshold power P_{crit} , which is given by [64]:

$$P_{\text{crit}} \approx \frac{0.15\lambda^2}{n_0 n_2}, \quad (3.2)$$

self-focusing will appear. After traveling some distance through the material this process results in a focus, which, for a collimated beam, is reached after the distance L_c [65]:

$$L_c = \frac{0.367L_{DF}}{\sqrt{[\sqrt{\frac{P_{in}}{P_{out}}} - 0.852]^2 - 0.0219}}, \quad (3.3)$$

where L_{DF} is the Rayleigh length of the beam [64]. For a convergent beam this length is reduced by the focusing length of the beam

$$\frac{1}{L_{c,f}} = \frac{1}{L_c} + \frac{1}{f}. \quad (3.4)$$

This effect, which results in a collapse into a soliton, is limited by several effects like plasma defocussing, multi-photon absorption and group velocity dispersion [66, 67]. Like the other processes, they are also highly dependent on the intensity. The interplay of these effects gives rise to the formation of a filament, which is quite universal, as it appears in different media [65]. Filamentation can be understood as an equilibrium state between the effects and thereby also highly depends on the intensity. The filament can survive as long as energy from the pulse can be deposited into the filament, which is described by the moving focus model [68]. For high peak powers, multifilamentation can occur, due to fluctuations in the beam profile. This results in an unstable, strongly rippled spectrum due to interference.

The shape of the supercontinuum is mainly determined by three processes: Firstly, the generation of the new frequencies is mainly driven by self-phase modulation (SPM). The time dependent phase can be written as [69]:

$$\omega(t) = \frac{d\phi(t)}{dt} = \omega_0 - \frac{n_2\omega_0}{c}L\frac{dI(t)}{dt}, \quad (3.5)$$

where L is the propagation distance. Therefore, new frequencies are generated due to the slope of the pulse, where lower frequencies are originating from the rising edge, while higher frequencies are found on the falling edge of the pulse. This corresponds to a positive chirp.

Secondly, self steepening appears, which arises from the dependence of the group velocity on the intensity [70]. Since higher intensities travel slower through the material (equation 3.1), the leading edge is stretched and the trailing edge is compressed. This is visible in the spectra by a broad plateau at short wavelengths. Thirdly, pulse splitting [71, 72], leads to the formation of two "sub-pulses", which generates a peak at short wavelength: Close to the critical power in the center of the peak, energy is redistributed to the side-bands of the pulses via SPM. Since the intensity in the center is then lower than in the wings, the wings get split following equation 3.1. As they are still overlapped for some time, the energy of

the high frequencies can be redistributed to the higher wavelength via a process similar to the three-wave mixing (section 3.2) [73, 74]. Nevertheless, a peak in the blue region can survive this process, also visible in the spectra (figure 3.2) presented here. This process also results in a chirp of the supercontinuum.

3.1.2 Experiment

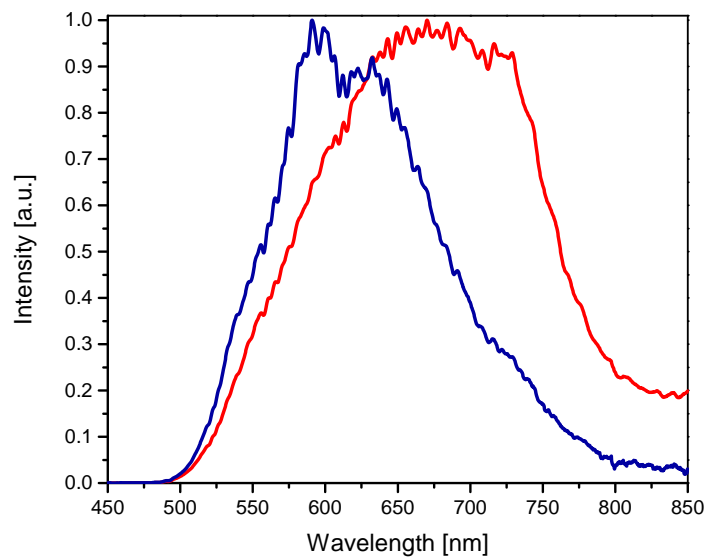


Figure 3.2: The supercontinuum spectrum generated by 1.1 ps pulses in 4 (blue) and 6 mm (red) YAG. It was found, that the thicker crystal is the more appropriate one in terms of short- and longterm stability for 1.1 ps pulses.

In case of supercontinuum generation a lot of parameters are coupled with each other. Even with a given wavelength of 1030 nm and a pulse duration of 1.1 ps in the present case, several variables have to be matched to each other. Focusing conditions, the used input power and the material are influencing each other. This makes it hard to find the optimal parameters. Furthermore, the optimal settings can only be found for one quantity at once. An example for this behavior is the stability of the supercontinuum based on peak-to-peak measurements. The best value for the stability neither corresponds to the broadest generated spectrum nor to the highest powers. The scope in this work was to find the parameters leading to the most stable supercontinuum in the range of 600-750 nm, which is the amplification bandwidth of the following NOPA stage (3.4.1). Thereby, it is

highly relevant for most OPA-applications and can be used as a guideline for the common 1030 nm pump beams.

For the supercontinuum generation a couple of different materials are available [63, 75]. As described in the literature, YAG is the best material for long laser pulses. To investigate the applicability of supercontinuum generation in bulk with the Innoslab amplifier, 4 mm and 6 mm thick plates were used together with different focusing lenses (50 mm, 75 mm, 100 mm and 125 mm) to find the best focusing conditions. The same was done for different input energies (9 μ J - 16 μ J). Recent results in the literature suggest that even thicker crystals might lead to better results, but haven't been applied here [36]. It was found, that the filament in the 4 mm crystal spanned to the back part of the crystal. In contrast, the supercontinuum generation wasn't stopped by the crystal edge in the 6 mm crystal. Therefore, also the spectrum was broader, as shown in figure 3.2, and more stable. The best results in case of the 6 mm crystal for the stability were obtained together with the 75 mm lens. Nevertheless, it is worth mentioning, that the results for different focusing lengths and input powers don't differ much. The focusing conditions themselves are also very important. In contrast to other nonlinear stages, where the crystal is usually placed in the focus to achieve a flat wavefront, this is not the case for the supercontinuum presented here. It was found, that for every change of input power it is necessary to move the crystal slowly from behind closer to the focus. Thereby, the filament starts to appear at the back part of the crystal and grows to a certain point. Meanwhile, also the peak at high frequencies is broadening. After reaching this optimal configuration, multifilamentation occurs and the supercontinuum becomes unstable. Finally, the crystal gets damaged. The whole process takes place on a sub-millimeter scale and is thereby prone to misalignment.

Another important improvement was achieved by inserting an iris in front of the focusing lens. By aperturing the outer part of the 1030 nm beam, corresponding to an energy throughput of 90-95%, the stability of the white-light could significantly be improved. This is probably a cleaning effect of the 1030 nm beam, since the Innoslab amplifier generates an elliptical beam profile (figure 2.7).

As shown in figure 3.3 for a laser pulse of 1.6 ps duration, the spectrum depends on the input energy. Similar spectra were obtained for 1.1 ps pulses. All of them included few nanojoules of energy in the NOPA wavelength range of 600-750 nm. The final input power of 11 μ J was chosen only by the stability. At slightly higher

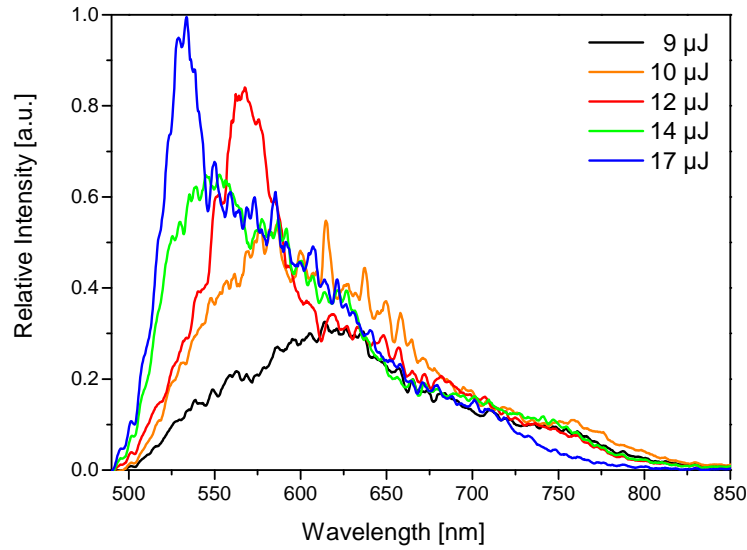


Figure 3.3: Spectrum of the supercontinuum at different input energies for 1.6 ps pulses. Courtesy of M. Neuhaus.

input powers of 13 μJ , multifilamentation becomes visible and afterwards the crystal is damaged.

With 11 μJ and a 75 mm lens the best stability on long time scales was achieved (figure 3.4). These measurements done for different regions of the supercontinuum revealed, that some parts of the spectrum are fluctuating more severe. The spectral region of highest stability can, to some extend, be chosen by the input power and the focusing conditions. This way, the stability of the supercontinuum could be kept stable for the spectral region of the NOPA. Nevertheless, small variations of the input conditions don't lead to noticeable change of the output parameters, which is also important for the following OPA stages.

The recently reported difficulty of generating a stable supercontinuum for narrowband pulses cannot be confirmed [76]. The observed stability of the supercontinuum, as shown in figure 3.4, is excellent ($<1\%$ rms), and similar to the other values in the literature. An explanation for the different results might be found in the stability of the driving laser system. This would underline the importance of the high efforts undertaken in this work, to build a robust pump source.

It is also important to mention, that no damage occurred to the YAG crystal for weeks, while realignment is also fast and easy. In addition, the supercontinuum

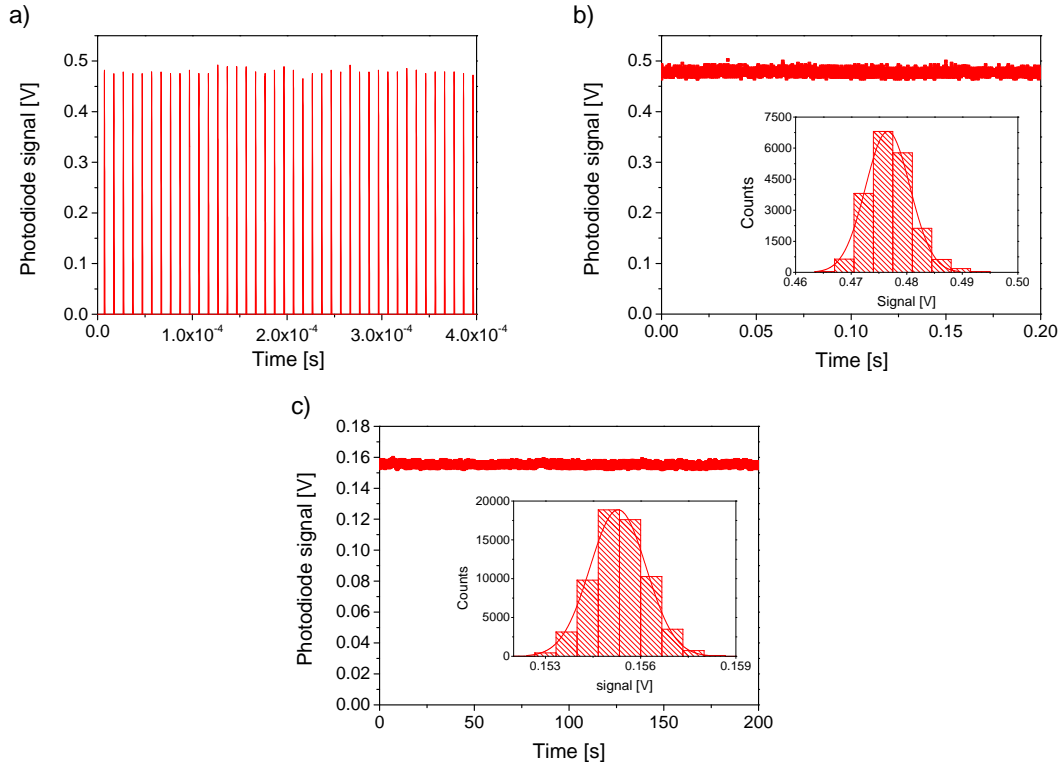


Figure 3.4: Stability of the supercontinuum around 700 ± 20 nm measured by a photo diode: a) peak-to-peak stability, b) short term stability measured for 20 ms: 0,6% rms and c) long term stability over more than 3 min: <1% rms. Similar results were obtained for other parts of the NOPA bandwidth.

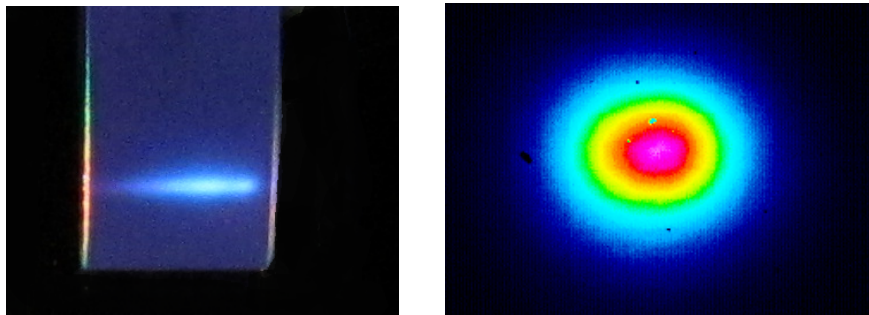


Figure 3.5: Supercontinuum filament (left) and its beam profile (right). The beam profile after the YAG crystal is more Gaussian than the fundamental beam.

has a better spatial profile (fig 3.5) compared to the Innoslab output, which is important for the following nonlinear stages.

Besides the good parameters obtained here, the present approach is probably not easily scalable towards even higher repetition rates. It was found, that the crystal heats up by almost 10 °C as shown in figure 3.6 and similar results were recently reported for comparable parameters [36]. Nevertheless, white-light generation has been reported for even higher repetition rates and pulse durations [63].

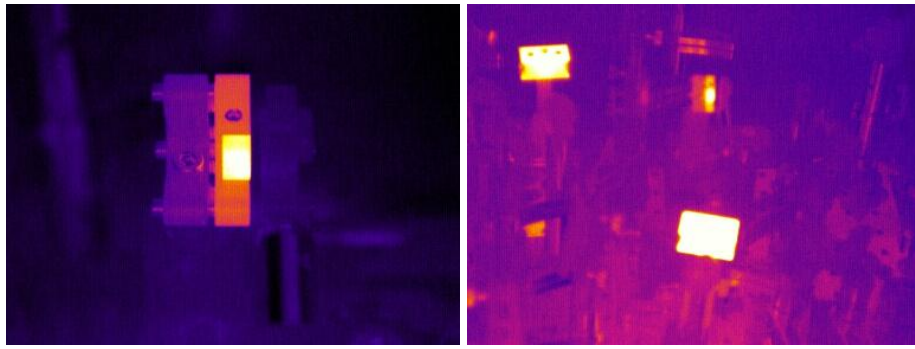


Figure 3.6: Thermal images of the YAG-crystal (left) and the NOPA setup (right). The crystal heats up by ~ 10 °C. The rest of the setup has room temperature, except for the beam dumpers.

3.2 Coupled wave equation

The following section is closely related to [77] and summarizes the important equations.

The basis of optical parametric amplification, and therefore for all the following parametric stages, is the three-wave-mixing process in a nonlinear medium, where a strong pump beam transfers energy to a seed beam. This effect can be understood by the nonlinear polarization which is given by:

$$P(t) = \epsilon_0(\chi^{(1)}E(t) + \chi^{(2)}E(t)^2 + \chi^{(3)}E(t)^3 + \dots), \quad (3.6)$$

where $\chi^{(1)}$ is the linear susceptibility, while $\chi^{(2)}$ and $\chi^{(3)}$ are the second and third order susceptibilities, respectively. The electric field of the laser pulses are given by

$$E_n(t) = E_n e^{-i\omega_n t} + c.c, \quad (3.7)$$

where c.c is the complex conjugate.

In the case that two laser pulses $n=1,2$ are interacting with a material whose second order susceptibility is non-zero, the second order polarization can be written as:

$$P^{(2)}(t) = \epsilon_0 \chi^{(2)} [E_1^2 e^{-2i\omega_1 t} + E_2^2 e^{-2i\omega_2 t} + 2E_1 E_2 e^{-i(\omega_1 + \omega_2)t} + 2E_1 E_2^* e^{-i(\omega_1 - \omega_2)t}] + 2\epsilon_0 \chi^{(2)} [E_1 E_1^* + E_2 E_2^*]. \quad (3.8)$$

The first four terms lead to radiation, where the first two belong to second harmonic generation, the third one to the sum frequency and the fourth one to difference frequency generation. The last term is the optical rectification, which is not discussed here. These processes can be described by the coupled wave equations. They can be derived from the Maxwell equations, giving:

$$\nabla^2 E - \frac{1}{c^2} \frac{\partial^2 E}{\partial t^2} = \frac{1}{\epsilon_0 c^2} \frac{\partial P^{NL}}{\partial t^2}. \quad (3.9)$$

Using the planar wave function 3.7 with:

$$E_n = A_i e^{ik_n z} \quad (3.10)$$

and the nonlinear polarization as:

$$P^{NL}(z, t) = P^{NL}(z) e^{-i\omega t} + c.c, \quad (3.11)$$

together with the polarization amplitude for the pump beam (p) in dependence of the signal (s) and idler (i) beam:

$$P_p = 4\epsilon_0 d_{\text{eff}} A_s A_i e^{i(k_s + k_i)z}, \quad (3.12)$$

where d_{eff} is the effective nonlinear optical coefficient, one obtains with $\nabla = \frac{\partial}{\partial z}$:

$$\left[\frac{d^2 A(z)}{dz^2} + 2ik \frac{dA(z)}{dz} - k^2 A(z) + \frac{\epsilon \omega^2}{c^2} A(z) \right] e^{i(kz - \omega t)} + c.c = -\frac{\omega^2}{\epsilon_0 c^2} P^{NL}(z) e^{-i\omega t} + c.c. \quad (3.13)$$

Since $k^2 = \frac{\epsilon \omega^2}{c^2}$, two terms cancel out. The slowly varying envelope approximation (SVEA) can be applied, giving:

$$\frac{d^2 A_p}{dz^2} \ll k_p \frac{dA_p}{dz}. \quad (3.14)$$

Thereby, the coupled wave equations are obtained, being:

$$\frac{dA_p}{dz} = \frac{2id_{\text{eff}}\omega_p^2}{k_p c^2} A_s A_i e^{i\Delta k z} \quad (3.15)$$

$$\frac{dA_s}{dz} = \frac{2id_{\text{eff}}\omega_s^2}{k_s c^2} A_p A_i^* e^{-i\Delta k z} \quad (3.16)$$

$$\frac{dA_i}{dz} = \frac{2id_{\text{eff}}\omega_i^2}{k_i c^2} A_p A_s^* e^{-i\Delta k z}. \quad (3.17)$$

The first equation thereby describes the pump beam and the last two belong to the signal and idler beam respectively. Δk is the wave vector mismatch:

$$\Delta k = k_i + k_s - k_p. \quad (3.18)$$

In case of an undepleted pump ($A_p = \text{const.}$) the gain of the signal is given by [78]:

$$G = \frac{I_s(z)}{I_s(0)} = 1 + \frac{\Gamma^2}{g^2} \sinh^2(gL) \quad (3.19)$$

with:

$$g = \sqrt{\Gamma^2 - \left(\frac{\Delta k}{2}\right)^2} \quad (3.20)$$

and:

$$\Gamma^2 = \frac{8\pi^2 d_{\text{eff}}^2 I_p}{n_i n_s n_p \lambda_i \lambda_s \epsilon_0 c} \quad (3.21)$$

where I_p is the pump intensity and L the crystal length. Based on these equations, there are a couple of constraints, that have to be taken into account. For an efficient amplification it is important to control the wave vector mismatch. Employing:

$$k = \frac{n\omega}{c} \quad (3.22)$$

into 3.18 with $\Delta k = 0$ yields:

$$n_p \omega_p = n_s \omega_s + n_i \omega_i. \quad (3.23)$$

This corresponds to the momentum conservation and can just be achieved in birefringent crystals, which have two refractive indices. Furthermore, for broadband signal beams, phase matching will be even more complicated, since the wave

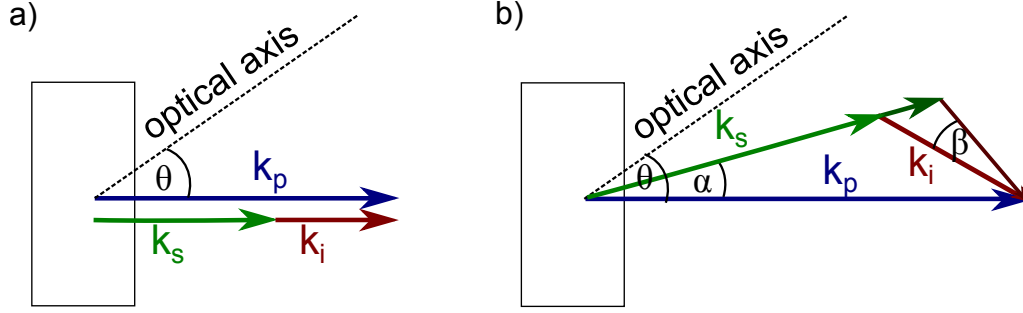


Figure 3.7: Phase matching for collinear and noncollinear geometry. The noncollinear geometry is shown for the tangential phase matching condition. The walk-off compensating phase matching is not used in the stages presented in this work.

vector mismatch has to be small over the whole frequency range of the signal. This can only be achieved for short crystal lengths, limiting the gain. By introducing a noncollinear angle α , as shown in figure 3.7, the achievable bandwidth can be extended. In the collinear case, all beams are propagating in the same direction, which is only defined by θ , the phase matching angle [78]. The noncollinear angle α thereby gives an additional degree of freedom, allowing to match more signal momenta to the pump momentum. The idler thereby exhibits an angular chirp ($\beta(\lambda)$). Nevertheless, for the collinear geometry a broad bandwidth can be achieved near the degeneracy point. This can be explained in terms of the group velocity mismatch (GVM), which is derived from the wave vector mismatch and the conservation of energy:

$$\omega_p - \omega_s - \omega_i = 0 \quad (3.24)$$

as [79]:

$$GVM = \frac{\partial k_s}{\partial \omega_s} = \frac{1}{v_{g,s}} - \frac{1}{v_{g,i}}, \quad (3.25)$$

with $v_g = \partial\omega/\partial k$ being the group velocity. It thereby vanishes at the degeneracy point, where the wavelengths of signal and idler are the same.

Besides the geometrical issues just described, the choice of the crystal has important influence on the efficient amplification, as described by the gain. It directly defines three fundamental variables: d_{eff} , the available interaction length and the index of refraction. Indirectly, it also limits the achievable pump intensity due to its damage threshold and the available wavelength due to absorption, which is for beta barium borate (BBO) limited to $<2.5 \mu\text{m}$.

3.3 Simulations with SISYFOS

To investigate the behavior of the OPA stages, simulations with the program: Simulation system for optical science (SISYFOS), developed by Dr. Gunnar Arisholm, were performed [80, 81].

SISYFOS is based on a Fourier-space method, which solves the coupled wave equations in the frequency domain. The pulses are simulated in 3D with their electric fields, allowing to analyze even complex aspects of nonlinear amplification as beam profiles and pump depletion. The propagation is simulated with dispersion, temporal and spatial walk-off for collinear and non-collinear geometries. Furthermore, nonlinear effects, as SF, can be investigated as well as two-photon absorption. In addition, thermal effects and pulse-front tilts can be taken into account which haven't been implemented here.

The BBO crystals were simulated based on the Sellmeier equations taken from [82], while lithium niobate (LNB) data for chapter 7 can be found in [83]. The simulations, shown here for the NOPA and the DFG, also include the temporal stretching. This aspect will be discussed in detail in chapter 4.

3.4 Generation of broadband 2 μm pulses

The supercontinuum generation stage is followed by two additional ones to generate the seed for the main amplification stage. In the first one, the NOPA stage, the pump beam for the DFG-process is generated. Afterwards, the idler of the DFG is used as the seed pulse for the main OPA amplifier. It is worth mentioning, that this scheme is theoretically applicable to basically all high average power amplifiers, while being able to generate a few-cycle, CEP stable seed.

In comparison to the main amplification stage, the aims of the seed generation are different. It is most important to obtain a broad spectral bandwidth, that can afterwards be amplified. Therefore, the power and the efficiency don't play a significant role, since the overall efficiency of the setup is mainly determined by the last amplification stage.

A lot of effort has also been spent to keep the fluctuations of the laser as small as possible, as described in chapter 2. In case of the OPA stages, these not only lead to power changes, but also to spectral ones. In addition, the CEP-stability will highly depend on the stability of spectrum. Therefore, it was important to operate the stages deeply in saturation, where small fluctuations aren't amplified.

As mentioned before (chapter 2.1), the intensity fluctuations in the saturated OPA are mainly determined by the ones of the pump laser. The stability is also limited by beam pointing drifts, which can be reduced by a stable pump laser system. In addition, beam pointing instabilities can be reduced by a rigid design of the OPA setup with few movable parts and a short beam path.

3.4.1 Nonlinear Optical Parametric Amplifier

The NOPA stage is basically the only noncollinear stage within the whole setup, although the main amplification stage has a slight angle to separate the beams. It serves in the following stage as the pump beam and has to deliver high pulse energies. In addition to the power, the NOPA has to generate a broad spectrum, since the 1030 nm beam in the DFG is narrowband.

To achieve a broad bandwidth two different approaches are possible. The easiest approach, chosen here, is the usage of the second harmonic to amplify the supercontinuum. Another one would be to use the third harmonic of the fundamental. This could be used to amplify shorter wavelengths in the NOPA, but unfortunately the additional frequencies in the DFG would be generated at short wavelength. Since the goal of this work was to generate a long wavelength output, this was not considered, although the final pulse durations should be shorter and the tunability better. Furthermore, the frequency tripling is less efficient, so that more energy of the Innoslab output has to be used to generate a sufficient pump power for the DFG-process. Finally, the absorption for short wavelengths is higher, so that crystal damage occurs earlier. This can be a problem, especially when higher repetition rates are used.

SHG To be able to pump the NOPA the fundamental beam had to be frequency doubled. The intensity was set to 50 GW/cm^2 with 3.6 W input power, focused into a 2 mm BBO crystal. The achieved output energy was 2.4 W, the overall efficiency thereby yielded 66 %. Going towards higher intensities is not recommendable, because significant pump depletion was already visible in the spectra, as shown in figure 3.8. Therefore, increasing the intensity could lead to beam distortions due to reconversion of the pump. The power dependence of the SHG on the 1030 nm is linear, resulting in a stable output.

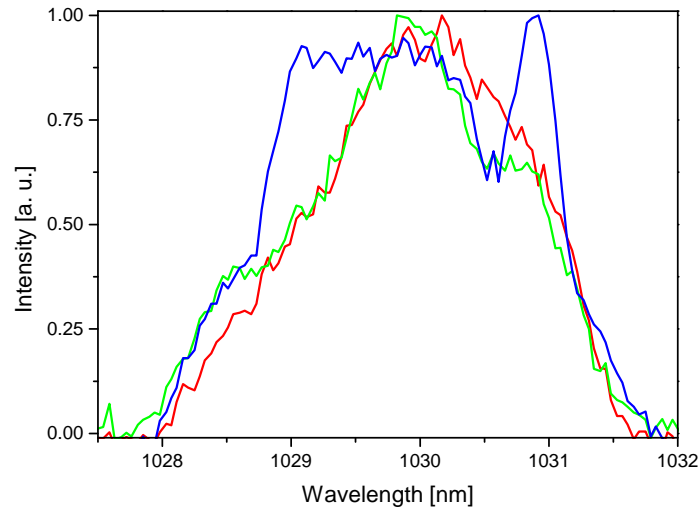


Figure 3.8: Pump depletion of the 1030 nm beam in the SHG. The red curve corresponds to the fundamental in front of the crystal, whereas the blue and green curves belong to the one after the crystal. The green curve and the blue curve show the spectrum without and with frequency doubling.

Simulation The NOPA was simulated with the measured white-light spectrum and the back calculated phase (for details, see chapter 4.1.2) (figure 3.9). The pump beam was assumed as a Fourier-limited pulse with a duration of 1100 fs, corresponding to the measured pulse. The intensity in the NOPA was set to about 50 GW/cm^2 in the pump beam, to avoid crystal damage. The beam of the supercontinuum had a size of $100 \mu\text{m}$, about $2/3$ of the pump beam ($160 \mu\text{m}$), with an energy of 2 nJ. The phase matching angle and the noncollinear angle were 21.4° and 1.9° for a broad amplified spectrum, respectively.

With these parameters the optimal crystal length was found to be around 4 mm and an output power of 630 mW was achieved.

Experiment In the experiment with the same parameters an output power of 530 mW was obtained with a broad amplification bandwidth, as shown in figure 3.10. The discrepancy between experiment and simulation is expected due to crystal imperfections and other small deviations. Especially the exact energy of the supercontinuum was unknown and had to be estimated. Anyway, similar differences of 10-15% will also be apparent in the next stages.

Besides the overall energy, the results are in good agreement to each other. The spectrum is a little bit broader than expected, which can be attributed to the di-

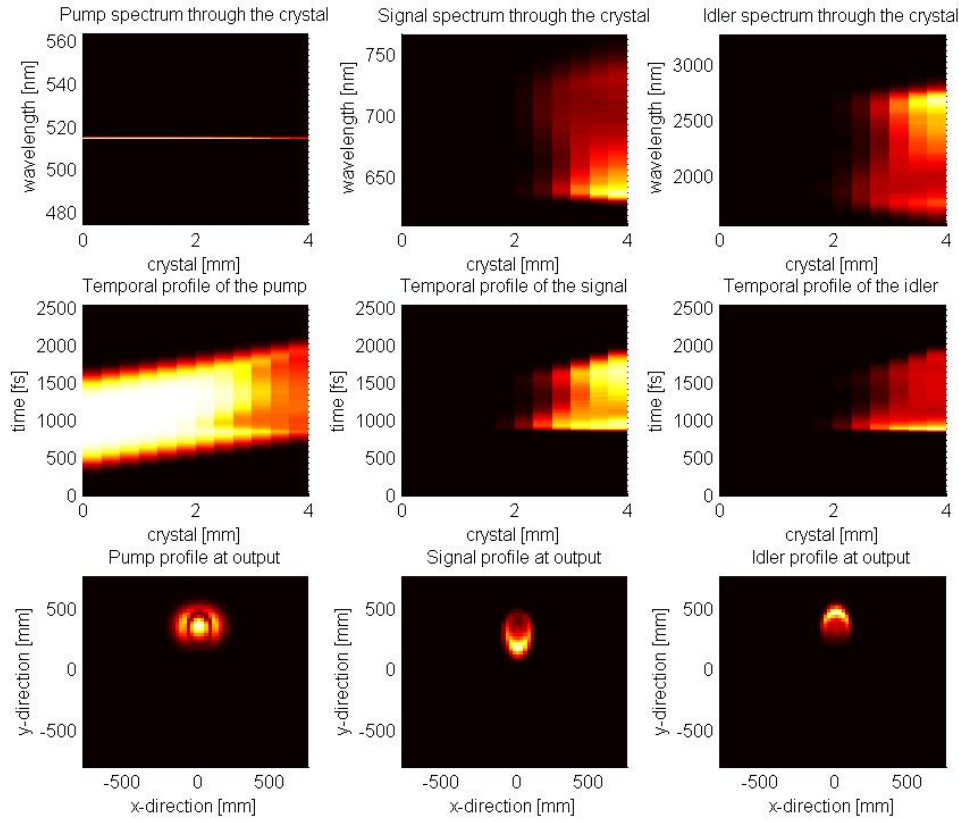


Figure 3.9: Simulation of the NOPA. The left column show the pump, the seed and the idler results. The first two rows correspond to the spectral and the temporal profiles within the crystal along the x-axis. The retrieved output energy of the signal yielded 800 mW.

vergence of the pump beam, which allows to phase match additional wavelengths. Furthermore, this stage is sensitive to the OPA angles and the beam parameters of the supercontinuum. Besides that, in both cases a peak at around 640 nm is observable and the OPA is saturated. A test with a 3 mm thick crystal led to a significant decrease in power and higher fluctuations, proving the saturation of this stage.

Another important feature found in the simulation and the experiment is the small quadratic spectral chirp in the beam, as depicted in figure 3.11, which is not present in the focus. This is a result of the phase matching conditions, which have a parabola like shape. It cannot be avoided with the present configuration, but also doesn't influence the following stages significantly.

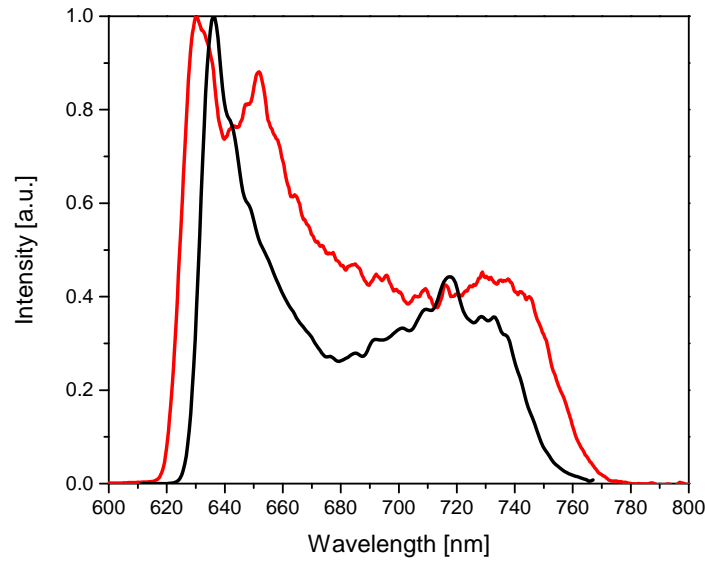


Figure 3.10: Spectrum of the NOPA (red) and the theoretical prediction (black).

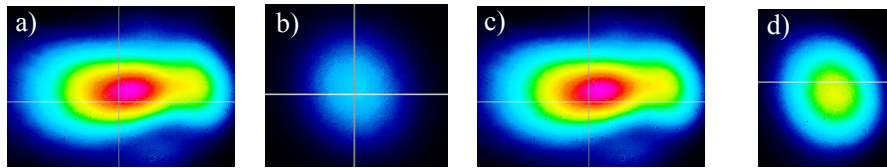


Figure 3.11: Chirp of the NOPA in the far-field. The beam profile is shown for different filters: a) Full beam, b) 630 nm, c) 700 nm, and d) 740 nm.

3.4.2 Difference Frequency Generation

Like the supercontinuum generation, special efforts were undertaken to generate the optimal pulses in the DFG for the following main amplification stage. Therefore, it was important that a strong seed beam could be used, as it is derived from the 1030 nm fundamental beam. This allows an optimal amplification and stability, also by using a big spot size for the seed beam. Since the idler at around 2 μm is used in the following stage, the angular chirp of the idler has to be taken into account, which can cause severe beam distortions.

Simulation Like for the NOPA, also the DFG was simulated with the 1030 nm signal beam as a Fourier-limited Gaussian pulse with an energy of 11 μJ (figure 3.12). The NOPA spectrum was implemented with an energy of 4.5 μJ . The

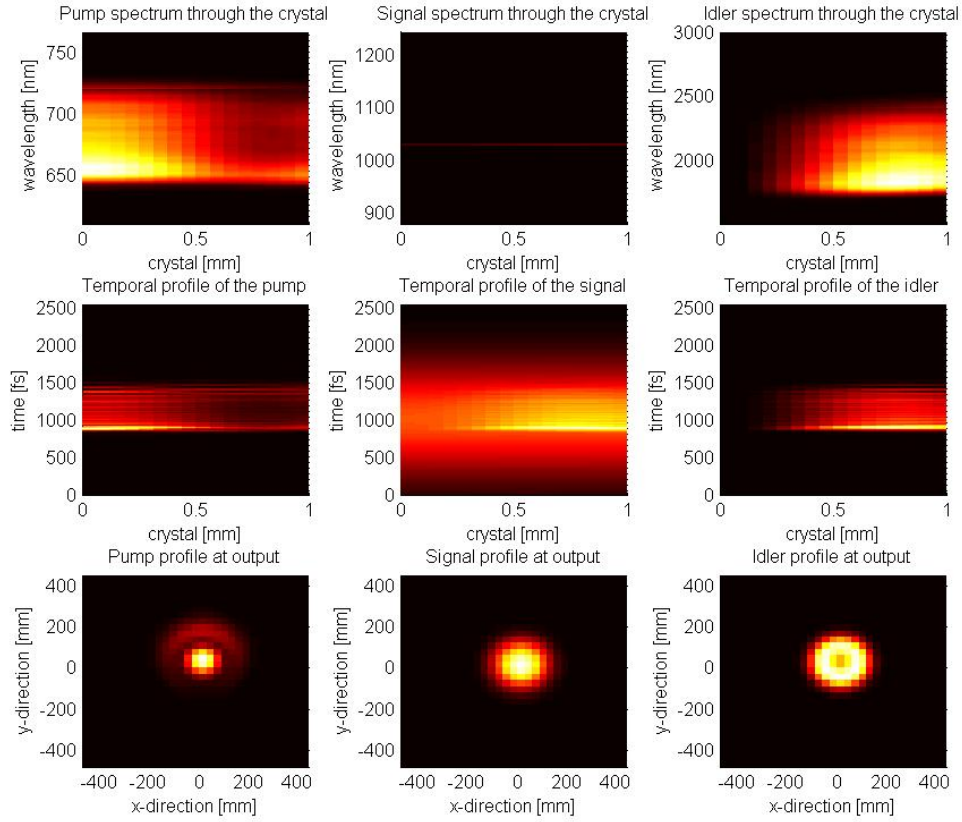


Figure 3.12: Simulation of the DFG process. The retrieved output energy of the idler yielded 72 mW

beams focal spot sizes were 200 μm for the seed and 150 μm for the pump beam with a propagation length of 1 mm in BBO at 20.1° in a collinear geometry. The idler is thereby slightly oversaturated, which is indicated by the reconversion visible in the center, and the peak at long wavelength from the NOPA is preserved.

Experiment In the beginning of this thesis a slightly noncollinear geometry for the DFG was chosen, since no dichroic mirrors were available. It didn't show significant disadvantages to the collinear stage, except the relatively low conversion efficiency compared to the theoretical predictions. The output energy was about 36 mW. Later on, when the main amplifier stage was built (chapter 4), its output showed a strong angular chirp and low amplification due to the wave vector mismatch, introduced by the noncollinear geometry of the DFG. This can only be compensated in a stretcher like setup [45, 84], which is complex and has a couple of disadvantages:

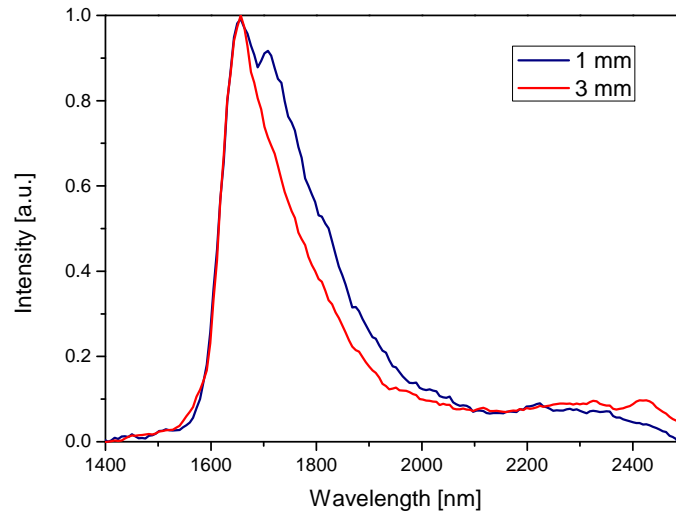


Figure 3.13: Spectrum of the DFG for different BBO thicknesses.

1. The long beam path leads to beam pointing fluctuations for the following stages.
2. The setup is inflexible to changes in the spectrum of the pulses.
3. The chirp cannot be fully compensated.

Another, more simple approach, is the compensation with wedges, which would probably result in even worse results.

These problems were avoided in the present setup by using the collinear geometry. This improvement could be achieved with the design of dichroic mirrors for the 1030 nm and the NOPA beam by V. Pervak. As shown in figure 3.13, changing to a complete collinear geometry leads to a broad spectrum, better than before. Please note, that the spectra shown for the DFG are underestimating the long wavelength part, since the used InGaAs spectrometer (nirQuest 512, Ocean Optics) significantly loses sensitivity above 2.3 μm . The real spectrum is broader, which will be visible in the last amplification stage (chapter 4.1.2).

Two crystals for the DFG were tested in the collinear geometry, leading to similar results. Thereby, it was decided to take the thin one (1 mm). The maximum output power was up to 60 mW with a broad spectrum and a round beam profile.

As shown in figure 3.14, the DFG can be operated in saturation, since the 1030 nm beam serves as a seed in this stage. Therefore, a comparably high seed energy of

11 μJ was used to suppress fluctuations originating from the laser. The additional power is thereby small compared to the gain in stability. As shown in the insets, also the spectrum does not depend on the power of pump and seed, which is important for the overall stability of the setup. Due to the careful alignment and the stable input beams, the fluctuations could be kept below 1%.

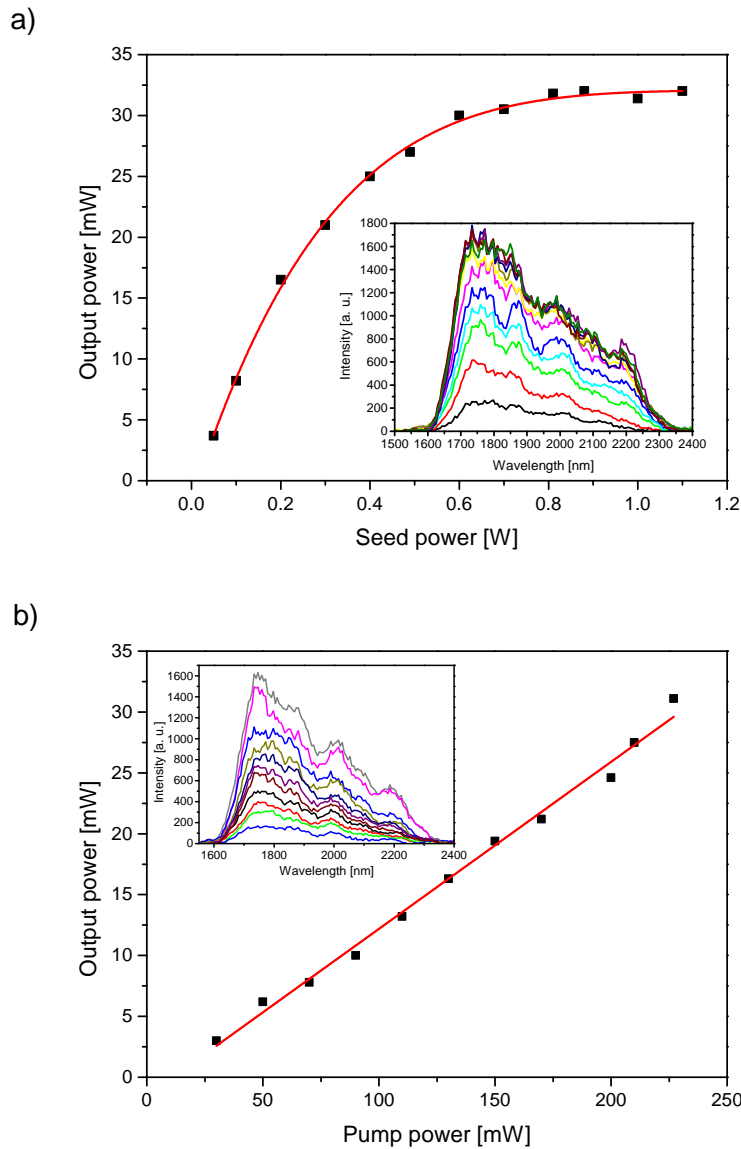


Figure 3.14: Power and spectral dependencies of the DFG for a) seed and b) pump beam. The insets depict the corresponding spectra.

3.5 Summary

The results obtained in this chapter prove, that a stable seed for picosecond pumped OPCPAs can be obtained, even without a broadband seed laser. Such a "single output OPA" has a couple of advantages compared to other schemes: First of all, the required laser system is simplified, since only one laser output is used for the seed generation and its amplification. No broadband Ti:Sa based front-end had to be implemented and only some requirements for the Innoslab amplifier had to be fulfilled.

Furthermore, an all optical synchronization is favorable compared to the active synchronization. Fluctuations in time are intrinsically compensated and do not have to be taken into account. It is also important to note, that not much pulse energy is needed for the seed generation in the present case. With about 50 μJ in total, this corresponds to 5% of the maximum output for a 100 W amplifier and in the present case of the 500 W Innoslab amplifier to even less.

The system proves, that even with 2 consecutive nonlinear stages and long pulse durations a stable operation can be assured. The power stability of about $\sim 1\%$ is comparable to standard laser systems and allows stable operation of the following OPCPA stage.

The novelty of the presented seed laser may also be illustrated by the possibility of conducting experiments with the DFG output (chapter 5). Therefore, it is also important to mention, that the DFG is passively phase stable, which will be discussed in the next chapter.

4 Dispersion management and CEP stabilization

The basic principles of OPAs have already been discussed in chapter 3. This chapter is therefore dedicated to the more difficult topics related to OPA-development. It thereby introduces some ideas, that led to the scheme of the seed generation reported before. By that, some additional advantages and how they can be implemented in a complete OPCPA system are shown.

This chapter is divided into two parts, related to the most critical parameters for OPAs: the pulse duration and the CEP stability. The first one deals with the dispersion management of the whole setup. As already reported, the super continuum is intrinsically chirped, so that all stages built here are basically OPCPA stages. In this chapter it will be shown, how the dispersion of the seed can actively be engineered for an optimal extraction of energy in the main amplification stage (in the following referred to as OPCPA stage in contrast to the other ones before). The dispersion management is also important to obtain few-cycle pulses, close to the Fourier limit. In most few-cycle OPAs a Dazzler corrects the spectral phase to obtain an optimal compression in the end. This device was not available for the repetition rates used in the present work, which makes the dispersion management more difficult.

The system presented here uses the material dispersion to stretch and to compress the pulses: The group velocity dispersion changes its sign for many materials at around $1.3\text{ }\mu\text{m}$. Therefore, material placed in the different spectral regions (near-IR and mid-IR) in the consecutive stages can neutralize each others dispersion. Together with some chirped mirrors, this leads to a simple scheme of pulse compression to the few-cycle regime, which will be discussed in 4.1. Additionally, a simple technique to measure the dispersion will be described in this chapter, that was developed during the construction of the laser system (4.1.1). It is advantageous for long wavelength, broadband pulses and especially at low energies. Afterwards, it will be discussed, how the dispersion affects the main amplification

stage and how the compression for the OPCPA stage could be achieved (4.1.2). The second part of the chapter discusses the carrier-envelope phase (CEP) stability of the laser system. In contrast to Ti:Sa based systems the CEP stability is achieved passively through the DFG process. The CEP stability is important for many applications in strong-field physics, like the photoionization experiments reported in chapter 5.

4.1 Dispersion control and measurement

As already discussed in section 2.3, the spectral phase can be described as Taylor expansion with higher order terms, where the GDD and the TOD are of special interest. As the value of the refractive index changes with the wavelength, it leads to a wavelength dependent phase velocity. This effect is present for all transparent media and has to be actively controlled. The wavelength dependent refractive index for a material can be described by the empirical Sellmeier equation, which is given by:

$$n(\lambda) = \sqrt{1 + \sum_i \frac{A_i \lambda^2}{\lambda^2 - B_i}} \quad (4.1)$$

where usually $i = 3$. Values for the material used in the setup are shown in table 4.1.

material	A_1	A_2	A_2	$B_1 [\mu\text{m}^2]$	$B_2 [\mu\text{m}^2]$	$B_3 [\mu\text{m}^2]$
BK7	1.0396	0.2318	1.0105	0.0060	0.0200	103.5606
Fused Silica	0.6961	0.4079	0.8975	0.0684	0.1162	9.8962
Sapphire	1.024	1.0582	5.2808	0.0614	0.1107	17.9266

Table 4.1: Sellmeier coefficients for selected materials. Taken from [85]

An important feature of the group velocity dispersion (GVD) in material is the change of its sign, typically at wavelength 1.2-1.5 μm . At near-IR wavelengths the value is positive whereas it's negative in the mid-IR. In the present case this allows to compensate the GDD that is accumulated before the DFG, or in the other way around, by introducing material in the NOPA beam, additional material behind the DFG generation can be compensated.

The advantage of this compensation scheme is not only the relatively high flexibility, but also the high efficiency in the compression, which is basically limited to the reflexion (the anti-reflection coating) of the material used to stretch and

compress the pulses.

Unfortunately, the TOD does not reverse its sign with the wavelength. Therefore, large amounts of material still lead to long pulses. This effect can be compensated by properly designed chirped mirrors.

4.1.1 Dispersion measurement in the seed beam

To be able to stretch and compress the pulses in the way just described, the spectral phase of the pulses has to be known. To measure it for the weak, spectrally broad and temporally long pulses obtained by the DFG is a challenging task with current pulse characterization methods. Therefore, a new method was developed, which is easier to implement.

Since the DFG output had to be measured, no suitable phase-retrieval method was available. In the beginning the Frequency Resolved Optical Gating (FROG) technique was unsuccessfully tested:

Typical spectrometers have a wavelength range up to 1100 nm (Si-detectors), or down to 900 nm (InGaAs). Therefore, the second harmonic generated by a source ranging from 1600 nm to 2400 nm cannot be completely recorded by a single spectrometer, which is needed for SHG-FROG. Stitching them together is complicated and needs a careful intensity calibration of the devices.

Since the SHG couldn't be measured with a single spectrometer, the third harmonic had to be used in the present case. There, the low average power and the long pulse durations led to low intensities and thereby to an unmeasurable signal. The spectrum was furthermore highly asymmetric (figure 3.13) with low spectral intensities over a broad wavelength range. Therefore, the retrieval with THG-FROG was impossible, because the long wavelength part could not be detected at all.

The technique used in this thesis is also based on SHG, where the spectrum can be described as [86]:

$$I_{SHG}(2\omega, \phi) = \left| \int_{-\infty}^{+\infty} |E(\omega - \Omega)| |E(\omega + \Omega)| \exp[i(\phi(\omega - \Omega) + \phi(\omega + \Omega))] d\Omega \right|^2. \quad (4.2)$$

The shape of the SHG spectrum thereby depends not only on the spectral amplitudes, but also on the spectral phase of the input pulse. Since the first terms are amplitudes and positive, it maximizes, when the exponent equals to zero. Taylor

expansion of the phase to the second order:

$$\phi(\omega \pm \Omega) = \phi_0 + \phi_1 \Omega + \frac{\phi_2 \Omega^2}{2} \quad (4.3)$$

gives:

$$I_{SHG}(2\omega, \phi) = \left| \int_{-\infty}^{+\infty} |E(\omega - \Omega)| |E(\omega + \Omega)| \exp\left[i \frac{\partial^2 \phi(\omega)}{\partial \omega^2} \Omega^2\right] d\Omega \right|^2, \quad (4.4)$$

since the first two coefficients cancel. It is obvious that the signal of the SHG at given frequency maximizes, when the GDD ($\frac{\partial^2 \phi(\omega)}{\partial \omega^2}$) is zero. By inserting a known amount of material or chirped mirrors, the position of the zero crossing can be changed. For a simple spectral phase this is visible by a peak shifting of the SHG in the spectrum (figure 4.1).

The GDD of the initial pulse can then be calculated as:

$$GDD_{initially} + GDD_{introduced} = 0 \quad (4.5)$$

By introducing different amounts material, the higher order terms can be retrieved by plotting the GDD versus the wavelength, which is shown in figure 4.1 for the seed pulse. The retrieved GDD for the setup was 1923 fs^2 and the TOD 7615 fs^3 .

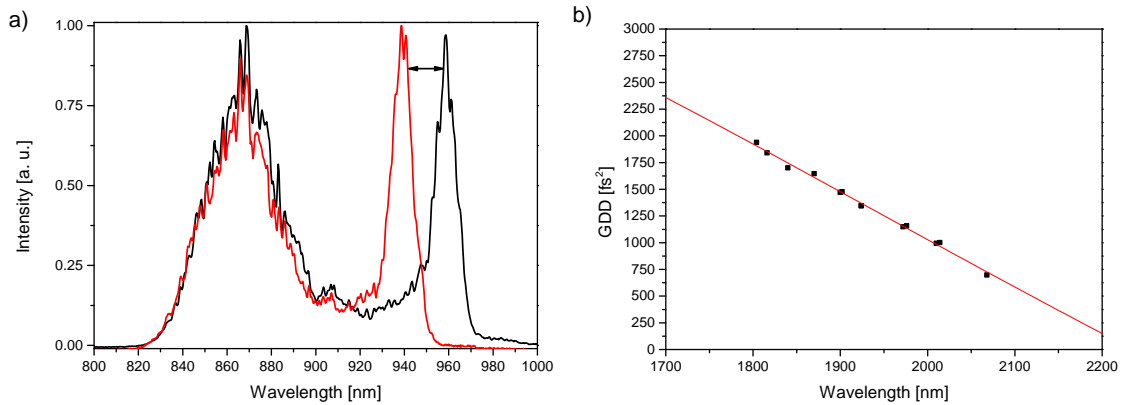


Figure 4.1: Chirp scan measurement with a 500 μm thick BBO. In a) the shift of the SHG peak is shown. The amount of sapphire differs by 5 mm, shifting the peak towards lower wavelengths. The GDD as a function of the doubled wavelength position of the SHG is presented in b). The fit yielded a GDD of 1923 fs^2 and a TOD of 7615 fs^3 .

It is important to mention that this technique has proven to be very reliable, as shown later in this section. Especially in spectral regions where no spectrometer can cover the full spectrum of the SHG the new technique is advantageous. Furthermore, it is quite robust to noise and easy to implement.

Since it only relies on the position of the SHG peak, it is not prone to intensity fluctuations and retrieval errors. In the chirp scan technique only wavelength calibration is necessary. Furthermore, low intensity pulses can be measured as shown here for 30 mW, which wasn't possible with THG-FROG. Other measurement techniques able to retrieve the spectral phase of the pulse, like multiphoton intrapulse interference phase scan (MIIPS) rely on expensive and more complex setups [87].

Nevertheless, there are some limitations on the usage: The shift of the SH-peak is only visible in presence of TOD. Furthermore only simple GDD-curves can be retrieved, for complex phases the chirp scan technique is not applicable. Anyway, in most applications like OPCPAs, where the phase is mainly determined by material dispersion, this technique can often be used.

4.1.2 Dispersion management in the main amplification stage

In contrast to the previous stages, the design of the main amplifier is more complicated as pointed out before. As mentioned already in chapter 3, the efficiency of the stage is sensitive to misalignments and imperfections like the angular chirp in the DFG. This illustrates, how much this stage (and possible following stages) depends on the quality of the seed beam. This is not only true for the laser parameters like the spectral bandwidth, intensities and beam sizes, but also optimal pulse durations of seed and pump. Since about 65 % of the total power in this setup is used in this stage, it has to be as efficient as possible. Therefore, several parameters have to be matched, which are highly correlated to each other. This will be illustrated by the comparison of an unoptimized and an optimized OPCPA stage.

Main amplifier without material optimization

As shown in figure 3.1, in both cases a 3 mm BBO is used for amplification. For an optimal amplification, the angle between pump and seed has to be kept as small as possible, since the OPCPA is operated around the degeneracy point. In principle, it would also be possible to use signal and idler together in a collinear

geometry. This would lead to an even broader spectrum and higher pulse energies, but wipe out the CEP stability (section 4.2), since the idler is not CEP stable.

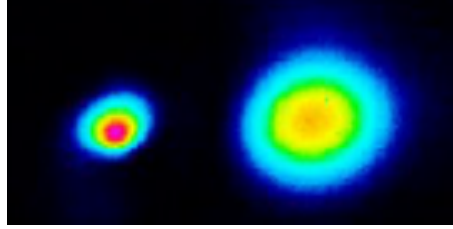


Figure 4.2: Beam profiles of the OPCPA at crystal position. The seed is shown on the left, whereas the pump is shown on the right.

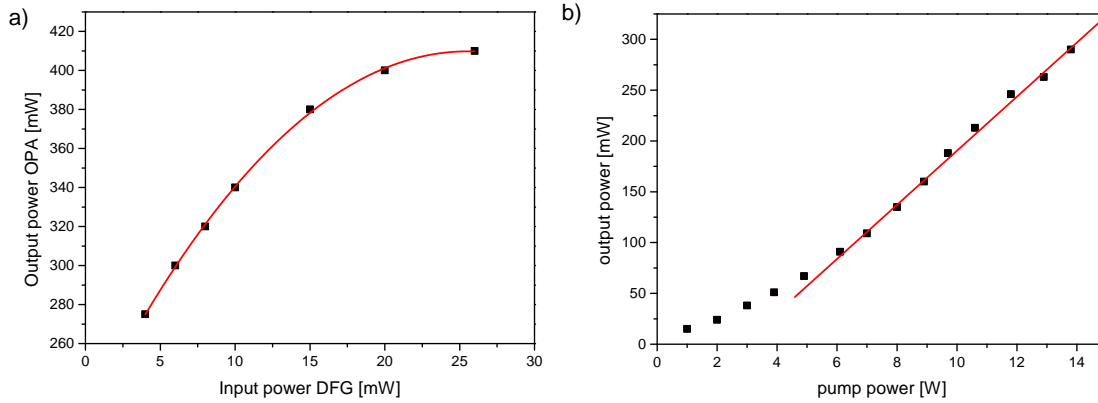


Figure 4.3: Power dependences for the a) seed and b) pump beam of the unoptimized OPCPA.

The beam sizes (FWHM) were $350\ \mu\text{m}$ for the pump and $150\ \mu\text{m}$ for the seed beam, as shown in figure 4.2. The pump power was set to 14 W corresponding to $140\ \mu\text{J}$ and the achieved intensity was around $80\ \text{GW}/\text{cm}^2$. The OPCPA is set up in saturation, to ensure stable operation (figure 4.3). The achieved stability is below 1 % rms, similar the stability of the laser system 2.

The obtainable output energy highly depends on the chosen phase matching angle. The energies corresponding to the spectra depicted in figure 4.4 range from $1.7\ \mu\text{J}$ to $4.4\ \mu\text{J}$ (after compression). The highest amplifications were achieved with the narrow spectra, shown in the inset. The picture also illustrates the high tunability of the OPCPA for different wavelengths. Nevertheless a good compromise between pulse energy and the spectrum could be obtained, shown as thick black line, corresponding to $3.1\ \mu\text{J}$. To compress these pulses, a combination of sapphire and chirped mirrors was introduced. The design of the mirrors, was focused on the

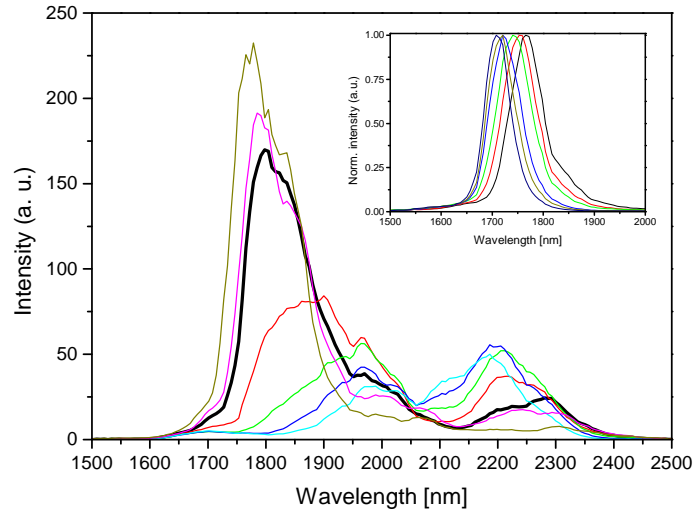


Figure 4.4: Tunability of the OPCPA for unoptimized dispersion.

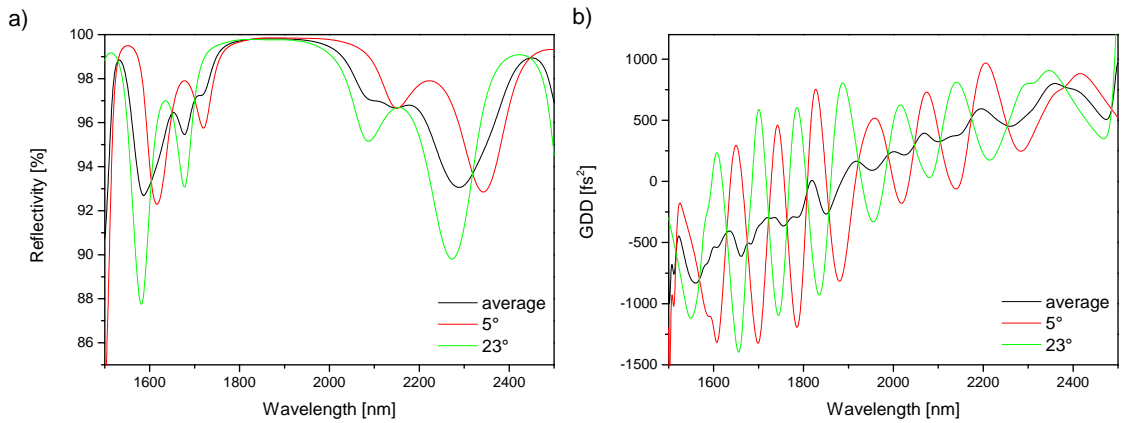


Figure 4.5: Chirped mirror design. As shown in a) the reflectivity over the whole frequency range is above 90% on average. b) The GDD of the mirrors is relatively flat. The goal of the design was to reach low GDD but high TOD compensation. This was only achievable with two angles of incidence. Courtesy of V. Pervak.

compensation of TOD, but only as little as possible GDD (figure 4.5). 15 mm of sapphire were used to compensate the GDD (the values are found in section 4.1.1), while 6 mirror bounces compensated the TOD. Sapphire is thereby favorable, since it is not only transparent at the amplified wavelengths range, but also exhibits the best ratio between GDD and TOD.

For fine tuning of the compression, wedges could be used, that anyway have to be introduced for the CEP control of the system (section 4.2). To verify the compression of the pulses, a THG-FROG was used to determine the pulse duration (figure 4.6). The retrieved pulse duration is 15.7 fs, which is close to the Fourier limit and a little bit above two cycles.

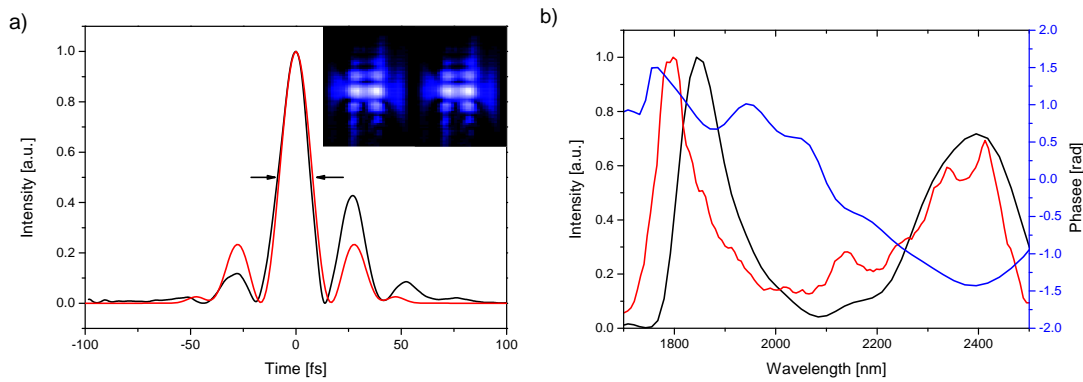


Figure 4.6: FROG measurement of the unoptimized OPCPA. In a) the retrieved temporal profile (black line) and Fourier-limited pulse (red line) are shown. The inset depicts the measured and retrieved FROG traces. The retrieved and measured mid-IR spectra (black and red lines, respectively) and retrieved residual spectral phase (blue line) are shown in b).

Main amplifier with material optimization

It is obvious, that a broad spectrum over the whole wavelength range should be obtainable. This was also predicted by the theoretical calculations in section 4.7 in collinear geometry, since the angle differences were proven to be negligible and the parameters mentioned before were used: The pump was set to 140 μJ at a beam size of 350 μm , corresponding to 86 GW/cm^2 . The beam size of the seed beam was 150 μm with an energy of 300 nJ and 3 mm thickness of the BBO. It was found, that up to 13 μJ of output energy should be achievable, with a GDD of 2000 fs^2 and a TOD of 0 fs^3 .

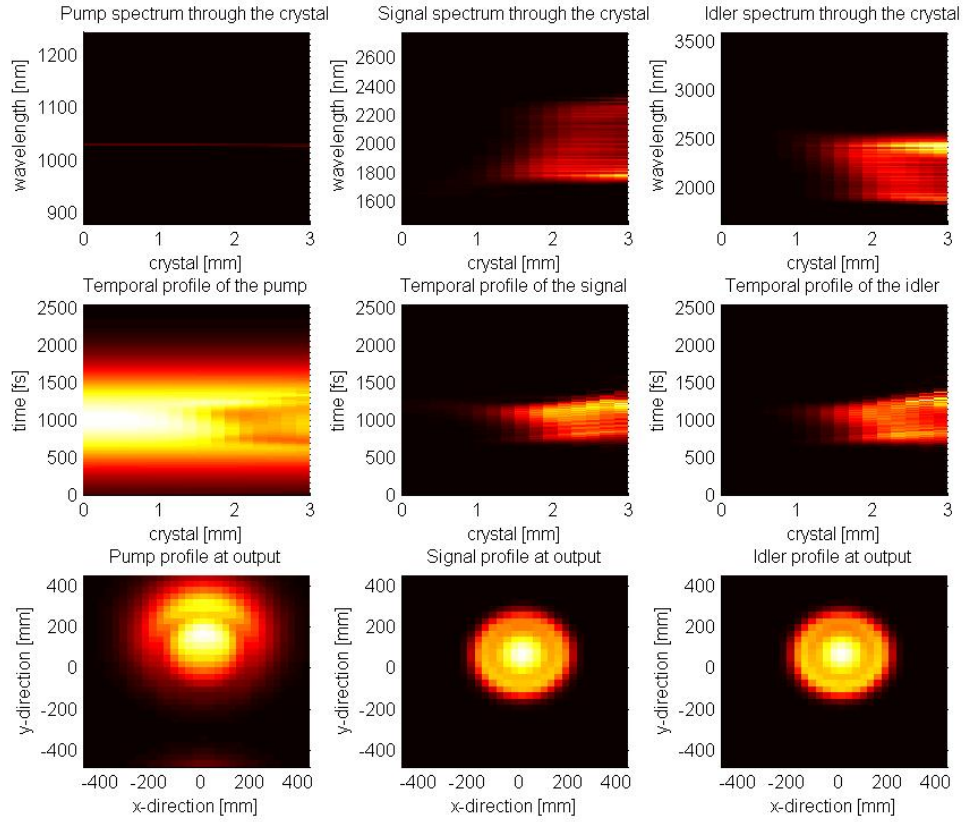


Figure 4.7: Model of the OPCPA. The retrieved output energy of the signal yielded $13 \mu\text{J}$.

The main difference between the simulation and the first version of the OPCPA is therefore the spectral phase of the pulses. When simulating the stage with the unoptimized spectral phase parameters, the efficiency significantly decreases, like in the experiment. This can be explained by the mismatch between the pulse lengths of seed and pump, since they haven't been optimized.

Besides that, especially a bad amplification around $2.2 \mu\text{m}$ is visible, which is not reproduced by the simulation above. There, a broad plateau over the whole long wavelengths part is apparent, which elevates in comparison to the peak at $1.8 \mu\text{m}$ with increasing pump energy. This behavior is a result of the TOD, as shown by simple calculations undertaken with LAB2, an add-on to LabVIEW®: The back-calculated phase of the white light leads to a "banana shape" temporal profile as shown in the upper left corner (figure 4.8).

Consequently, this shape is preserved in front of the OPCPA (second column) and afterwards compressed close to the Fourier limit. It is obvious that the amplifica-

tion for the OPCPA is therefore inefficient. Especially the long wavelengths cannot efficiently be amplified, since the duration of this part is short and thereby a lot of the seed photons interact with a limited number of pump photons. This also explains the spectral shape of the unoptimized OPCPA. Even the small elevation at long wavelength can be explained, because at lowest frequencies the pulses get a bit stretched again.

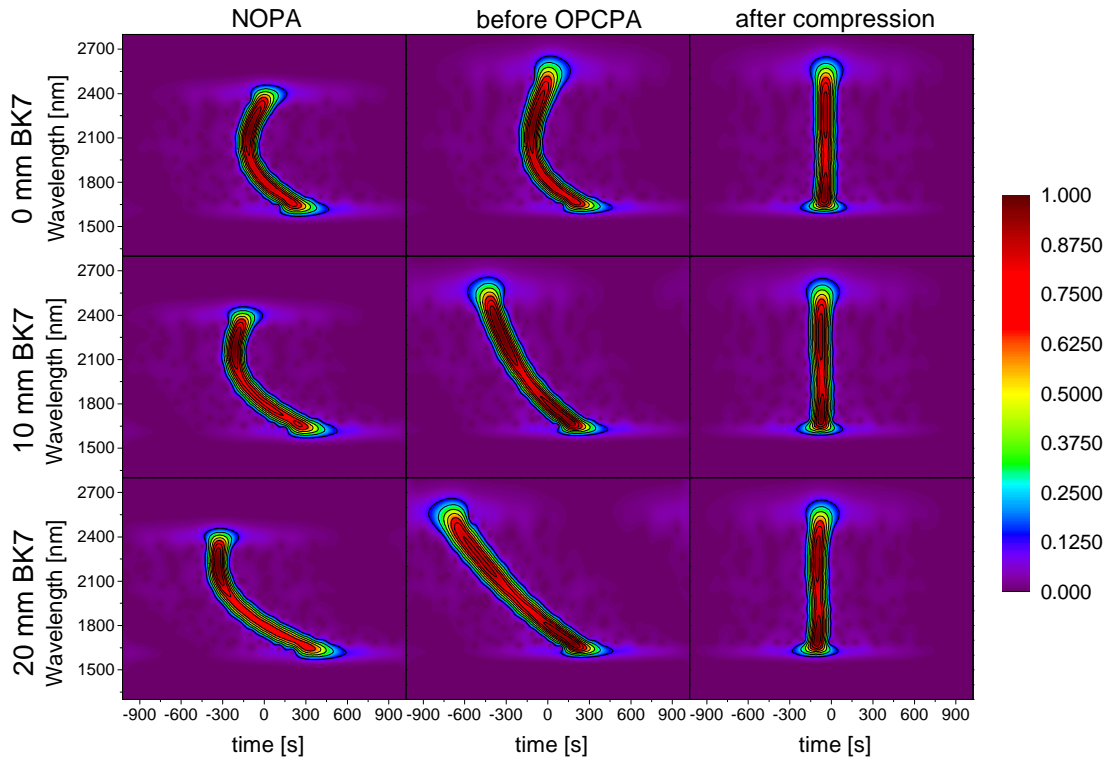


Figure 4.8: Windowed FFT for different dispersions, showing the spectral-temporal maps. The first row depicts the profile without introducing material, the second one for 10 mm of BK7 and the third for 20 mm BK7, in the white light. The first column shows the profile at the NOPA-position, the second one in front of the OPCPA and the last one after compression. For more details, see text.

To show this behavior, different amounts of material were introduced into the white light beam (figure 4.9). With increasing thickness, the gap between the two peaks at long and short wavelength is closed and the power increases. This can be explained by the different wavelengths that get stretched in time, while a better energy extraction is achieved, due to a better temporal overlap of pump and seed. This holds for up to 40 mm, where the power starts to drop again, because the

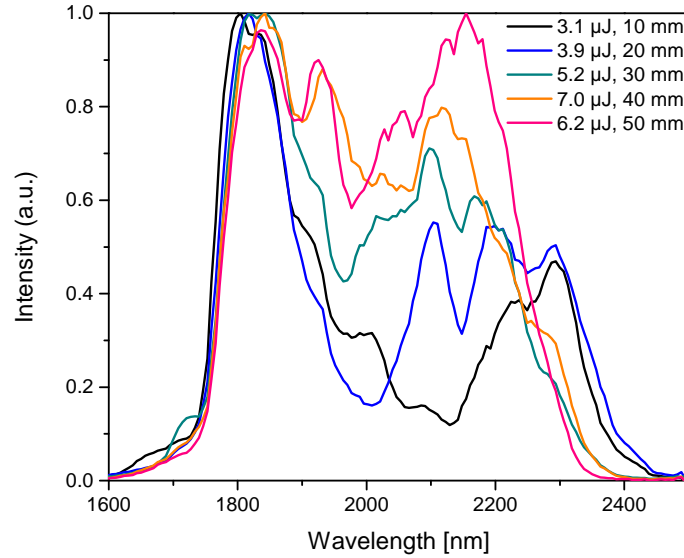


Figure 4.9: OPCPA spectra for different amounts of fused silica. The power of the consecutive spectra is shown in the legend.

pulses become too long. Anyway, this simple scheme of stretching the pulses is not optimal, because the pulses are not linearly stretched in time.

An additional degree of freedom is available with the usage of the chirped mirrors. When a few of them are introduced right behind the DFG, they significantly reduce the amount of TOD, leading to almost linearly chirped pulses in front of the OPCPA (second and third row, middle column in figure 4.8). By the usage of chirped mirrors in front of the OPCPA not only a linear chirp can be obtained, but also an almost optimal temporally stretched pulse can be achieved. Furthermore the compression after the OPCPA becomes more efficient, since the number of mirrors after the OPCPA stage is reduced.

The last two rows show the scheme for 10 and 20 mm of BK7 introduced in the supercontinuum for additional chirping of the pulses, respectively. In both cases four chirped mirrors are used to "linearize" the chirp. While 3 (4) mirrors and 17.5 (23.5) mm sapphire are compressing the pulse (last column).

As shown in figure 4.8, the additional BK7 can be compressed by almost the same amount of sapphire behind the OPCPA. For every 10 mm of additional material, another chirped mirror has to be added, to compensate the TOD. This has been done theoretically up to 40 mm of BK7, where still a compression with a deviation of 0.3 fs to the Fourier limit was achievable, allowing to match even longer pump

pulses. This could still be optimized by varying the materials. Since every glass exhibit a unique ratio between GDD and TOD, the material can be combined to get more flexibility.

As shown, the interplay between material and chirped mirrors allows to optimize spectral phase and pulse duration to ensure a high efficiency in the process. This way, it compensates to some extent the lack of an Acousto-Optic Programmable Dispersive Filter (AOPDF), usually used in OPCPAs. In comparison, the presented scheme has also the advantage, that high losses from this device are avoided and that it is completely passive.

The two curves for 10 and 20 mm of BK7 have a pulse duration close to the one of the pump pulse with 1.1 ps. Since seed and pump pulse are originating from the same laser source, timing jitter is expected to be very low. Therefore, it can be approximated, that maximal overlap should be obtained. To decide which amount of material is better, one has to rely on more sophisticated methods like SISYFOS and to verify them by the experiment.

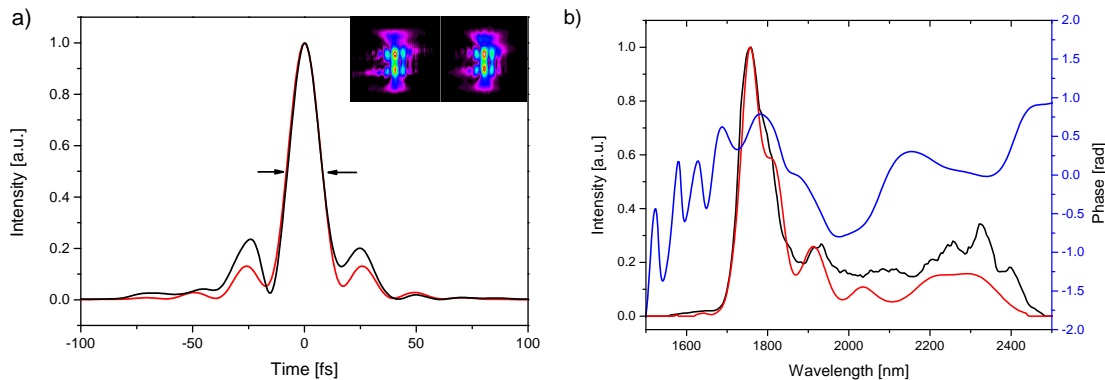


Figure 4.10: FROG measurement of the optimized OPCPA. In a) the retrieved temporal profile (black line) and Fourier-limited pulse (red line) are shown. The inset depicts the measured and retrieved FROG traces. The retrieved and measured mid-IR spectra (black and red lines, respectively) and retrieved residual spectral phase (blue line) are shown in b).

Here, the theoretical predictions could be confirmed by stretching the seed pulses with different amounts of material. Four chirped mirrors were used to reduce the amount of TOD. At 10 mm of introduced fused silica, the results improved significantly, while at 15 mm the spectrum started to narrow. Nevertheless, this amount could be used to obtain an optimal energy output. The pulses were compressed with 30 mm of sapphire and 3 additional chirped mirrors down to

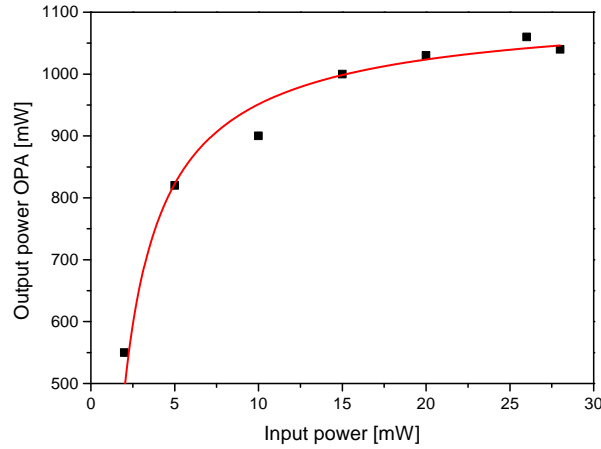


Figure 4.11: Power dependence from the seed for the optimized OPCPA.

15.5 fs, as shown in figure 4.10. The obtained compressed pulse energy was 10 μJ , which is in good agreement with the theoretical calculations presented above. The compressor has an efficiency of about 90%. The pulses are smoothly amplified over the whole spectral region, without a dip around $2.1 \mu\text{m}$. The spectrum is thereby similar to the one obtained in the DFG, while long wavelengths are more pronounced after the OPCPA stage. The low amount of TOD also leads to a significant increase of pulse energy, while the pulse duration is the same as before and close to the Fourier-limit. Besides these improvements also the pre-/post pulse could be minimized and the stability of the system is increased due to a deep saturation of the OPCPA, which already starts at around 10-15 mW of seed energy, as shown in figure 4.11.

The pulse stretching after the supercontinuum generation also led to better results in the NOPA and DFG stages, since the temporal overlap with the pump is also improved in those cases. Nevertheless, this effect had little influence on the OPCPA-stage, since all stages were already saturated before.

4.2 CEP measurement and stabilization

The second important parameter that has to be taken into account for the few-cycle OPCPAs is the carrier envelope-phase (CEP) stability. It plays a crucial role for strong-field experiments and describes the time evolution of the electric-field underneath the carrier wave.

4.2.1 Theory of CEP stability

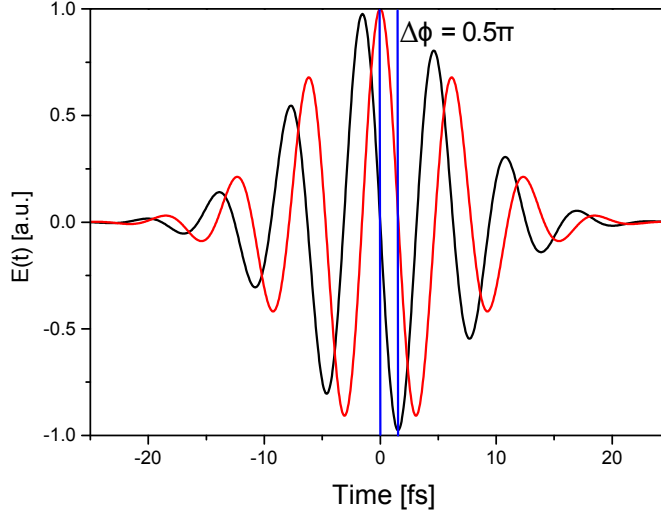


Figure 4.12: Electric field of a laser pulse.

For a laser pulse the electric field can be described as [31]:

$$E(t) = A(t)\cos(\omega_0 t + \phi), \quad (4.6)$$

where $A(t)$ is the amplitude envelope, ω_0 the central frequency of the pulse and ϕ the CEP. An example is given in figure 4.12 similar to the compressed DFG pulses used in the photoemission experiments.

Without any stabilization, laser systems produce a random CEP, which shifts between $0 < \Delta\phi < 2\pi$. This CEP shift is described in the frequency domain by:

$$\Delta\phi = 2\pi \frac{\nu_{\text{CEO}}}{f_{\text{rep}}}, \quad (4.7)$$

where f_{rep} is the repetition rate of the laser and ν_{CEO} the carrier-envelope offset frequency. To control ν_{CEO} the self-referencing technique was developed [29], where one part of the beam undergoes a nonlinear process e.g. SHG. Afterwards, it is overlapped with the fundamental, where the frequency comb for the fundamental is given by:

$$\nu(m) = mf_{\text{rep}} + \nu_{\text{CEO}} \quad (4.8)$$

and for the SH:

$$2\nu(m) = 2mf_{\text{rep}} + 2\nu_{\text{CEO}}, \quad (4.9)$$

respectively. If the original pulse has an octave spanning spectrum, its blue components overlap with the red components of the SH, leading to an amplitude modulation at f_{CEO} , since:

$$2\nu(m) - \nu(2m) = (2mf_{\text{rep}} + 2\nu_{\text{CEO}}) - (2mf_{\text{rep}} + \nu_{\text{CEO}}) = \nu_{\text{CEO}}. \quad (4.10)$$

This relation can be used to measure the CEP in the described f-2f interferometer. Furthermore, such setup is routinely applied in the active stabilization of the CEP. Besides the active synchronization the CEP can also be passively stabilized. For DFG the three-wave mixing is described as:

$$\omega_{\text{Idler}} = \omega_{\text{Pump}} - \omega_{\text{Signal}}. \quad (4.11)$$

Similarly, one can deduce that a similar relation is also found for the CEP [88, 89]:

$$\Phi_{\text{Idler}} = -\pi/2 + \Phi_{\text{Pump}} - \Phi_{\text{Signal}} \quad (4.12)$$

The equation implies, that, as long as signal and pump are correlated, the idler is CEP stable. Both beams therefore have to be originating from the same source. This way of CEP stabilization, although being easy to implement at a first glance, has to be taken into account over the whole system design to obtain good values. The correlation between the beams can easily be destroyed, leading to high CEP fluctuations, which will be discussed in the next section.

4.2.2 Impact on the laser design

The idea of using a passively CEP stable OPCPA is essential for the OPCPA design. It not only allows to omit the active stabilization of the CEP, but also requires passive temporal synchronization, as already pointed out in chapter 3. This reduces the timing jitter between seed and pump pulse, which, although not measured, is expected to be on the order of few femtoseconds [54].

The timing jitter is thereby also an important parameter for the CEP stability, as it leads to a different temporal overlap of the pump and seed pulses. The CEP then fluctuates together with the central frequency of the pulse, since its value depends on the propagation through a dispersive material, which itself is

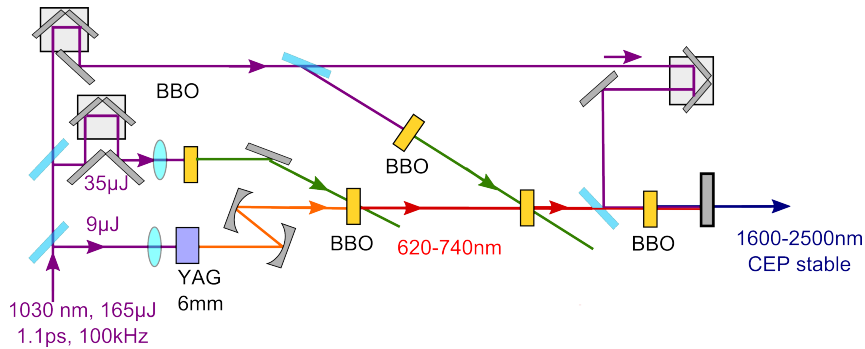


Figure 4.13: Alternative setup design. In contrast to the used one two NOPA stages are implemented followed by a single DFG stage.

wavelength dependent. As discussed in the literature [90], a shift of 1% in central wavelength can lead to a change of 0.8 rad in CEP. Although being measured for shorter pump pulses, this explains the difficulties to stabilize the CEP in [53]. It is also the reason, why so much attention was paid to the power dependences, as well as to the corresponding spectral dependences in chapter 3.

Nevertheless, this design also restricts the setup in some ways. One question that haven't been addressed in the design of the setup until now is: Why are we not using one or more additional stages in the visible wavelength region and only use the last stage to generate the idler. Figure 4.13 depicts this scenario. It has the advantage of working with well established materials, optics and detection methods, which are not easily available for long wavelength. Furthermore the visible beam is easier to handle in terms of alignment. The two important drawbacks of this approach are the following:

Firstly, the overall efficiency would probably decrease quite significantly, since one of the most inefficient steps, the DFG-process, is placed at the end of the setup. Furthermore, the additional SHG stage(s) would further decrease the efficiency. In addition these stages are also difficult to handle for high power beams. Secondly, even more important, the CEP stability is expected to be worse. After splitting the pulses into two different parts for supercontinuum generation and the DFG, the CEP can change independently for each arm. Therefore, the beams are interferometrically coupled, where small fluctuations can lead to high CEP instabilities. Therefore, the beam path before the DFG has to be kept as short as possible.

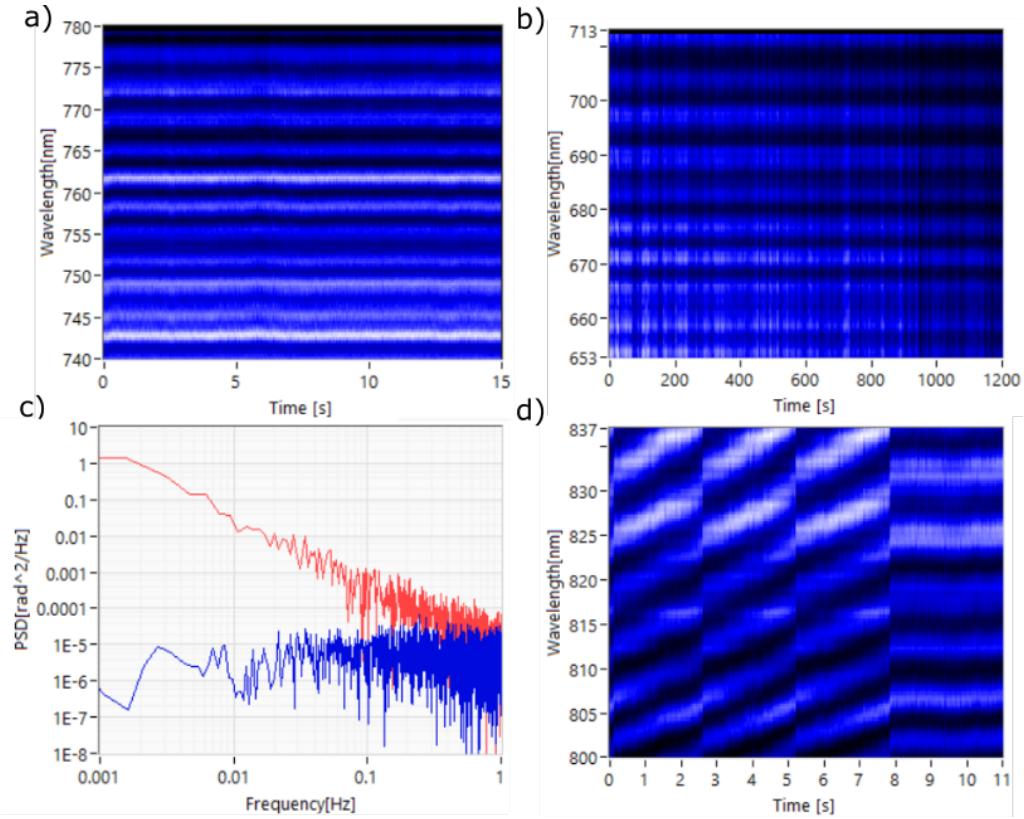


Figure 4.14: Results of the CEP measurement. The interference fringes are shown for: a) short time scales with a stability of 103 mrad over 15s and b) for long time scales with feedback-loop recorded with 136 mrad over 20 min. c) depicts the noise (power spectral density) with (blue) and without (red) stabilization. In d) the CEP control is shown with a $0-\pi$ ramp pattern, followed by constant CEP.

4.2.3 Slow feedback loop and CEP measurement

The CEP was measured by a collinear f-2f setup. The focused pulses were first broadened in a sapphire plate and, after refocusing, frequency doubled in a BBO (100 μm , uncoated). The fringes visibility was optimized by a cube polarizer. Already the first CEP stability measurements showed an excellent CEP stability on short time scales, but the long term stability was unacceptable and a slow loop control had to be implemented. In the present case this was achieved by varying the beam path length of the NOPA arm, which was implemented by a piezo-driven mirror. This leads to a strongly improved CEP stability on long timescales, which is shown in figure 4.14 c).

The measurements shown in figure 4.14 were undertaken with an in-loop f-2f interferometer controlling the slow-loop. In part a) a typical fast 15 s measurement is shown, resulting in 103 mrad fluctuations, where under optimal conditions

even a stability down to 80 mrad was achievable. This value increases for long timescales to 136 mrad (20 min, b)). The values obtained are thereby upper limits since the measurement is highly sensitive to variations in the SCG in the sapphire plate. Figure 4.14 d) shows an example of the CEP control with the piezo-mirror, followed by constant CEP). Due the high repetition rate of the laser system, it was impossible to measure the single shot CEP stability. The results presented here were taken with the lowest possible acquisition time of the spectrometer corresponding to 4 ms. Nevertheless, due to the passive CEP stabilization and the high stability of the laser system no fluctuations on shorter time scales are expected.

The values presented here are very comparable to the ones obtained elsewhere [36, 37, 91–93], where most systems, however, are using an active synchronization scheme with an AOPDF.

4.3 Summary

As shown in this chapter, the OPCPA scheme developed in this thesis is capable of delivering almost Fourier-limited, few-cycle, CEP stable pulses at 2 μm . Furthermore, it can be scaled towards higher pulse energies, as well as higher repetition rates, which will be discussed in chapter 7.

One of the main advantages, which allows the scalability, is the simplicity of the design. It is, besides the slow feedback loop for the CEP, an all optical approach without any limiting electronics. Nevertheless, it is possible to adjust the important parameters to achieve an optimal energy extraction from the pump pulses by optimizing the material dispersion. The scheme is, as exploited theoretically, applicable for a broad range of pulse durations of the pump beams, even for the given coating design of the chirped mirrors.

The obtained parameters from the amplification make the developed system a unique laser source. It delivers one of the highest pulse energies among high repetition rate, mid-IR sources. Furthermore, it delivers about 2-cycle, CEP stable pulses, while the CEP stability as well as the energy stability are excellent.

5 First photoionization experiments with the 100 kHz system

To show the applicability of the laser system, first prototype experiments were undertaken with the first version of the DFG setup. The experiments do not only profit from the different wavelength of the laser, but also from the high repetition rate.

This chapter gives a short overview of the results obtained. For a detailed description of the experiments, the reader is referred to [94, 95], while the underlying theory will be described in more detail in chapter 6.

5.1 Theoretical background

As already emphasized in chapter 1 an important approach for the understanding of the strong-field processes in atoms and molecules is based on the simple man's model (SMM) [22]. The adiabaticity is given by the Keldysh parameter γ in atomic units:

$$\gamma = \sqrt{\frac{I_p}{2U_p}} \quad (5.1)$$

with the ponderomotive potential U_p :

$$U_p = \frac{A^2}{4} = \frac{E_0^2}{4\omega^2}, \quad (5.2)$$

with A being the vector potential ($A = A_0 * \cos(\omega t)$), I_p the ionization potential, E_0 the electric field strength and ω the laser frequency. It describes the transition from the multiphoton photoemission picture to the quantum mechanical tunneling picture [96, 97].

For $\gamma \gg 1$ multiphoton ionization (MPI) is the dominant photoemission mechanism. The electric field of the laser is small compared to the Coulomb-field and

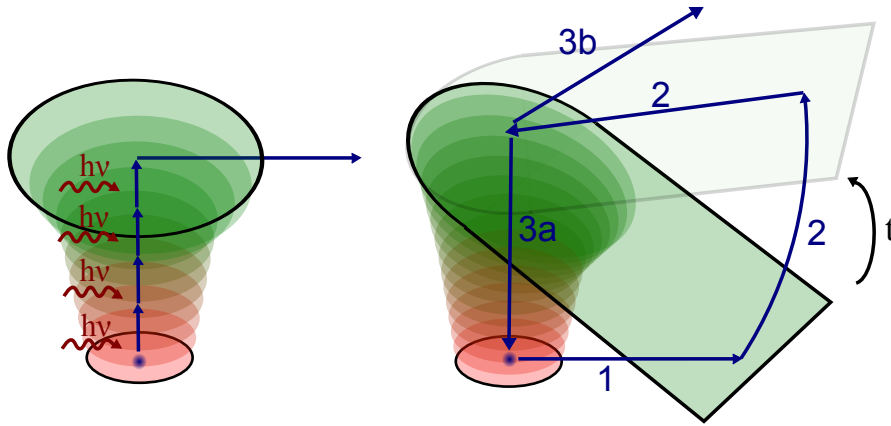


Figure 5.1: Schemes of multiphoton ionization (left) and above-threshold-ionization described by simple man's model (right). In the multiphoton regime, the electron absorbs the minimal amount of photons to overcome the ionization potential. For low Keldysh parameters the electron can tunnel through the potential (1). The electron is driven away from the molecule gaining additional energy in the oscillating field (2). After some time the electron recollides with the parent molecule (3). Here, several effects can be observed: 3a denotes the recombination which results in high harmonic generation. In addition recollision of the electron can be observed by rescattering (3b) as well as non-sequential double ionization (NSDI).

can be treated by perturbation theory. The photoemission of electrons in this regime is limited to the absorption of the minimal number of photons, needed to extract the electron from the molecule, as shown in figure 5.1. Going towards lower values of γ to ~ 1 , by either increasing the intensity or the wavelength of driving laser, the emission process changes. Above-threshold-ionization (ATI) becomes the main driving force in the photoemission spectra. It can be seen by equidistant peaks with an energy spacing of the photon energy and the appearance of a high energy plateau for $\gamma \ll 1$.

In the intense laser fields at low Keldysh parameters, the influence of the electric field of the laser compared to the Coulomb field cannot be neglected anymore. In this case, the potential barrier of the molecule is bent, so that the electrons can tunnel out of the system, while the rate is determined by the instantaneous electric field of the driving laser. Therefore, the whole process is not only dependent on the wavelength and intensity of the laser, but also on the CEP.

The tunneling process in the Keldysh theory is described as a direct transition from the ground state to a continuum state (Volkov-state) in the electric field of the laser [97]. Typically, additional bound states and the Coulomb potential are

neglected (Strong-Field Approximation (SFA)). In addition, the initial state is also not influenced by the laser field under these assumptions.

The liberated electron in the electric field of the laser pulse then shows a quiver motion. Depending on the birth time, which corresponds to a specific point in the electric field, it can either escape out of the system or recollide with the molecule (for more details see chapter 6).

Similar processes can be found in solids. Equation 5.1 can be adopted to solids [98, 99] by substituting the ionization potential by the work function ϕ of the solid, yielding:

$$\gamma = \sqrt{\frac{\phi}{2U_p}} \quad (5.3)$$

where the intermediate (ATI) regime is referred to as Above-Threshold Photoemission (ATP).

Nanostructures exhibit field enhancement and field confinement due to the interaction of the incoming light with the electrons of the nanostructure. The first one leads to an increased electric nearfield. Therefore, the strong-field processes are possible at correspondingly lower intensities compared to gas phase atoms or molecules. Field confinement manifests itself in the decay of the near-field away from the surface with a decay length l_F . If the length scale of the electron motion during a half-cycle is on the order of the decay length, the dynamics of the electron in the field can be significantly altered compared to the strong-field photoemission from an atom or molecule in a quasi-homogeneous laser focus (on the length scale of the quiver motion).

The competition between near-fields and quiver energy was observed in 2012 by Herink et al. in dependence of the laser wavelength [100]. For long wavelengths the quiver amplitude exceeds the decay length of the near-field (l_F), so that they feel its decay. When the electrons are driven away from the surface, they experience a smaller field in the next half-cycle, that pushes them back to the tip, as the field decreases with the distance to the surface. This behavior leads to a quenching of the quiver motion. As a result, the rescattering energy and probability decreases, leading to a reduction of the cutoff. This effect can be described by a dimensionless adiabaticity parameter δ [100]:

$$\delta = \frac{l_F}{l_q} = \frac{l_F m \omega^2}{e E_0}, \quad (5.4)$$

where l_q is the electron quiver amplitude in a homogeneous monochromatic laser field. With this formula two different regimes can be separated. In the instantaneous regime ($\delta \ll 1$) at high intensities or long wavelengths, the electron leaves the near-field within a half-cycle of the electric field. It can therefore be considered as being accelerated by a static electric field with a final energy of:

$$E_{\text{final}} \sim E_0 \cdot l_F \quad (5.5)$$

In the adiabatic regime ($\delta \gg 1$), the ponderomotive potential is adiabatically transformed into kinetic energy of the drift motion. The electron undergoes subcycle motion as in a homogeneous field. The field inhomogeneity only affects the cycle-averaged drift motion as the electron drifts away from the surface:

$$E_{\text{final}} \sim U_p = E_0^2 \quad (5.6)$$

For laser pulses the energy gained by the electron is also limited by the pulse duration in the adiabatic regime. If the pulse is gone before the electron leaves the near-field of the tip, the obtained energy is reduced. In comparison, this effect has no influence in the instantaneous regime.

5.2 Experimental setup

The experiments were done with the first available laser-setup. There, only the DFG was available with an output energy of 36 mW and slightly different spectrum (figure 5.2).

The stability of the 2 μm beam was 1.1% rms. These pulses could be compressed in the same way as described in chapter 4 by a combination of material and chirped mirrors down to 18,4 fs FWHM, corresponding to 3.1 optical cycle pulses. In addition, phase stability measurements were undertaken which yielded 533 mrad rms on short time scales. Long term observation of the CEP was not possible due to high fluctuations in the supercontinuum.

These pulses were coupled into a vacuum chamber, as shown in figure 5.3, with background pressures down to 10^{-7} mbar. The window (3 mm of Sapphire) was part of the compression scheme. The collimated beam was focused by an off-axis parabolic mirror (OAP) ($f=15$ mm) onto the target. Besides gas nozzle

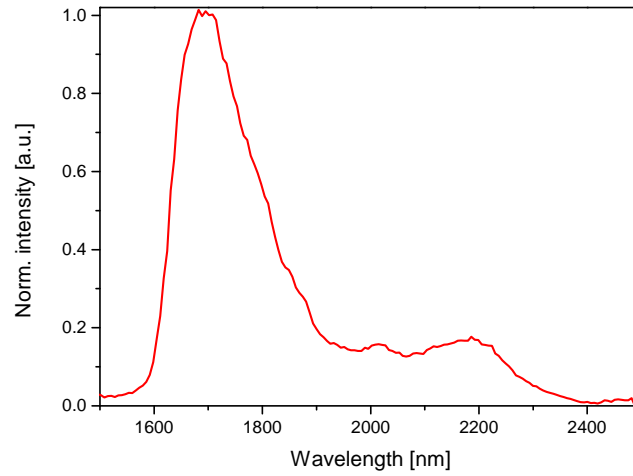


Figure 5.2: Spectrum of the first DFG stage.

and nanotips, also a YAG-plate could be inserted to obtain a THG-signal from the surface which was used to optimize the compression by wedges (not shown) in front of the chamber. After the tip, the beam is collimated and recorded with a CMOS camera for alignment of the targets.

The apex of the nanotip target is placed in the focus of the OAP. The polarization of the electric field is parallel to the tip.

The photoelectron spectra are obtained by a time of flight spectrometer (Kaesdorf ETF10). The flight times are recorded by a time to digital converter (TDC, FAST Comtec P7889) with a resolution of 100 ps. To calibrate the spectra presented in the following a white light peak from the surface of the gas nozzle was used for time zeroing.

5.3 Results

5.3.1 Xenon gas

To prove the applicability of the laser and to calibrate the intensity in the experiments, electron emission from xenon was measured in the beginning. The spectra obtained show the expected features, as shown in figure 5.4 for an intensity of around $5 \cdot 10^{13} \text{ W/cm}^2$. Besides the $2 U_p$ cutoff around 40 eV, several ATI-peaks were observable, with a spacing of $\approx 0.8 \text{ eV}$ in good agreement to the expected value ($\sim 0.7 \text{ eV}$). The $10 U_p$ cutoff is, however, not visible.

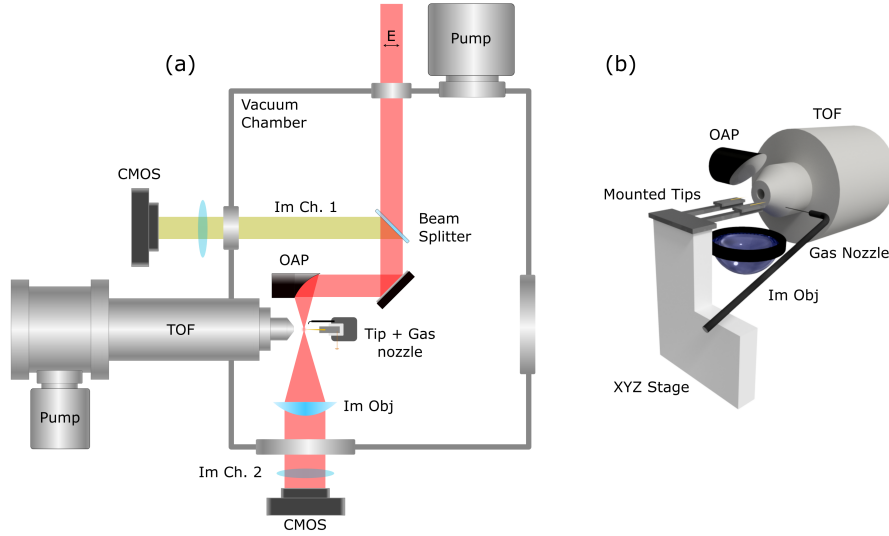


Figure 5.3: Experimental setup for the photoionization experiments. a) The beam enters the vacuum chamber through a sapphire window. The focusing on the target is done by an on-axis and off-axis parabolic mirror (OAP). b) 3 dimensional picture of the experimental setup. Courtesy of S. Mitra.

Interestingly, these peaks showed a CEP-dependence as depicted in figure 5.4b), which could be reproduced by theoretical calculations. The asymmetry (A) is calculated from the signals for a given phase ($S(\phi)$) as:

$$A = \frac{S(\phi) - S(\phi + \pi)}{S(\phi) + S(\phi + \pi)} \quad (5.7)$$

This was surprising, as the CEP-stability was measured to be around 500 mrad rms on short time scales with long term drifts. It can thereby be concluded, that the real CEP-stability was lower than the measured one. It can be explained by the high fluctuations in the supercontinuum generation of the f-2f interferometer at that time. This would also be in good agreement to the results obtained in 4.2, where a significant improvement in the stability measurement could be achieved due to higher pulse energies.

5.3.2 Nanotips

The photoelectron spectra from the gold nanotips were taken at a rate of up to 50000 electron counts per second, calibrated with the xenon measurements shown above. The on-target intensities are limited by the damage threshold of the tips. In

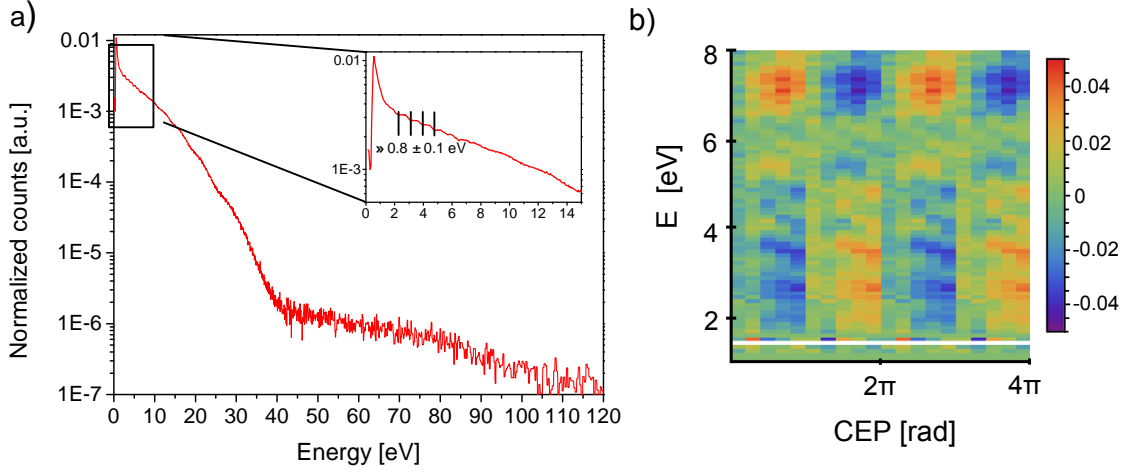


Figure 5.4: Results on xenon gas. a) Typical xenon spectrum obtained with the DFG beam. ATI peaks are observed with a spacing of about $0.8 (+/- 0.1)$ eV. The central wavelength is at 1800 nm corresponding to 0.69 eV. Due to the high asymmetry of the spectrum, the emission can be expected to be mainly driven by the 1700 nm peak (0.73 eV) b) Asymmetry map of the ATI peaks in xenon. Picture taken from [94].

contrast to standard Ti:Sa measurements, the long wavelengths used here, lead to a small Keldysh parameter deep in the tunneling regime and also small adiabaticity parameters before hitting the damage threshold of the tips.

When plotting the obtained spectra, two interesting features can be seen, as shown in figure 5.5. First, for higher intensities, a strong shoulder forms, and cutoff depends linearly on the laser intensity. Second, all spectra have a sharp peak at low energies. In the beginning, this peak shifts linearly towards higher energies with intensity and its width increases, which hasn't been reported so far. At intermediate intensities this behavior is slowed down significantly, while a secondary peak appears at low energies.

The shift of the low-energy peak can be understood in terms of the ponderomotive potential. In figure 5.6 the theoretical results for the minimal kinetic energy of the electrons emitted in the central cycle of the laser pulse are depicted. As shown, for all pulse lengths, the energy shift has a distinct peak. It originates from the minimal kinetic energy and shifts towards lower adiabaticity parameters for shorter pulse lengths. This can be explained by two competing effects. In the limit of a continuous wave laser and $\delta \gg 1$, the ponderomotive potential is

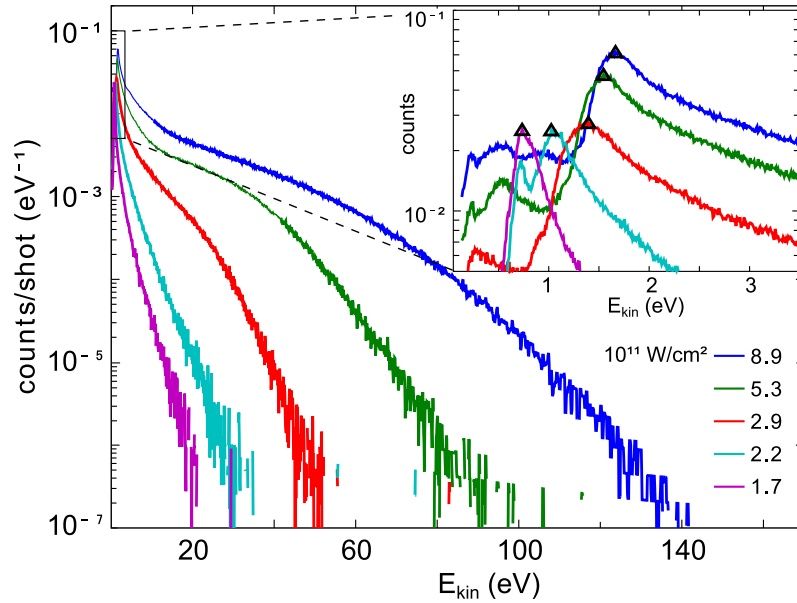


Figure 5.5: Intensity dependent photoelectron spectra for the gold nanotips. As shown, in the inset the low energy peak exhibits a strong change in the behavior at $2.9 \times 10^{11} \text{ W/cm}^2$. Courtesy of J. Schötz.

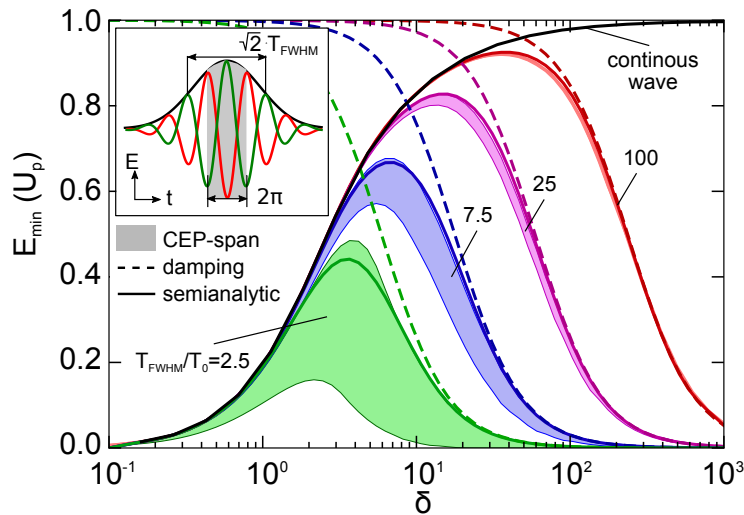


Figure 5.6: Change of the minimal final energy for different adiabaticity parameter in the central cycle for different pulse lengths and CEPs. T_0 denotes the period of the laser pulse. Courtesy of J. Schötz.

adiabatically transferred to the electron leading with a minimal energy of $1 U_p$. When going towards lower values of δ , the electron feels the inhomogeneity of the near-field at the tip during their quiver motion, so that the additionally gained energy is decreased and approaches 0 for $\delta \ll 1$. This non-adiabatic effect of the subcycle-propagation, as discussed in 5.1, not only influences the final maximum photoelectron energy and probability for the rescattering electrons as discussed in Herink et al. [100], but also the low-energy electrons via the ponderomotive shift. For laser pulses of finite duration, another effect has to be taken into account. In case of short pulse lengths, the ponderomotive potential can not be treated as time independent. It decreases significantly during the electrons motion, which then cannot gain the full energy of the initial potential anymore. Therefore, in case of common laser systems with short wavelengths, the ponderomotive shift can usually be neglected ($\delta \gg 1$).

In contrast to these systems and to gas targets, the sub-cycle quiver motion and the cycle-averaged drift motion can not be separated in our experiment, as the ponderomotive shift becomes non-adiabatic due to the small decay length of the near-field. Due to the short pulse length and the long wavelength, the ponderomotive shift is clearly visible in our experiment. At low intensities the obtained energy is limited by the drift motion. This leads to a strong linear increase of the peak position with increasing intensity. At intermediate intensities the peak is reached and the maximal ponderomotive shift is acquired. The sub-cycle propagation becomes dominant and in the following, the additionally acquired energy is only a result of the stronger electric field strength and thereby comparably small. The appearance of the secondary peaks at lower energies can be attributed to different half cycles of the laser-field as indicated by theoretical simulations.

Not all features can be explained by the simple considerations above. In the spectra the peak significantly broadens, which is not reproduced by the simple model and has to be analyzed in detail with further experiments.

5.4 Discussion

The results shown here, prove the importance of laser systems like the one built in this thesis. Even the seed for the main OPCPA is able to give new insights into the strong-field physics of nanomaterials. Since the wavelength is more than two times higher than the one of standard Ti:Sa systems usually used for these types of investigations, the experiment is shifted into the tunneling regime and enables the

exploration of low adiabaticity parameter regimes. This leads to the observation of low energy peaks, whereas their shift has not been reported in the literature so far.

The importance of this difference was also shown in the work of S. Mitra [95] by the direct comparison to a 10 kHz Ti:Sa-system (Femtopower, Femtolasers). It was not possible to reach the tunneling regime ($\gamma \approx 1$), so that the features reported here were not observable. Furthermore, the higher repetition rates allowed a significant decrease in the measurement time from about an hour to a couple of minutes with comparable parameters. This results in less requirements for the laser stability and better statistics. In addition, it was also possible to measure at way lower counts per shot, which is also important for other techniques as will be discussed in chapter 7.

In the future these experiments will be continued with the improved version of the OPA, where especially the phase-stability will increase the possibilities and give new insights into the underlying physics.

6 Laser induced electron diffraction of the buckminsterfullerene C₆₀

This chapter describes another experiment which benefits from high repetition rate mid-IR laser systems and includes the necessity of high pulse energies. Laser induced electron diffraction (LIED) is in contrast to the experiment described in the previous chapter, not aiming for the electronic properties of the sample, but its structure. Its first implementation is the combination of the methods originating from strong-field physics with gas-phase electron diffraction (GED) [27], called angle-swept LIED (ASLIED). Instead of an electron gun producing the electrons, the recolliding electrons were used to image the molecule under investigation. Obviously, due to the usage of a short laser pulse, this technique has the advantage, that time resolved information can in principle be extracted, which is difficult for GED .

In 2014 another LIED technique was established, which makes further advantage of the unique combination of methods, simplifying retrieval and measurement at once. fixed-angle broadband laser-driven electron scattering (FABLES) uses the broad electron energy distribution for structure determination [28].

The power of these techniques hasn't been investigated to a big extend since suitable laser sources are not very common, yet. Nevertheless, in the present work the application of these techniques on the buckminsterfullerene C₆₀ could successfully be demonstrated. This study not only extends the methods to large molecules, but shows the possibility of imaging structural dynamics in such systems. Until now, no direct observation of the strong-field interaction of C₆₀ was possible. Here, for the first time, the theoretical predictions made before could be experimentally confirmed, directly showing the structural deformation of C₆₀ in intense fields.

Nevertheless, the experiment reveals the current limitations, where laser systems, like the one presented before, could further improve the results and the time duration necessary for such experiments.

All the work has been done in collaboration with the group of Prof. Louis DiMauro from the Ohio State University (Columbus). Some results presented here are also contained in [101].

To understand which formulas from the simple man's model are necessary for the structural retrieval, first the GED is described in the beginning. Afterwards the theoretical approach for LIED is established and previous experiments are shown. In the next section, the known behavior of C_{60} in strong fields is described and finally, the experiment is illustrated and the results are presented and discussed.

6.1 Gas-phase electron diffraction

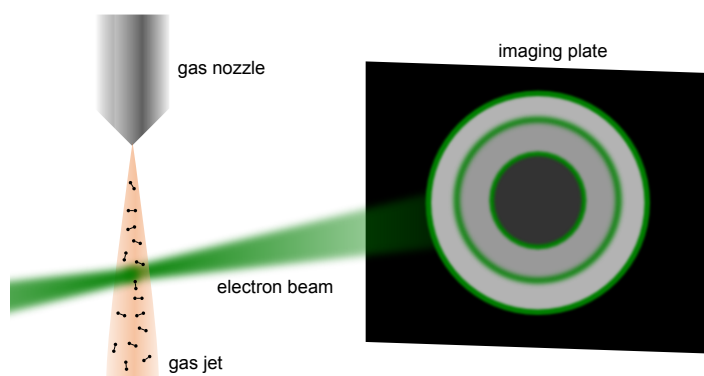


Figure 6.1: Principle of Gas-phase electron diffraction. An electron beam is guided into the gaseous sample. The diffraction pattern is collected on an imaging plate.

The section is closely related to [102] and summarizes the important physics.

GED was developed shortly after the invention of electron diffraction in 1930 [26] and first x-ray diffraction measurements in gas-phase. Therefore the basic apparatus itself is quite simple, as shown in figure 6.1. It uses a collimated beam, which is illuminating the gaseous sample. Afterwards the diffracted image is recorded on an imaging plate.

The structure can be retrieved by using the independent atom model (IAM). It is based on the assumption that the (elastic) scattering amplitudes of each atom in a molecule are independent of each other and no molecular binding is present. Therefore, the total scattering amplitude is approximated as a sum of the atomic ones:

A plane electron wave with the momentum k_0 along the z-axis hits a fixed molecule

consisting of N atoms, leading to a momentum $|\mathbf{k}| = |\mathbf{k}_0| = (k, \theta, \varphi)$. The amplitude of the scattered wave diffracted at distance R , can be written as:

$$\psi(R) = C \frac{e^{ik_0 R}}{R} \sum_i f_i(\theta) e^{i\mathbf{s}\mathbf{r}_{ij}}, \quad (6.1)$$

while $s = |\mathbf{s}| = |\mathbf{k} - \mathbf{k}_0|$ is the momentum transfer. f_i denotes the scattering amplitude of the i^{th} atom at position \mathbf{r}_i and C is a constant. The azimuthal angle φ is not important due to symmetry. The intensity is thereby calculated as:

$$I(s) = \frac{C^2 I_0}{R^2} \sum_{i=1}^N f_i(s) e^{i\mathbf{s}\mathbf{r}_i} \sum_{i=1}^N f_i^*(s) e^{-i\mathbf{s}\mathbf{r}_i} = \frac{C^2 I_0}{R^2} \sum_{i=1}^N \sum_{j=1}^N f_i(s) f_j^*(s) e^{i\mathbf{s}\mathbf{r}_{ij}}, \quad (6.2)$$

with $\mathbf{r}_{ij} = \mathbf{r}_i - \mathbf{r}_j$. For randomly oriented molecules this formula changes to:

$$I(s) = \frac{C^2 I_0}{R^2} \sum_{i=1}^N \sum_{j=1}^N f_i(s) f_j^*(s) \frac{\sin(sr_{ij})}{sr_{ij}}, \quad (6.3)$$

due to the relation $|\mathbf{s}| = 2k_0 \sin(\theta/2)$. Here, two components can be separated:

$$I(s) = \frac{C^2 I_0}{R^2} \left(\sum_{i=1}^N |f_i|^2(s) + \sum_{i=1}^N \sum_{j=1}^N f_i(s) f_j^*(s) \frac{\sin(sr_{ij})}{sr_{ij}} \right) \quad (6.4)$$

where $i \neq j$. The last equation is the central point in the GED retrieval. It shows, that the recorded spectra are made up of two independent contributions. The first one is the atomic scattering (I_A), which is the sum of the scattering cross sections, derived from the sum of the atoms. Usually another component S_i is added:

$$I_A(s) = \frac{C^2 I_0}{R^2} \sum_{i=1}^N (|f_i|^2(s) + S_i), \quad (6.5)$$

which describes the incoherent scattering. The second one contains the structural information (I_M):

$$I_M(s) = \frac{C^2 I_0}{R^2} \sum_{i=1}^N \sum_{j=1}^N f_i(s) f_j^*(s) \frac{\sin(sr_{ij})}{sr_{ij}}, \quad (6.6)$$

which shows an oscillatory behavior. In GED therefore often the Molecular Con-

trast Factor is used which is defined as:

$$MCF = \frac{I_M}{I_A}. \quad (6.7)$$

The radial distribution, describing the internuclear distances in the molecule, is retrieved by Fourier transforming:

$$f(r) = \int_0^\infty s I_M(s) e^{-as^2} \sin(rs) ds \quad (6.8)$$

where a is a damping constant.

6.2 Laser induced electron diffraction

LIED relies on recollision of the electrons with the sample under investigation. Nevertheless, in this case it is even more important to reach high intensities at long wavelength to reach highest ponderomotive energies according to eq. 5.2, as will be described in the following section. An intuitive picture of the SMM has already been given. Here a more formal approach is chosen on the important processes of LIED, whereas atomic units are used throughout the following.

6.2.1 Tunneling

As already reported in 5.1 the first step in the SMM is the tunneling ionization of the atom, where the KFR theory with SFA is often used to describe the tunneling. Two extensions to the Keldysh theory have to be mentioned for the description of the tunneling regime: Perelomov, Popov and Terent'ev (PPT) [103] and Ammosov, Delone and Krainov (ADK) [104]. The former one can particularly be used to calculate the ionization rate for hydrogen and in contrast to the Keldysh theory, includes the long-range Coulomb interaction. The ADK- theory is used in the quasi-static limit ($\gamma = 0$) of PPT, allowing to model other atoms and ions [97]: In the PPT model the rate of ionization is given by:

$$w(E, \omega) = \sum_{q \geq q_{thr}}^\infty w_q(E, \omega) \quad (6.9)$$

where F is the field strength of the laser, q the number of absorbed photons and q_{thr} the minimal number of photons required to ionize the atom. This number

is defined by the ionization potential of the atom (I_p) and the ponderomotive potential (equation 5.2). The ionization rate depends on the initial state of the atom. For hydrogen this is characterized by the electron configuration donated with the quantum numbers n , l and m . It can be shown that the rate can be calculated as follows:

$$w(E, \omega) = |C_{n^*l^*}|^2 G_{lm} I_p \left(\frac{2E_0}{E} \right)^{2n^*-|m|-1} \left(\frac{1}{\sqrt{1+\gamma^2}} \right)^{-|m|-1} \frac{4}{|m!| \sqrt{3\pi}} \cdot \frac{\gamma^2}{1+\gamma^2} e^{\frac{2E_0}{3E} g(\gamma)} \sum_{q \geq q_{thr}}^{\infty} A_q(\omega, \gamma) \quad (6.10)$$

The coefficients $|C_{n^*l^*}|^2$ and G_{lm} only depend on the quantum numbers of the electron, whereas $g(\gamma)$ and $A_q(\omega, \gamma)$ depend on the Keldysh parameter $\gamma = \omega(E_0^{1/3}E)$ (for details see [97]).

The rate thereby depends only on the interaction of the electron, the Coulomb potential and the laser field. In the ADK-model, this expression is simplified for the tunneling regime by basically setting all terms including γ to one. This is important since the model can than only be used in the tunneling regime ($\gamma < 0.5$).

The ADK theory was later on, extended to (diatomic) molecules (MO-ADK) [105]. Within this model the wave function of a valence electron for large distances, where the tunneling occurs, is expressed as:

$$\Psi^m(\mathbf{r}) = \sum_l C_l E_l(r) Y_{lm}(\hat{\mathbf{r}}) \quad (6.11)$$

The term $Y_{lm}(\hat{\mathbf{r}})$ denotes the spherical harmonic of an electron quantized along the field. With

$$E_l(r \rightarrow \infty) \approx r^{Z_c/\kappa-1} e^{-\kappa r}. \quad (6.12)$$

($\kappa = \sqrt{2I_p}$ and Z_c = effective coulomb charge) a formula for the ionization rate for an unaligned molecule under angle \mathbf{R} is obtained,

$$w(E, \mathbf{R}) = \left(\frac{3E}{\pi \kappa^3} \right)^{1/2} \omega_{stat}(E, \mathbf{R}), \quad (6.13)$$

where E is again the field strength and ω_{stat} the static field ionization rate. As shown in [106] this theory can be extended to other molecules.

One of the most important differences to the atomic case is the ionization rate

dependency on the orientation of the molecule, due to the anisotropic charge density distribution.

6.2.2 The returning electron

After tunneling the electron is accelerated by the field away from the atom/molecule and returns after some time. The time can be calculated using the classical motion of an electron in an oscillatory field [107, 108]. By integrating the classical equation of motion two times, setting initial momentum and position at time zero (t_0) to zero:

$$\ddot{x} = -E \sin(\omega t), \quad (6.14)$$

one obtains:

$$x(t) = \frac{E}{\omega^2} (\sin(\omega t) - \sin(\omega t_0)) - \frac{E}{\omega} (\cos(\omega t_0)t + \cos(\omega t_0)t_0). \quad (6.15)$$

The kinetic energy is given by [97]:

$$E_{kin} = 2U_p [\sin(\omega_0 t) - \sin(\omega_0 t_0)]^2. \quad (6.16)$$

Electrons that return to the origin can recollide with the parent ion. The time of rescattering t_r can be obtained from equation 6.15 by setting $x(t_r) = 0$. The highest kinetic energy achievable at that time is given by $3.17U_p$ [97, 109].

To be able to calculate the kinetic energy of the incoming electron in the LIED procedure, it is essential to derive an equation to calculate the returning momentum in dependence of the detected momentum.

The canonical momentum of an electron in an electromagnetic field is classically derived by:

$$\mathbf{p}_c = \mathbf{p} - \mathbf{A}, \quad (6.17)$$

where \mathbf{A} is the vector potential. For an elastic scattering process the vector potential before (b) and after (a) the recollision (r) is constant. Therefore the momenta are obtained as: ($A(t_{r,b}) = A(t_{r,a}) = A(t_r)$).

$$\mathbf{p}(t_{r,b}) - \mathbf{A}(t_r) = \mathbf{p}(t_0) - \mathbf{A}(t_0) \quad (6.18)$$

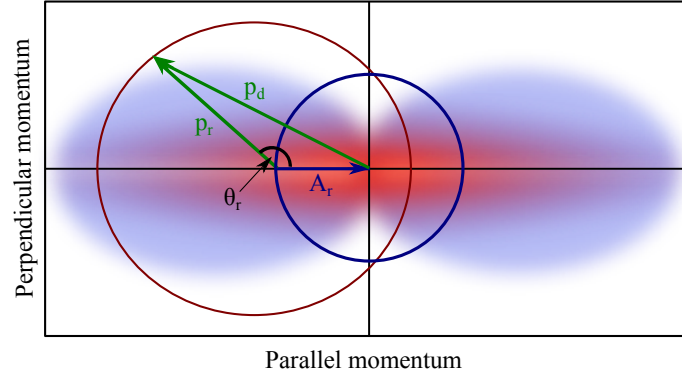


Figure 6.2: Scheme for the rescattering process. The detected momentum is given by $\mathbf{p}_d = \mathbf{p}_r - \mathbf{A}_r$. The shaded area denotes a typical distribution measured with LIED. The highest energies are found ($10 U_p$), when the perpendicular momentum equals zero (backscattering geometry), while the central part (blue circle) contains the direct electrons ($2U_p$). The picture for C_{60} is found in figure 6.5.

and

$$\mathbf{p}(t_d) - \mathbf{A}(t_d) = \mathbf{p}(t_{r,a}) - \mathbf{A}(t_r). \quad (6.19)$$

The vector potential at the detection and the momentum at the beginning are zero: ($\mathbf{A}(t_d) = 0$, $\mathbf{p}(t_0) = 0$). The momentum at recollision thereby depends only on the initial and final vector potential:

$$\mathbf{p}(t_{r,b}) = \mathbf{A}(t_r) - \mathbf{A}(t_0) \quad (6.20)$$

The detected momentum is given by:

$$\mathbf{p}(t_d) = \mathbf{p}(t_{r,a}) - \mathbf{A}(t_r) \quad (6.21)$$

As shown in figure 6.2 the detected momentum also depends on the angle, in which the electron is scattered (θ_r), yielding:

$$\mathbf{p}(t_d) = [p(t_r)\cos\theta_r - A(t_r)]\hat{\mathbf{r}}_{\parallel} + p(t_r)\sin\theta_r\hat{\mathbf{r}}_{\perp} \quad (6.22)$$

$$= [[\mathbf{A}(t_r) - \mathbf{A}(t_0)]\cos\theta_r - A(t_r)]\hat{\mathbf{r}}_{\parallel} + [\mathbf{A}(t_r) - \mathbf{A}(t_0)]\sin\theta_r\hat{\mathbf{r}}_{\perp}. \quad (6.23)$$

In the special case of backscattering ($\theta_r = \pi$) the formula yields:

$$\mathbf{p}(t_d) = -2\mathbf{A}(t_r) + \mathbf{A}(t_0) \quad (6.24)$$

where the detected energy can be derived with equation 5.2 as:

$$E(t_d) = \frac{p(t_d)^2}{2} = \frac{[2A(t_r) + A(t_0)]^2}{2} = 2U_p[2\cos(\omega t_r) - \cos(\omega t_0)]^2 \quad (6.25)$$

The last missing link to apply the GED technique to laser generated rescattering electrons is the connection between the differential cross section of a molecule and the photoelectron spectrum. This can be found in quantitative rescattering theory (QRS) [110–112]:

$$D(p_d, \theta) = W(p_r)\sigma(p_r, \theta_r), \quad (6.26)$$

where $D(k, \theta)$ is the photoelectron spectrum, $W(k_r)$ the returning electron wave packet and $\sigma(p_r, \theta_r)$ the differential cross section (DCS).

This formula has some important implications for the whole rescattering process. As shown, the recolliding electrons are independent of the molecule. The electron wave packet can thereby be determined with an arbitrary molecule and just depends on the driving laser, whereas it is separable from the electron-ion rescattering. It is possible to get field-free differential cross sections like the ones in GED, allowing to reconstruct the structure of the molecule:

The relation between the momenta and the angles can be derived from eq. 6.23. For a fixed momentum (p_r) it is thereby possible to obtain the structure of the molecule, where $W(p_r)$ is the momentum distribution of returning wave packet. It is a normalization factor, which is derived from measurements of noble gases and can be found in [113].

To obtain the intensity of the incoming wavepacket according to GED, the angle dependent tunnel ionization following 6.13 has to be taken into account, since the magnitude of the wave packet depends on it. Equation 6.2 for an unaligned molecule thereby becomes [114]:

$$I(\theta) = \left(\sum_{i=1}^N |f_i|^2(s) \right) \int N(\Omega_L) d\Omega_L + \sum_{i=1}^N \sum_{j=1}^N f_i(s) f_j^*(s) \int N(\Omega_L) e^{isr_{ij}} d\Omega_L \quad (6.27)$$

The MCF can then be written as:

$$MCF = \frac{\sum_{i=1}^N \sum_{j=1}^N f_i(s) f_j^*(s) \int N(\Omega_L) e^{isr_{ij}} d\Omega_L}{\sum_{i=1}^N |f_i|^2(s) \int N(\Omega_L) d\Omega_L} \quad (6.28)$$

Please note, that here the coefficient $C^2 I_0 / R^2$ is neglected and $\mathbf{s} = (k, \theta, \varphi)$ is just depending on θ .

6.2.3 Fixed angle broadband electron scattering

According to the relation [102]:

$$s = |\mathbf{s}| = |k_0 - k| = 2k_0 \sin(\theta/2) \quad (6.29)$$

where, $k_0 = p_r$, the momentum transfer can also be varied by the energy of the electrons. In contrast to the GED experiments, the electrons generated by strong laser fields intrinsically exhibit a broad energy bandwidth. Consequently this is an easy pathway for LIED measurements to obtain the structure of the molecule, called FABLES.

To obtain the highest energy range the backscattering geometry is chosen, since it exhibits the biggest momentum transfer range. Furthermore the atomic term in this case shows a smooth behavior, further simplifying the retrieval.

6.2.4 Comparison of the methods and previous work

The difference between GED and ASLIED is the origin of the scattering electrons. The energy of the electrons usually extends to tenth of keV where the energy of the one originating from the recollision process lies on the order of 100-1000 eV. Nevertheless, imaging of the molecules is still possible, since the detected angle in case of LIED is higher than the few (10°) degree used in a typical GED experiment [102].

As shown in equation 6.29, the limited energy can to some extent be compensated, but still the achievable resolution in LIED is limited, as will also be shown in the results section. Thereby, it is important to mention that according to equation 5.1 it is necessary for high values of U_p to use long wavelengths and high intensities. As already discussed before (chapter 1 and 5), these systems are not widely spread. This problem is probably one of the reasons, why the usage of the LIED techniques was not common in the literature until now.

ASLIED has so far been applied in a proof-of-principle experiment to nitrogen and oxygen [27], later on to acetylene [115] and very recently to benzene [116]. The first experiment is especially interesting because another important feature

of ASLIED was shown in this study: by changing the wavelength of the driving laser, the authors were able to retrieve time dependent informations on the molecules. Since there is a time delay between the ionization of the molecule and the recollision of the electron as emphasized by equation 6.15, the ion can undergo a structural change in between. Furthermore, the time is dependent on the driving wavelength and thereby controlling it gives access to informations of the structural change upon ionization. The study therefore also showed the power of ASLIED to obtain time dependent information, which is impossible with GED. It is worth mentioning, that those changes were on a sub-Ångström scale with femtosecond precision. A different approach was chosen in [117]. In a Cold Target Recoil Ion Momentum Spectroscopy (Coltrims) type experiment, it was possible to directly observe the dissociation of acetylene, depending on the alignment with respect to laser field.

In comparison to those experiments, the reports of FABLES is even more limited in the literature. Besides the first experiment again on nitrogen [28], only oxygen and acetylene [118] have been investigated. This is also a result of the even higher demands on the laser system. Although only a single emission angle has to be investigated the stability of the laser has to be even better, as it will also be shown in the present work.

6.3 Buckminsterfullerene C₆₀

C₆₀ was chosen as sample for several reasons. To investigate the possibilities of the LIED technique it is advantageous that GED data is available for a direct benchmark. The obtained radial distribution is shown in figure 6.3 [119], while data for low energy electrons can be found in [120]. In addition, the cage size is large and the molecule has more atoms than any other molecule investigated with LIED so far.

Besides the experimental advantages, C₆₀ has interesting electronic properties [121–123]. A lot of theoretical investigations as well as experiments have been undertaken in strong-field physics to investigate its behavior in intense fields. The first interesting subject, that can be addressed by C₆₀ are the similarities to atoms and molecules. Since it has an icosahedral symmetry and a defined electronic structure, C₆₀ is comparably easy to investigate theoretically [124]. This makes an ideal model for studying many-electron effects. Furthermore, it can

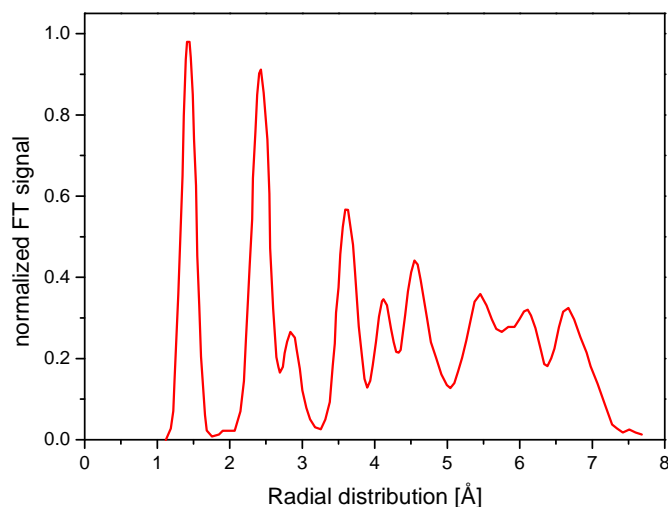


Figure 6.3: Radial distribution of C₆₀, obtained by GED. The graph is taken from [119].

be seen as a prototype molecule for a whole class of nanomaterials, which hold promise to be used in broad variety of applications [125–127].

Especially in the beginning of this century, several experiments tried to understand the behavior of C₆₀ in strong electric fields: According to the Keldysh theory, it was found that for short wavelengths (up to 800 nm) and low intensities, the molecule shows only single and double ionization [128]. With increasing intensity, higher ionization states are achievable. In addition, fragmentation sets in, where C₂ loss is visible in the mass spectra. At high intensities, this mechanism leads to a saturation with relatively low ionization states. For an overview of some results, see [123] and [129]. Therefore, the results obtained by Bhardwaj et al. draw a lot of attention [130]. It showed, that for a pulse with 1800 nm central wavelength almost no fragmentation but ionization up to C₆₀¹²⁺ was reported.

To understand this change, two different excitation pathways have to be discussed. For short wavelength the so called breathing (*a_g(1)*) mode is excited [131], where the motion is a symmetrical expansion of the whole C₆₀ molecule. The excitation thereby incorporates an excitation of the *t_{1g}* mode (LUMO +1), which can act as a doorway state to excite the breathing mode. This results in an excitation of Rydberg states (see [132, 133]), which lead to the fragmentation reported above. This scheme includes multi-electron excitation and electron-electron interactions.

In contrast to that, the long wavelength behavior is expected to be driven within the single active electron (SAE) picture according to the SMM (chapter 5) [122, 124, 134], although some contribution from multielectron effects is also predicted [135]. Intuitively, the interaction can then be viewed as a "laser-induced dipole force" [130], where the electric field pulls the molecule. Thereby it is expanded in one direction, while getting squeezed in the other one. This corresponds to an excitation of the $h_g(1)$ -mode, which is also called the oblate-prolate motion. The structural changes of C₆₀ have been investigated theoretically [136, 137]:

Upon excitation with a 1800 nm 70 fs pulse C₆₀ stores a lot of vibrational energy in the $h_g(1)$ without fragmentation in accordance to the results discussed above. Thereby, the bond-length between adjacent carbon atoms can be increased up to 2.6 Å, where the equilibrium distance is about 1.45 Å (figure 6.3, [119]). The oscillation period of the $h_g(1)$ -mode is about 120 fs. It is important to note that these calculations also showed a high stability of the cations against decomposition.

6.4 Experimental setup

In the beginning of the measurements were undertaken in collaboration with the group of Prof. Louis DiMauro from the Ohio State University (Columbus) where an already existing laser system was used [101]. Later on, an improved version was built within the collaboration:

The system is based on a commercial Ti:Sa amplifier (Spitfire Ace, Spectra physics, 12 mJ, 80 fs, 800 nm, 1 kHz) system with an additional three-stage, KTA-based OPA. The signal is generated in a sapphire plate and the long wavelength part is afterwards amplified by the fundamental of the Ti-Sa amplifier. The idler of the last amplification stage which had a variable central wavelength at around 3.1–3.6 μm is used as the laser source for the experiment. The pulse energy in the experiment was around 200 μJ with a pulse duration of about 100 fs. The polarization direction was controlled with a $\lambda/2$ waveplate. The beam was then focused by a lens into the vacuum chamber.

The experimental setup is similar to the one described in chapter 5. The main difference is the oven which effusively evaporates the C₆₀ into the vacuum. The first one was replaced by a new version, which was able to heat the sample up to 600°C. Furthermore, the distance to the interaction region was optimized leading to higher target density. The TOF and detection method was kept as described

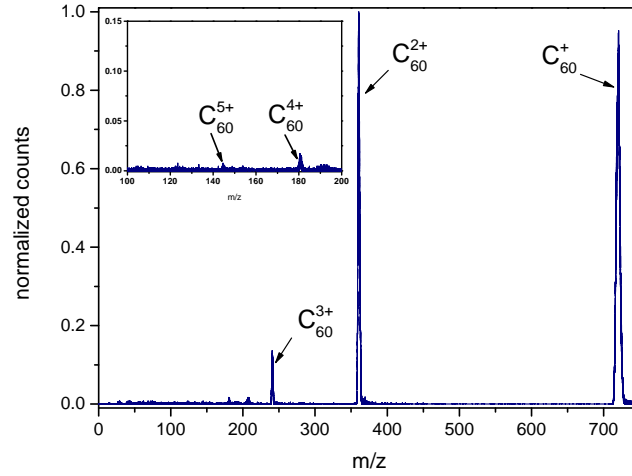


Figure 6.4: Typical mass spectrum of C_{60} obtained before the measurement.

in [101]: The detection system after the drift tube is based on two microchannel plates in Chevron configuration, followed by a conical anode. The acceptance angle of this TOF is further reduced with an iris in front of the MCPs. The detection system uses a TDC (2228A, LeCroy) with a time resolution down to 50 ps.

The OPA was operated at 3.6 μm and the peak intensities were kept on the level of around 80 TW/cm^2 . The mass spectra were thereby similar to the ones in [138], as shown in figure 6.4. Please note, that the ionization shouldn't have a significant effect on the imaging [136].

6.5 Results

6.5.1 Angular resolved laser induced electron diffraction

The measurements for ASLIED were performed by changing the polarization angle by 2° in a randomized fashion to exclude beam drifts. The obtained 2D-momentum is shown in figure 6.5, where the maximal detected momentum was 8.4 au, corresponding to 10 U_p . Therefore the achievable rescattering energy ($3.17 U_p$) is about 300 eV. From this plot, several angle dependent DCS can be extracted, as depicted in figure 6.6 for angles above 35° . Lower angles are neglected due to the contribution of direct electrons, which start to overlay the rescattered ones. All of the plots show unique dependences, which can be attributed to the

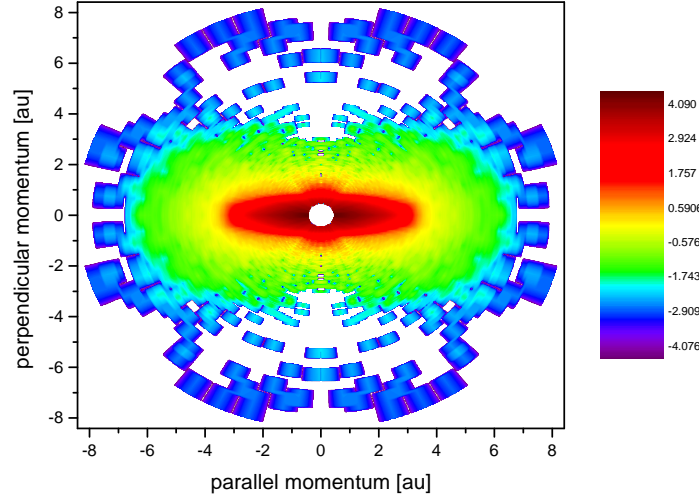


Figure 6.5: 2D momentum plot for C_{60} at $3.6 \mu\text{m}$ and $80 \text{ TW}/\text{cm}^2$. Courtesy of Dr. Junliang Xu.

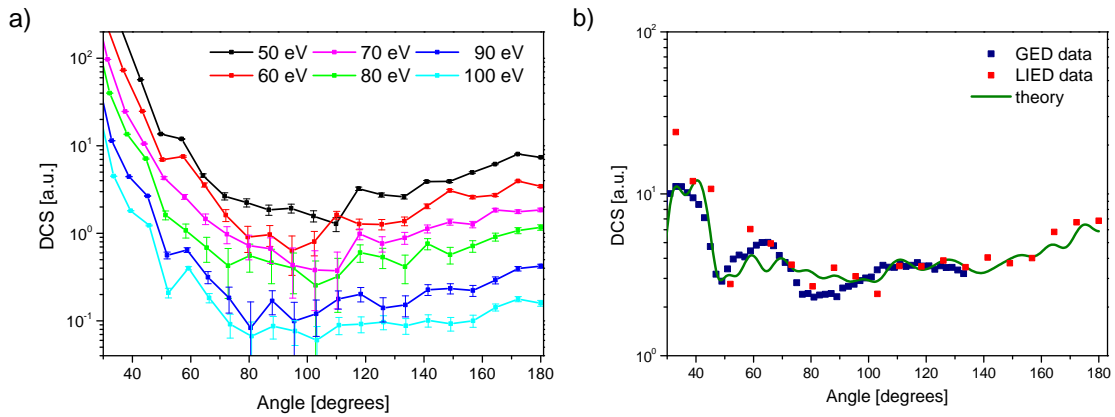


Figure 6.6: Angular dependent DCS for ASLIED. In a) the distribution for different energies is shown. The different dependences can be attributed to the structural information. In b) the DCS for 100 eV is compared to theory to the GED at low energies. Data and graphs are reproduced from [120]. The different imaging angles are a result of the different techniques, as discussed in 6.2.4. Courtesy of Dr. Junliang Xu/ Dr. Cosmin Blaga.

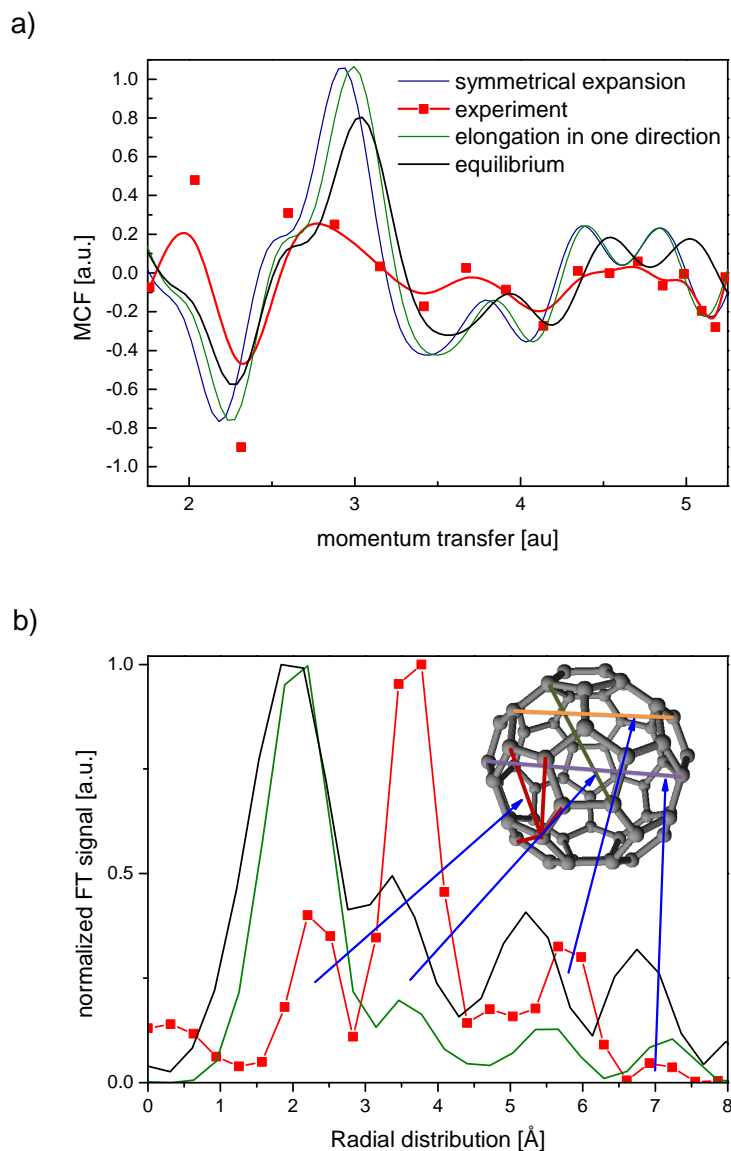


Figure 6.7: Results for ASLIED at 100eV. In a) the MCF in dependence of the momentum transfer in atomic units is shown. The experimental data points are connected with an eye guiding b-spline (red). The results are compared to the theoretical predictions for the cage in equilibrium (black), a symmetrical expanded cage ($g(1)$ -mode, blue) and the prolated cage ($h_g(1)$ -mode, green). In b) the corresponding radial distributions are depicted. Furthermore, the detected peaks are assigned to some atomic distances in the molecule. Please note, that only the position of the peaks and not their amplitude is important. Courtesy of Dr. Junliang Xu.

structure of the C₆₀. Nevertheless, only the distributions above 60 eV were investigated in detail, because they have the highest momentum transfer range. As shown for 100 eV in figure 6.6b), the results are in good agreement to the experimental data and theoretical calculations undertaken with GED at low energies, proving the reliability of the results [120]. The corresponding experimental MCF in figure 6.7 is compared to several theoretical ones, belonging to the molecule in equilibrium, a symmetrically expanded and a prolated one. All of them are in good agreement to the experimental MCF, which is reproducing their main features. Although all of them are similar, the best fit corresponds to the last elongated cage with an expansion of 6%. This can also be seen in the radial distribution, where the peak corresponding to the cage size fits better to the deformed cage. Thereby it is unlikely that the ionization itself is the reason for this change, because one would expect a symmetric deformation, since the charge can be expected to be delocalized.

Besides the cage size, also the other peaks obtained in the radial distribution fit nicely to the elongated cage, distinguishing four different bond classes. The resolution isn't as good as in the GED case, where most of the bonds were distinguishable. For the other energies (60-90 eV) a similar behavior is observed and the elongation is around $5(\pm 3)\%$ as shown in figure 6.8.

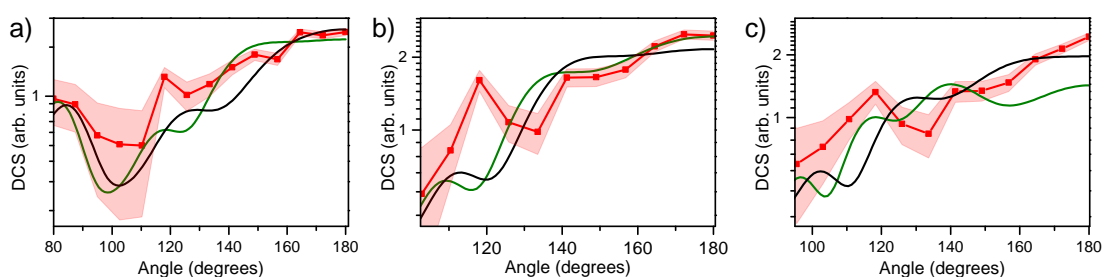


Figure 6.8: DCS for ASLIED at a) 70 eV b) 80 eV and 90 eV. The experimental data (red) is compared to equilibrium cage (black) and the elongated one (green). The obtained values are $(6\pm 2)\%$, $(3\pm 2)\%$, and $(7\pm 2)\%$, respectively. Courtesy of Dr. Cosmin Blaga.

6.5.2 Fixed-angle broadband laser-driven electron scattering

To verify those results, FABLES was applied to C_{60} . In contrast to the measurements for ASLIED the count rate with the first laser system was too low, to get reliable results. Therefore more pulse energy and a higher target density were needed which was achieved with the new oven and the second OPCPA (6.4).

As shown in figure 6.9, even with the new setup the retrieval of the structure is difficult. The most important point within the retrieval of FABLES is the correct smoothing of the data before Fourier-transformation. High frequencies are filtered out by smoothing. It leads to a loss of information at high values in the radial distribution, which are of special interest in the present analysis. Nevertheless, smoothing is necessary for the suppression of artifacts in the TOF-measurement. This can be visualized in the momentum transfer, where a five point moving average was applied (figure 6.9), which basically acts like a low-pass filter as described above.

Anyway, within the retrieval of the radial distribution it was found, that the peak at around 7 \AA is persistent for a broad range of parameters, without a significant change in the position. This is not only true for the averaging (3-5 points), but also for different cropping ranges (different overall momentum transfer ranges). An important feature, implemented in the program used in the analysis shown here, is the weighting based on the number of the counts for each bin. The bins at high energies, with high statistical errors are less weighted. In the picture shown here, a range from 2.17 to $9.3 U_p$ was chosen. As discussed above, similar results were obtained for example with four point averaging and a range 2.19 - $9.8 U_p$. Like in the ASLIED measurements the interference fringes reproduce the theoretical model for an elongated cage quite well. This is also confirmed by the radial distribution. Like before, four peaks can be distinguished, which have basically the same position as in the ASLIED measurement. The change in the molecular size varies for different parameters by about 6-9% in comparison to the equilibrium case, which is in good agreement to the ASLIED results. An analysis done by Dr. Junliang Xu revealed similar results with an increase of 8-9 %

It is important to mention, that the results obtained with FABLES are less reliable than the ones from the ASLIED analysis. This is also shown in the lower plot, where the obtained radial distribution is shown together with an error analysis. The statistics of the measurement are not good enough to draw any final conclu-

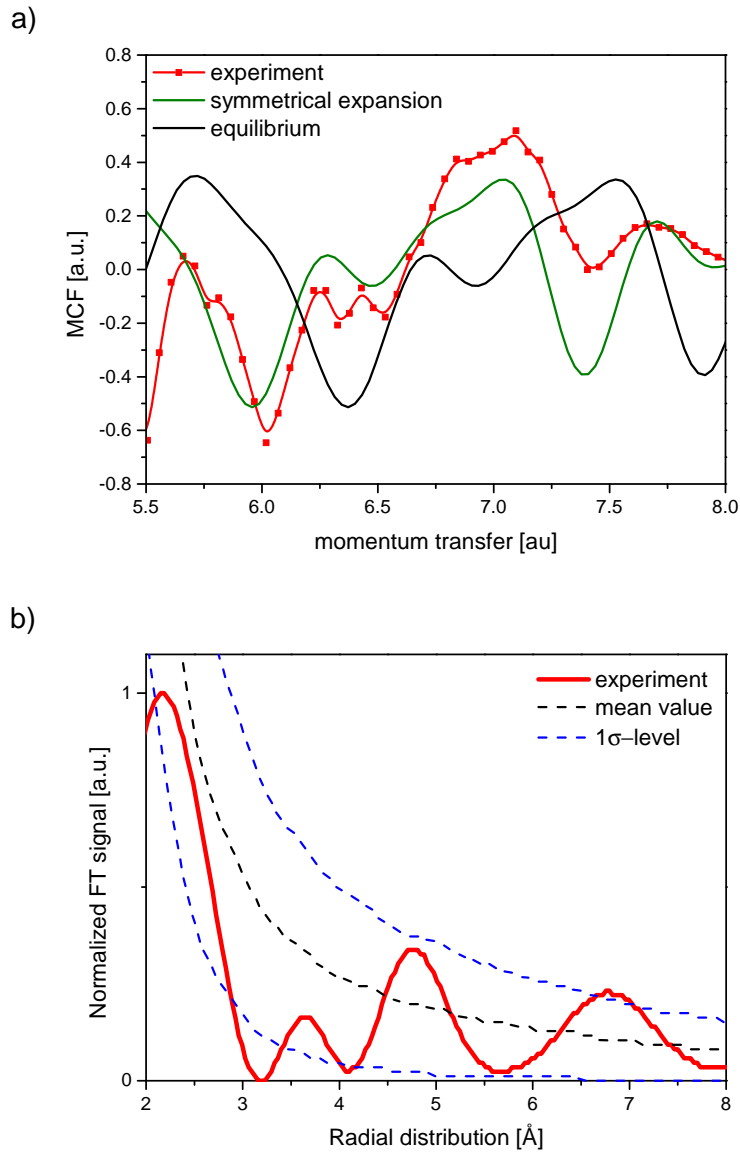


Figure 6.9: Results for FABLES. On the top the experimental momentum transfer (blue) is plotted together with the theoretical curve for an 8% increased cage size in one direction (green) and the equilibrium cage (black). The experimental radial distribution is shown with the retrieved mean-values in b). More details about the retrieval can be found in the text.

sions. Especially the peaks located below the one corresponding to the overall cage size are not even reaching the 1σ confidence level (blue dashed lines).

6.5.3 Dynamics

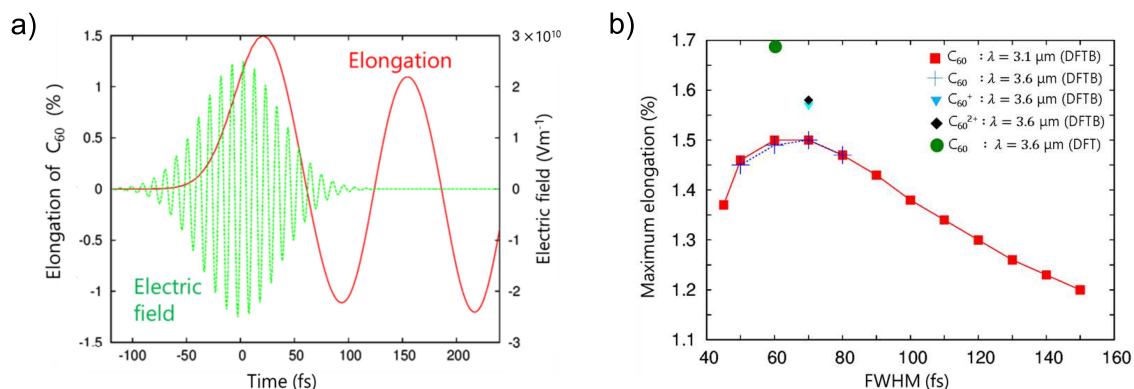


Figure 6.10: Theoretical results of the C_{60} deformation in the laser field for the SCC-DFTB method (mio-1-1 parameter set) at a peak intensity $I_0 = 84 \text{ TW/cm}^2$. a) The temporal profile for the elongation of neutral C_{60} in a 60 fs, $3.1 \mu\text{m}$ Gaussian pulse (green line). b) Maximum elongation of the neutral C_{60} for different pulse durations. In addition the results for different wavelength and the charged C_{60}^{z+} ($z=1,2$) are shown. Furthermore a result evaluated by B3LYP/6-31G(d) of DFT is presented (green circle).

The results obtained from both experiments, ASLIED and FABLES, prove an increase in the cage size of the molecule, which can be explained within the framework of the theoretical predictions, as discussed in [136]. A detailed theoretical analysis by Prof. Kono from the Tohoku University (Sendai) using density functional theory (DFT) on both the standard B3LYP/6-31G(d) level and the self-consistent charge density-functional based tight-binding (SCC-DFTB) semi-empirical method in combination with the standard mio-1-1 C-C parameter set revealed more details of the process.

Both methods show an elongation of the molecule in good agreement to each other that oscillates with a picosecond lifetime. Due to the strong electromagnetic field of the laser pulse the C_{60} cage is prolated in one direction. As shown in figure 6.10 the deformation reaches its maximum shortly (~ 20 fs) after the peak of the laser pulse at $t = 20$ fs, close to the time where the recollision events in the LIED techniques take place (~ 9 fs). This contradicts a fully adiabatic process, which would lead to an overlap between the maxima of the pulse envelope and

the C₆₀ elongation. This can at least qualitatively be understood by an vibrational impulsive Raman excitation [137, 139]. As described in the literature, for short pulse durations, the change of the pulse envelope becomes too short for a fully adiabatic process. The energy is non-adiabatically transferred to the molecule, where a maximal elongation of the molecule is reached after the peak of the laser pulse. This process leads to a maximal deformation for $\approx T_{h_g(1)}/2$ corresponding to about 60-70 fs. This behavior is shown on the right side of figure 6.10. However, the effect of the pulse duration on the deformation is small. The same applies to the ionization state of the molecule which is important since single and double-ionized C₆₀ is present in the experiment (figure 6.4).

The calculated elongation of 1.3-1.4% for 84 TW/cm² is smaller compared to the experimental data. The reason for the deviation can most likely be found in the experiment. Due to the long wavelength an exact characterization of the driving pulse is difficult. The intensity of the pulse used for the calculations was determined by the $2U_p$ cutoff. This method is not very exact since the $2U_p$ cutoff is usually not well defined and therefore leads to a significant error. The intensity has an important influence on the deformation (at an intensity of ~ 340 TW/cm² an increase of about 7% was calculated). In addition pre-pulses cannot be excluded which could have an important influence on the deformation.

6.6 Discussion

The investigation of C₆₀ with ASLIED and FABLES has extended the application of these techniques in several ways. First of all the molecular size has been extended far beyond previous work. Until now the largest molecule under observation was benzene (C₆H₆), which has only been observed with ASLIED. For FABLES the change is even more dramatic, where acetylene (C₂H₂) is the largest molecule successfully investigated so far. Furthermore, it has been proven that both methods are capable of providing interesting insights into the molecular dynamics of molecules with high temporal and spatial resolution. Thereby it is complementary to other UED techniques, which are limited to denser targets. This work thereby opens the way for the investigation of other more complex molecules. The next step in the investigations will be a pump-probe measurement to show the applicability as full 4D method, which will be discussed in chapter 7.

Besides the results obtained here the work has also shown the importance of high repetition rate sources with high pulse energies at long wavelength, like the one

built in this thesis. The data acquisition time was on the order of days, which was only possible due to excellent laser stability. Nevertheless this is too long for pump-probe experiments, which would be the ultimate goal in the future. A better laser source is also important for the FABLES measurement, where the results are not reliable because of the relatively low statistics. This is important since the FABLES technique is simpler to implement. It doesn't rely on the theoretical modeling with the IAM, which in the literature has recently been discussed to be insufficient, especially for small atoms like hydrogen [118].

7 Upgrades and applications of the laser system

The laser system presented here, can be seen as a platform, which allows for different types of improvements. Since only a small fraction of the Innoslab amplifier power is used until now (about 30 W uncompressed), several developments are imaginable, which aim for different laser parameters and take advantage of the complete power. These ideas will be introduced in the first part. Corresponding to that, different types of experiments are in the pipeline based on the ones presented in the chapters 5 and 6.

7.1 Upgrades of the laser system

The maximal average output power of the Innoslab amplifier is 500 W, corresponding to 5 mJ pulse energy at 100 kHz. After compression, this yields about 3.3 mJ with the present compressor. This value could still be further optimized with bigger gratings to optimize the incidence angle, leading to lower diffraction losses.

7.1.1 Towards high energies

The most straight forward way of improving the system is an increase of the pulse energies. In contrast to other OPCPAs, where two crystals are used for amplification, this is possible even within a single stage. Based on the assumptions above and incorporating about 0.3 mJ for the seed generation, 3 mJ are still available for the final stage. Together with the 3 mm BBO crystal used before and proper beam sizes of 1.1 mm (FWHM), a pulse energy of 280 μJ can be achieved. The intensity is higher than before with about 130 GW/cm^2 , but still way below the measured damage threshold of the BBO around 760 GW/cm^2 , as proven by some material tests. The only difference in comparison to the low energy OPCPA is an elevation

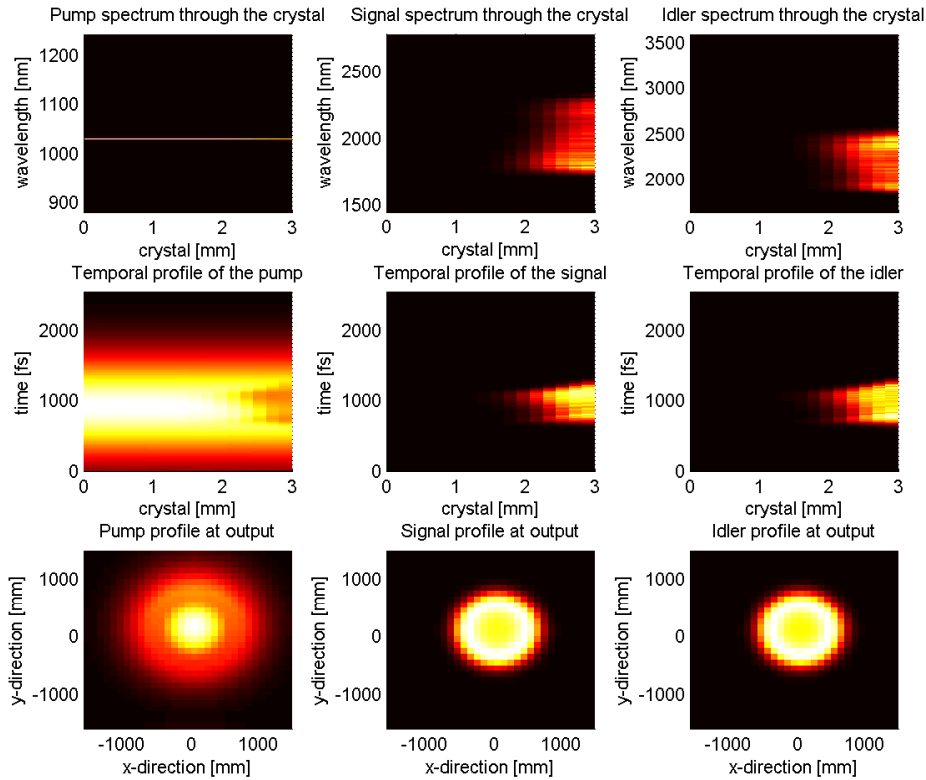


Figure 7.1: Simulation of a final OPCPA stage with a 3 mm BBO-crystal. The retrieved output energy of the signal yielded 280 μJ . The parameters are the same as in chapter 4, except for the beam sizes, which are in both cases 1.1 mm and the energy of the pump beam (3 mJ). Its intensity is thereby set to 130 GW/cm^2 , which has been tested to be far away from the damage threshold of the BBO crystal.

of the long wavelengths in the spectrum, as shown in figure 7.1. In a first attempt, this has already been tried with 1 mJ pump energy. There, an energy of about 100 μJ was achievable, as expected by additional simulations, not shown. The main difficulty with the high average powers is the idler absorption in BBO. This led to the destruction of the crystal at higher powers due to heating. A solution for this problem might be lithium niobate (LNB), which has less absorption in that spectral region. It has also the advantage of being able to amplify an even broader spectrum. Nevertheless, one has to take into account, that LNB suffers from the photorefractive effect at high intensities [140]. The low intensities achievable in LNB are compensated by the higher nonlinear coefficient, which is twice as high as in BBO. That's why the simulations predict, that a pulse energy of up to 380 μJ for LNB is achievable with a 3 mm crystal and an intensity of 65 GW/cm^2 .

7.1.2 Towards high repetition rates

Another possibility is an increase of the repetition rate. In the present laser setup, this can be done by an adjustable divider in the electronics of the fiber amplifier, which controls the first AOM for pulse picking. The fiber amplifier is constructed to be operated with up to 1 MHz. This repetition rate can also be used together with the Innoslab amplifier, which was anyways constructed for higher repetition rates [52]. Actually, it is even more stable in this operation mode, since the inversion within the Yb:YAG crystal is removed more frequently. This also suppresses parasitic effects and lowers the intensity in the cavity.

The OPCPA itself should in principle easily be adopted to higher repetition rates. Therefore, one can expect similar pulse parameters in comparison to the ones reported in this thesis. By just increasing the repetition rate ten times, a compressed average power of about 200 W would have to be used. The excess energy can then be used for a higher amplification, similar to the stage shown in the previous section.

One of the possibly limiting factors for increasing the repetition rates is the heating of the YAG-crystal used for SCG. As shown in figure 3.6, already at 100 kHz a significant elevation in temperature is present. Therefore it is likely, that the crystal cannot withstand a tenfold increase in power. Beam distortions can be expected to appear in the beam profile. A possible way to overcome this problem, is the usage of a cross-polarized wave generation (XPW) stage before SCG [56]. This would lead to a broadening of the spectrum by a factor of $\sqrt{3}$, resulting in a pulse duration of about 650 fs. Using such shortened pulses, the pulse energy needed to obtain a stable white light is reduced, so that the thermal load on the YAG-crystal can be reduced [75].

The main drawback of this approach is the low efficiency of the overall process, which is on the order of 10%. Hence, a bigger portion of the overall pulse energy is needed to obtain the supercontinuum, also reducing the efficiency of the whole setup. Since it is a third order process it also quite sensitive to fluctuations. It could be an alternative to find a compromise between repetition rate and pulse energy to avoid these complications.

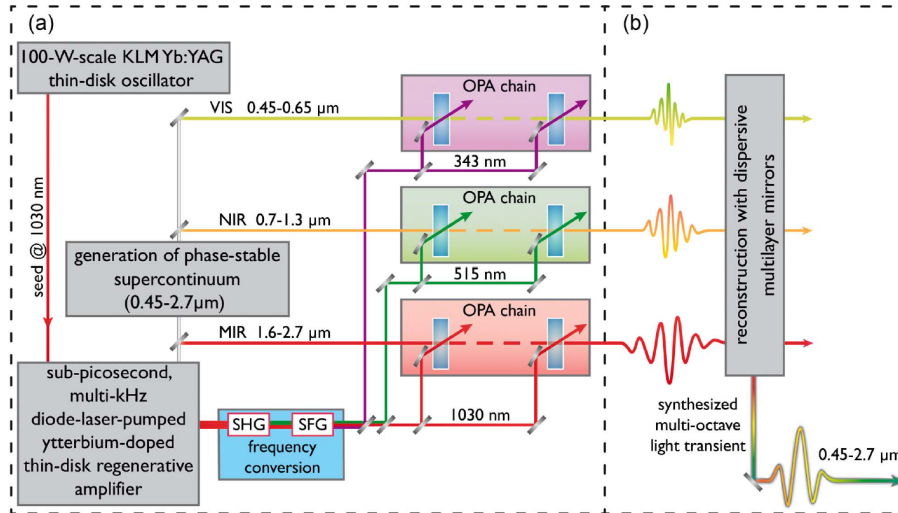


Figure 7.2: Scheme of a multichannel OPCPA, taken from [33]. A broadband seed is split into three parts. Afterwards each channel is independently amplified with different pump wavelength. In the end the outputs are recombined to produce an ultra broadband pulse.

7.1.3 Towards shorter pulse durations

Another possible direction for the future development is a reduction of the pulse duration. One possibility has already been discussed by the use of XPW to further broaden the spectrum. With two stages, it should be possible to decrease the pulse duration significantly. Of course, this comes at the cost of pulse energy as reported before. Nevertheless, an interesting approach would be to use the pulses generated in the present OPCPA, broaden the pulses with XPW, and afterwards amplify them further in LNB.

A more complex way is the usage of an additional amplification chain. The principle is shown in figure 7.2. In this case, the seed is split into several parts and amplified separately in different channels [141]. Afterwards they are recombined, leading to a broad spectrum with very short pulses. This idea can be easily implemented by frequency doubling or even tripling of the mIR pulses and amplification of each channel independently.

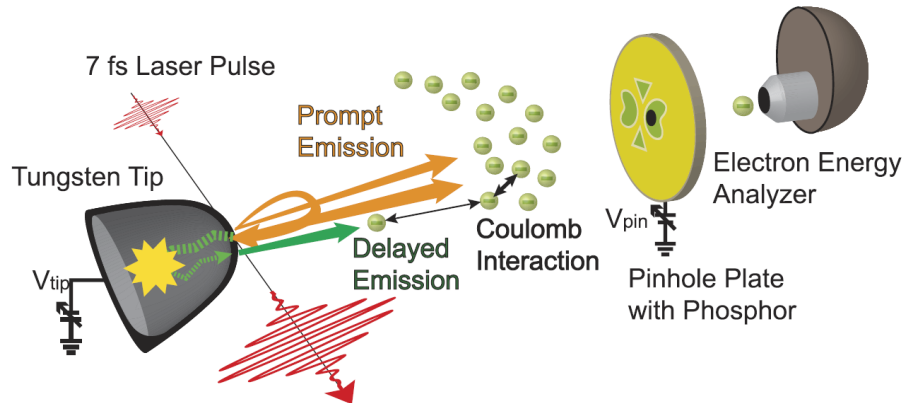


Figure 7.3: Scheme of the delayed emission experiment taken from [145]. A voltage is applied to the tungsten tip, allowing to observe the delayed emission of electrons after laser excitation.

7.2 Experiments

As shown by the experiments in this thesis, the laser system offers different opportunities for improvements due to its unique pulse parameters. Most important is of course the high repetition rate, making it an ideal tool for measurements which require high statistics. am

7.2.1 Nanostructures

In case of the nanotips, the advantage of the long wavelengths has already been shown in a first experiment. Here, not the high pulse energies, but rather the long wavelengths are of special interest. Nevertheless, it should be noted, that the high pulse energies can still be beneficial in these experiments, as they offer the opportunity to shorten the pulse by XPW. It should be possible to build up to 2 stages, with which it could be possible to reach the single cycle regime.

Besides that, due to the development of the system, more systematic investigations can now be undertaken. The nanotips can be measured with high CEP stability, which gives another degree of control in the experiment. As reported in [95] for 800 nm pulses, the nanotips show a strong CEP dependence in the tunneling regime. This region can easily be reached with the new laser system offering the possibility to work at even lower Keldysh parameters. Similar experiments can also be done for different targets, for example nanowires and nanospheres [142–144].

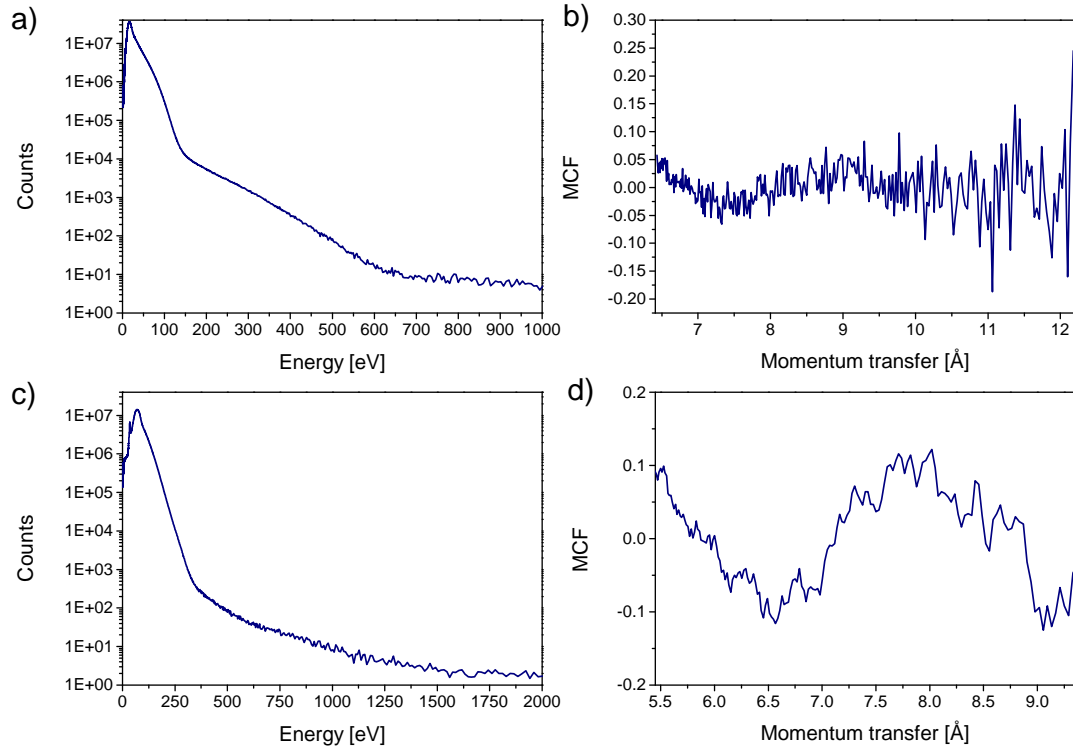


Figure 7.4: Results of the LIED pump-probe measurements. The top row shows a) the photoelectron spectrum and the b) the MCF for C_{60} . The corresponding spectra for N_2 are shown in c) and d). Here the MCF is shown with 9 point averaging.

Another interesting experiment with nanotips was presented by Yanagisawa et al. [145], who measured the time delayed emission, originating from electrons that enter the nanotips at recollision. One portion of them is scattered inside the tips and remitted after some time, leading to a characteristic emission, as depicted in figure 7.3. The main difference to the experiment in this thesis is the applied voltage, which can easily be implemented in the experimental setup.

For higher wavelengths, the electrons can be expected to show a different pathway in the tip, due to higher return energies. This could even suppress the delayed emission, if the electrons are pushed too deep into the tip. Furthermore, these investigations can be done in dependence of the CEP, which should also have an effect on the tips.

7.2.2 Pump-LIED probe experiments

The first results have shown, that LIED is able to image C_{60} with high spatial and time information. The next step would be to show the structural changes in a pump-probe measurement. This has already been tried in collaboration with the group of Prof. Jens Biegert at ICFO, Barcelona. Their 160 kHz system is able to deliver about 15 μJ on target at 3.2 μm [34]. The apparatus was based on a TOF-spectrometer similar to the one reported in 5. During the campaign no oscillations within the rescattered electrons, which encode the structural information, were found in a first Fables measurement of C_{60} , as shown in figure 7.4, even for static measurements without pump. Interestingly, the similar results were obtained by a measurement undertaken with nitrogen, where only a small signal was present, which is in addition dependent on the fitting parameters. Besides that, as reported before [28], a modulation depth of 20% should be visible, while only 10% is present in the current study. High fluctuations in the measurement are visible, as shown in the C_{60} data. For N_2 this can be accounted by a strong averaging, which is impossible for C_{60} . It would vanish the high frequencies, that encode the long distances in the radial distribution, as discussed in 6.5.2, making it impossible to retrieve the structure.

Most probable, the reason for the failure of the experiment has to be found in the apparatus. The main difference between the Ohio and Barcelona experiments is the pulse energy of the driving laser. Since the intensity was kept on the same level as in the experiments in Ohio, it can be attributed to the focusing conditions of the beam, which was consequently much tighter. As the rescattering angle is of great importance for the measurement, this could have led to an averaging effect over a larger angle range, which leads to a smearing effect of the fringes. This was probably also enhanced by a difference within the detection system, where in Ohio an iris was placed in front of the detector, further decreasing the acceptance angle of the TOF. Hence, higher pulse energies are needed to detect the interference fringes, which could in principle be done with the high energy output of the system shown here, which also has a sufficient repetition rate for pump-probe measurements. The drawback of our laser system is the comparably short wavelength, which is probably only sufficient for ASLIED experiments. Nevertheless, it also has some advantages, which cannot be quantified at the moment. Firstly, the system exhibits a comparably short pulse duration reducing the needed pulse energy for a given intensity. This reduces the focusing requirements and

especially for pump-probe experiments, leads to an excellent temporal resolution. Secondly, it allows to control the CEP, which hasn't been done so far in this kind of experiments. As shown for the tips, the electron yield is highly determined by the phase of the electric field, so that control should lead to better statistics, compared to the phase averaged measurements shown here. As a pump beam, one can use a small fraction of the 2 μm beam. For short wavelength it can be frequency doubled or tripled. This also allows to access the second regime around 400 nm, where the $a_g(1)$ mode is excited (for details see chapter 6.3).

8 Conclusions

In the first part of this thesis, a simple and robust scheme for a high power, high repetition rate, few-cycle, and CEP stable OPCPA in the mid-IR has been demonstrated, based on a cutting-edge laser amplifier. It is an all optical approach utilizing only a single laser amplifier output.

In chapter 2 the development of the Innoslab based amplifier laser chain is described, being a powerful laser source at 100 kHz. It produces stable short laser pulses around 1 ps with 1030 nm central wavelength with an energy of up to 5 mJ (uncompressed). A central point within this thesis was the development of a reliable seed generation, circumventing common difficulties in OPCPA design. Therefore, the possibilities of utilizing supercontinuum generation with comparably long laser pulses were experimentally studied. The results prove, that the generated white light is stable on short and long time scales, which is the key requirement for the following parametric stages. Consequently, it was used for broadband amplification in BBO with a frequency doubled fraction of the fundamental beam of the 1030 nm amplifier. The good efficiency of this stage, together with the results of the following DFG stage, shows the potential of generating the seed for OPCPA with our approach. The DFG stability is on the same level as the Innoslab amplifier and the spectrum supports few-cycle pulses. The generated pulses were compressible close to the Fourier limit and the pulse energy was sufficient for OPCPA seeding.

To show the applicability of the generated seed, a single amplifier stage was built. In the present setup 140 μ J pump energy were used, leading to more than 10 μ J output energy. The pulses could be compressed with a mixture of chirped mirrors and sapphire, with an efficiency of about 90%. As shown theoretically, the dispersion can be used to optimize the pulse duration for an optimal overlap between pump and seed. This allows to apply the scheme also to other amplifier systems and removes the necessity of using AOPDFs, while keeping the compression close to the Fourier limit as shown in the present case. In this thesis, a compression down to 15.5 fs was achieved, which could further be optimized by varying the

materials used for stretching and compression. The OPCPA stage also allowed to measure the CEP stability precisely. Here, a value of 103 mrad on short time scales could be achieved, while it increases to 136 mrad on longer time scales. The latter value was only obtainable with an active stabilization, which could be implemented with a slow-loop control. It is based on a piezo-driven mirror, which significantly improved the stability.

Since the current setup uses only a fraction of the Innoslab amplifiers power, the output pulses can be further amplified. In a first attempt, which is not part of this thesis, 100 μJ could be achieved in BBO, in accordance to the theoretical investigations accompanying the experimental development. Therefore it is important to note, that only a single stage is needed to make use of the full power. A further increase in power was limited by the idler absorption of the BBO. As investigated theoretically here, solutions for this problem are available for the future development, which can also include increased repetition rates and shorter pulse durations.

The importance of such a laser is shown in the second part of the thesis. In a first gas experiment, the compressed output pulses of the DFG were used to show its applicability. Here, the expected ATI peaks were observable, leading to further investigations with nanotips. Due to its long wavelength, the OPA showed the potential to investigate the photoemission of electrons in the transition region between multiphoton and tunneling regime. Already with the weak, not CEP-stabilized pulses new insights into the influence of the nearfield of the tip on the emission process could be gained.

In contrast, the LIED experiment shows the limitations of current laser systems, which are operating at low repetition rates. Nevertheless, in the work of the thesis the range of molecules that can be investigated could be advanced. The buckminsterfullerene C_{60} studied here is the biggest molecule probed with ASLIED and FABLES. Among others, it is also interesting for strong-field physics, due to its unique structural and electronic properties. The experiment could verify theoretical investigations, which predicted a prolongation of the molecule in the laser field. Especially the ability of investigating the structural deformation of C_{60} and the dynamics of other molecules give rise to future developments of these techniques. It should be possible to directly observe the dynamics in a pump-probe measurement. Current high repetition rate systems, like the one used in this thesis, cannot provide enough pulse energy, which further underlines the importance of new laser sources.

Bibliography

- [1] T. H. Maimann. “Stimulated Optical Radiation in Ruby”. *Nature* 187 (1960), pp. 493–494.
- [2] M. Hentschel, R. Kienberger, C. Spielmann, G. A. Reider, N. Milosevic, T. Brabec, P. Corkum, U. Heinzmann, M. Drescher, and F. Krausz. “Attosecond metrology”. *Nature* 414 (2001), pp. 509–513.
- [3] P. B. Corkum and F. Krausz. “Attosecond science”. *Nature Physics* 3 (2007), pp. 381–387.
- [4] M. D. Perry, D. Pennington, B. C. Stuart, G. Tietbohl, J. A. Britten, C. Brown, S. Herman, B. Golick, M. Kartz, J. Miller, H. T. Powell, M. Vergino, and V. Yanovsky. “Petawatt laser pulses”. *Optics Letters* 24 (1999), pp. 160–162.
- [5] C. Danson, D. Hillier, N. Hopps, and D. Neely. “Petawatt class lasers worldwide”. *High Power Laser Science and Engineering* 3 (2015), e3.
- [6] M. Fermann, A. Gavanauskas, and G. Sucha. *Ultrafast Lasers: Technology and Applications*. Boca Raton and Florence: C R C Press LLC and Taylor & Francis Group [distributor], 2002.
- [7] J. F. Ready. *Industrial applications of lasers*. Academic press, 1997.
- [8] C. V. Shank and E. P. Ippen. “Subpicosecond kilowatt pulses from a mode-locked cw dye laser”. *Applied Physics Letters* 24 (1974), pp. 373–375.
- [9] A. H. Zewail. “Femtochemistry: Atomic-Scale Dynamics of the Chemical Bond †”. *The Journal of Physical Chemistry A* 104 (2000), pp. 5660–5694.
- [10] *Press Release: The 1999 Nobel Prize in Chemistry*. URL: http://www.nobelprize.org/nobel_prizes/chemistry/laureates/1999/press.html.
- [11] P. F. Moulton. “Spectroscopic and laser characteristics of Ti:Al₂O₃”. *Journal of the Optical Society of America B* 3 (1986), pp. 125–133.
- [12] D. E. Spence, P. N. Kean, and W. Sibbett. “60-fsec pulse generation from a self-mode-locked Ti: Sapphire laser”. *Optics Letters* 16 (1991), pp. 42–44.

- [13] D. Strickland and G. Mourou. "Compression of amplified chirped optical pulses". *Optics Communications* 56 (1985), pp. 219–221.
- [14] M. Ossiander, F. Siegrist, V. Shirvanyan, R. Pazourek, A. Sommer, T. Latka, A. Guggenmos, S. Nagele, J. Feist, J. Burgdörfer, R. Kienberger, and M. Schultze. "Attosecond correlation dynamics". *Nature Physics* 13 (2016), pp. 280–285.
- [15] N. H. Burnett, H. A. Baldis, M. C. Richardson, and G. D. Enright. "Harmonic generation in CO₂ laser target interaction". *Applied Physics Letters* 31 (1977), pp. 172–174.
- [16] L'Huillier and Balcou. "High-order harmonic generation in rare gases with a 1-ps 1053-nm laser". *Physical Review Letters* 70 (1993), pp. 774–777.
- [17] M. Lewenstein, P. Balcou, M. Y. Ivanov, A. L'Huillier, and P. B. Corkum. "Theory of high-harmonic generation by low-frequency laser fields". *Physical Review A* 49 (1994), pp. 2117–2132.
- [18] P. M. Paul, E. S. Toma, P. Breger, G. Mullot, F. Auge, P. Balcou, H. G. Muller, and P. Agostini. "Observation of a train of attosecond pulses from high harmonic generation". *Science* 292 (2001), pp. 1689–1692.
- [19] R. Kienberger, M. Hentschel, M. Uiberacker, C. Spielmann, M. Kitzler, A. Scrinzi, M. Wieland, T. Westerwalbesloh, U. Kleineberg, U. Heinzmann, M. Drescher, and F. Krausz. "Steering attosecond electron wave packets with light". *Science (New York, N.Y.)* 297 (2002), pp. 1144–1148.
- [20] M. F. Kling, C. Siedschlag, A. J. Verhoef, J. I. Khan, M. Schultze, T. Uphues, Y. Ni, M. Uiberacker, M. Drescher, F. Krausz, and M. J. J. Vrakking. "Control of electron localization in molecular dissociation". *Science (New York, N.Y.)* 312 (2006), pp. 246–248.
- [21] F. Krausz and M. Ivanov. "Attosecond physics". *Reviews of Modern Physics* 81 (2009), pp. 163–234.
- [22] P. Corkum. "Plasma perspective on strong field multiphoton ionization". *Physical Review Letters* 71 (1993), pp. 1994–1997.
- [23] M. F. Hommelhoff Peter; Kling. *Attosecond nanophysics: From basic science to applications*. Ed. by P. Hommelhoff and M. F. Kling. Weinheim: Wiley-VCH, 2015.

- [24] T. Fennel, K.-H. Meiwes-Broer, J. Tiggesbäumker, P.-G. Reinhard, P. M. Dinh, and E. Suraud. “Laser-driven nonlinear cluster dynamics”. *Reviews of Modern Physics* 82 (2010), pp. 1793–1842.
- [25] “Attosecond physics at the nanoscale”. *Reports on Progress in Physics* 80 (2017), p. 054401.
- [26] H. Mark and R. Wierl. “Über Elektronenbeugung am einzelnen Molekül”. *Die Naturwissenschaften* 18 (1930), pp. 205–205.
- [27] C. I. Blaga, J. Xu, A. D. DiChiara, E. Sistrunk, K. Zhang, P. Agostini, T. A. Miller, L. F. DiMauro, and C. D. Lin. “Imaging ultrafast molecular dynamics with laser-induced electron diffraction”. *Nature* 483 (2012), pp. 194–197.
- [28] J. Xu, C. I. Blaga, K. Zhang, Y. H. Lai, C. D. Lin, T. A. Miller, P. Agostini, and L. F. DiMauro. “Diffraction using laser-driven broadband electron wave packets”. *Nature communications* 5 (2014), p. 4635.
- [29] H. R. Telle, G. Steinmeyer, A. E. Dunlop, J. Stenger, D. H. Sutter, and U. Keller. “Carrier-envelope offset phase control: A novel concept for absolute optical frequency measurement and ultrashort pulse generation”. *Applied Physics B* 69 (1999), pp. 327–332.
- [30] D. J. Jones. “Carrier-Envelope Phase Control of Femtosecond Mode-Locked Lasers and Direct Optical Frequency Synthesis”. *Science* 288 (2000), pp. 635–639.
- [31] A. Apolonski, A. Poppe, G. Tempea, C. Spielmann, T. Udem, R. Holzwarth, T. W. Hänsch, and F. Krausz. “Controlling the Phase Evolution of Few-Cycle Light Pulses”. *Physical Review Letters* 85 (2000), pp. 740–743.
- [32] *Press Release: The 2005 Nobel Prize in Physics*. URL: https://www.nobelprize.org/nobel_prizes/physics/laureates/2005/press.html.
- [33] H. Fattahi, H. G. Barros, M. Gorjan, T. Nubbemeyer, B. Alsaif, C. Y. Teisset, M. Schultze, S. Prinz, M. Haefner, M. Ueffing, A. Alismail, L. Vámos, A. Schwarz, O. Pronin, J. Brons, X. T. Geng, G. Arisholm, M. Ciappina, V. S. Yakovlev, D.-E. Kim, A. M. Azzeer, N. Karpowicz, D. Sutter, Z. Major, T. Metzger, and F. Krausz. “Third-generation femtosecond technology”. *Optica* 1 (2014), pp. 45–63.

- [34] M. Baudisch, H. Pires, H. Ishizuki, T. Taira, M. Hemmer, and J. Biegert. “Sub-4-optical-cycle, 340 MW peak power, high stability mid-IR source at 160 kHz”. *Journal of Optics* 17 (2015), p. 094002.
- [35] M. Baudisch, B. Wolter, M. Pullen, M. Hemmer, and J. Biegert. “High power multi-color OPCPA source with simultaneous femtosecond deep-UV to mid-IR outputs”. *Optics Letters* 41 (2016), pp. 3583–3586.
- [36] N. Thire, R. Maksimenka, B. Kiss, C. Ferchaud, P. Bizouard, E. Cormier, K. Osvay, and N. Forget. “4-W, 100-kHz, few-cycle mid-infrared source with sub-100-mrad carrier-envelope phase noise”. *Optics Express* 25 (2017), pp. 1505–1514.
- [37] C. Homann, M. Bradler, M. Förster, P. Hommelhoff, and E. Riedle. “Carrier-envelope phase stable sub-two-cycle pulses tunable around 1.8 μm at 100 kHz”. *Optics Letters* 37 (2012), pp. 1673–1675.
- [38] C.-J. Lai, K.-H. Hong, J. P. Siqueira, P. Krogen, C.-L. Chang, G. J. Stein, H. Liang, P. D. Keathley, G. Laurent, J. Moses, L. E. Zapata, and F. X. Kärtner. “Multi-mJ mid-infrared kHz OPCPA and Yb-doped pump lasers for tabletop coherent soft x-ray generation”. *Journal of Optics* 17 (2015), p. 094009.
- [39] Y. Deng, A. Schwarz, H. Fattahi, M. Ueffing, X. Gu, M. Ossiander, T. Metzger, V. Pervak, H. Ishizuki, T. Taira, T. Kobayashi, G. Marcus, F. Krausz, R. Kienberger, and N. Karpowicz. “Carrier-envelope-phase-stable, 1.2 mJ, 1.5 cycle laser pulses at 2.1 μm ”. *Optics Letters* 37 (2012), pp. 4973–4975.
- [40] H. Fattahi. “Yb:YAG-Pumped, Few-Cycle Optical Parametric Amplifiers”. *High Energy and Short Pulse Lasers*. Ed. by R. Viskup. InTech, 2016.
- [41] M. Muller, M. Kienel, A. Klenke, T. Gottschall, E. Shestaev, M. Plotner, J. Limpert, and A. Tunnermann. “1 kW 1 mJ eight-channel ultrafast fiber laser”. *Optics Letters* 41 (2016), pp. 3439–3442.
- [42] P. Russbueltdt, T. Mans, J. Weitenberg, H. D. Hoffmann, and R. Poprawe. “Compact diode-pumped 1.1 kW Yb:YAG Innoslab femtosecond amplifier”. *Optics Letters* 35 (2010), pp. 4169–4171.
- [43] T. Nubbemeyer, M. Kaumanns, M. Ueffing, M. Gorjan, A. Alismail, H. Fattahi, J. Brons, O. Pronin, H. G. Barros, Z. Major, T. Metzger, D. Sutter, and F. Krausz. “1 kW, 200 mJ picosecond thin-disk laser system”. *Optics Letters* 42 (2017), pp. 1381–1384.

- [44] M. Kienel, M. Muller, A. Klenke, J. Limpert, and A. Tunnermann. “12 mJ kW-class ultrafast fiber laser system using multidimensional coherent pulse addition”. *Optics Letters* 41 (2016), pp. 3343–3346.
- [45] I. Ahmad. “Development of an optically synchronized seed source for a high-power few-cycle OPCPA system”. PhD thesis. Ludwig-Maximilians-Universität München, 2011.
- [46] T. Metzger. “High-repetition-rate picosecond pump laser based on an Yb:YAG disk amplifier for optical parametric amplification”. PhD thesis. Technische Universität Berlin, 2009.
- [47] J.-C. Diels and W. Rudolph. *Ultrashort Laser Pulse Phenomena: Fundamentals, Techniques, and Applications on a Femtosecond Time Scale (Optics and Photonics)*. Academic Press, 2006.
- [48] E. Treacy. “Optical pulse compression with diffraction gratings”. *IEEE Journal of Quantum Electronics* 5 (1969), pp. 454–458.
- [49] O. Martinez. “3000 times grating compressor with positive group velocity dispersion: Application to fiber compensation in 1.3–1.6 μm region”. *IEEE Journal of Quantum Electronics* 23 (1987), pp. 59–64.
- [50] S. Karsch. “Generation of high-intensity laser pulses, Lecture notes”. unpublished.
- [51] P. Russbueldt, D. Hoffmann, M. Hofer, J. Lohring, J. Luttmann, A. Meissner, J. Weitenberg, M. Traub, T. Sartorius, D. Esser, R. Wester, P. Loosen, and R. Poprawe. “Innoslab Amplifiers”. *IEEE Journal of Selected Topics in Quantum Electronics* 21 (2015), pp. 447–463.
- [52] P. Russbueldt, T. Mans, G. Rotarius, J. Weitenberg, H. D. Hoffmann, and R. Poprawe. “400W Yb: YAG Innoslab fs-Amplifier”. *Optics Express* 17 (2009), pp. 12230–12245.
- [53] A. Schwarz, M. Ueffing, Y. Deng, X. Gu, H. Fattahi, T. Metzger, M. Os- siander, F. Krausz, and R. Kienberger. “Active stabilization for optically synchronized optical parametric chirped pulse amplification”. *Optics Ex- press* 20 (2012), pp. 5557–5565.
- [54] R. Riedel, M. Schulz, M. J. Prandolini, A. Hage, H. Höppner, T. Gottschall, J. Limpert, M. Drescher, and F. Tavella. “Long-term stabilization of high power optical parametric chirped-pulse amplifiers”. *Optics Express* 21 (2013), pp. 28987–28999.

- [55] N. Minkovski, S. M. Saltiel, G. I. Petrov, O. Albert, and J. Etchepare. "Polarization rotation induced by cascaded third-order processes". *Optics Letters* 27 (2002), pp. 2025–2027.
- [56] T. Buberl, A. Alismail, H. Wang, N. Karpowicz, and H. Fattahi. "Self-compressed, spectral broadening of a Yb:YAG thin-disk amplifier". *Optics Express* 24 (2016), pp. 10286–10294.
- [57] C. Erny, L. Gallmann, and U. Keller. "High-repetition-rate femtosecond optical parametric chirped-pulse amplifier in the mid-infrared". *Applied Physics B* 96 (2009), pp. 257–269.
- [58] R. Riedel, A. Stephanides, M. J. Prandolini, B. Gronloh, B. Jungbluth, T. Mans, and F. Tavella. "Power scaling of supercontinuum seeded megahertz-repetition rate optical parametric chirped pulse amplifiers". *Optics Letters* 39 (2014), pp. 1422–1424.
- [59] M. Puppín, Y. Deng, O. Prochnow, J. Ahrens, T. Binhammer, U. Morgner, M. Krenz, M. Wolf, and R. Ernstorfer. "500 kHz OPCPA delivering tunable sub-20 fs pulses with 15 W average power based on an all-ytterbium laser". *Optics Express* 23 (2015), pp. 1491–1497.
- [60] J. Rothhardt, S. Demmler, S. Hädrich, J. Limpert, and A. Tünnermann. "Octave-spanning OPCPA system delivering CEP-stable few-cycle pulses and 22 W of average power at 1 MHz repetition rate". *Optics Express* 20 (2012), pp. 10870–10878.
- [61] M. Schultze, T. Binhammer, G. Palmer, M. Emons, T. Lang, and U. Morgner. "Multi- μ J, CEP-stabilized, two-cycle pulses from an OPCPA system with up to 500 kHz repetition rate". *Optics Express* 18 (2010), pp. 27291–27297.
- [62] P. Rigaud, A. van de Walle, M. Hanna, N. Forget, F. Guichard, Y. Zaouter, K. Guesmi, F. Druon, and P. Georges. "Supercontinuum-seeded few-cycle mid-infrared OPCPA system". *Optics Express* 24 (2016), pp. 26494–26502.
- [63] M. Bradler. "Bulk continuum generation: The ultimate tool for laser applications and spectroscopy". PhD thesis. München: Ludwig-Maximilians-Universität München, 2014.
- [64] J. H. Marburger. "Self-focusing: Theory". *Progress in Quantum Electronics* 4 (1975), pp. 35–110.
- [65] A. Couairon and A. MYSYROWICZ. "Femtosecond filamentation in transparent media". *Physics Reports* 441 (2007), pp. 47–189.

- [66] P. Chernev and V. Petrov. "Self-focusing of light pulses in the presence of normal group-velocity dispersion". *Optics Letters* 17 (1992), pp. 172–174.
- [67] J. E. Rothenberg. "Space–time focusing: Breakdown of the slowly varying envelope approximation in the self-focusing of femtosecond pulses". *Optics Letters* 17 (1992), pp. 1340–1342.
- [68] A. Brodeur, C. Y. Chien, F. A. Ilkov, S. L. Chin, O. G. Kosareva, and V. P. Kandidov. "Moving focus in the propagation of ultrashort laser pulses in air". *Optics Letters* 22 (1997), pp. 304–306.
- [69] S. Uhlig. *Self-organized surface structures with ultrafast white-light: First investigation of LIPSS with supercontinuum*. BestMasters. Wiesbaden: Springer Spektrum, 2015.
- [70] G. P. Agrawal. *Nonlinear fiber optics*. 5. ed. Amsterdam [u.a.]: Elsevier/Acad. Press, 2013.
- [71] J. E. Rothenberg. "Pulse splitting during self-focusing in normally dispersive media". *Optics Letters* 17 (1992), pp. 583–585.
- [72] D. Faccio, A. Averchi, A. Couairon, M. Kolesik, J. V. Moloney, A. Dubietis, G. Tamosauskas, P. Polesana, A. Piskarskas, and P. Di Trapani. "Spatio-temporal reshaping and X Wave dynamics in optical filaments". *Optics Express* 15 (2007), pp. 13077–13095.
- [73] M. Kolesik, E. M. Wright, and J. V. Moloney. "Interpretation of the spectrally resolved far field of femtosecond pulses propagating in bulk nonlinear dispersive media". *Optics Express* 13 (2005), pp. 10729–10741.
- [74] D. Faccio, A. Averchi, A. Lotti, M. Kolesik, J. V. Moloney, A. Couairon, and P. Di Trapani. "Generation and control of extreme blueshifted continuum peaks in optical Kerr media". *Physical Review A* 78 (2008), p. 033825.
- [75] M. Bradler, P. Baum, and E. Riedle. "Femtosecond continuum generation in bulk laser host materials with sub- μ J pump pulses". *Applied Physics B* 97 (2009), pp. 561–574.
- [76] A.-L. Calendron, H. Cankaya, G. Cirmi, and F. X. Kartner. "White-light generation with sub-ps pulses". *Optics Express* 23 (2015), pp. 13866–13879.
- [77] R. W. Boyd. *Nonlinear optics*. 3rd ed. Amsterdam and Boston: Academic Press, 2008.

- [78] G. Cerullo and S. de Silvestri. “Ultrafast optical parametric amplifiers”. *Review of Scientific Instruments* 74 (2003), pp. 1–18.
- [79] Christian Homann. “Optical parametric processes to the extreme: From new insights in first principles to tunability over more than 4 octaves”. PhD thesis. München: Ludwig-Maximilians-Universität München, 2013.
- [80] G. Arisholm. “General numerical methods for simulating second-order nonlinear interactions in birefringent media”. *Journal of the Optical Society of America B* 14 (1997), pp. 2543–2549.
- [81] G. Arisholm. “Quantum noise initiation and macroscopic fluctuations in optical parametric oscillators”. *Journal of the Optical Society of America B* 16 (1999), pp. 117–127.
- [82] D. Zhang, Y. Kong, and J.-y. Zhang. “Optical parametric properties of 532-nm-pumped beta-barium-borate near the infrared absorption edge”. *Optics Communications* 184 (2000), pp. 485–491.
- [83] D. E. Zelmon, D. L. Small, and D. Jundt. “Infrared corrected Sellmeier coefficients for congruently grown lithium niobate and 5 mol% magnesium oxide –doped lithium niobate”. *Journal of the Optical Society of America B* 14 (1997), pp. 3319–3322.
- [84] A. Shirakawa, I. Sakane, and T. Kobayashi. “Pulse-front-matched optical parametric amplification for sub-10-fs pulse generation tunable in the visible and near infrared”. *Optics Letters* 23 (1998), pp. 1292–1294.
- [85] *refractive index*. URL: <https://refractiveindex.info>.
- [86] A. Comin, R. Ciesielski, G. Piredda, K. Donkers, and A. Hartschuh. “Compression of ultrashort laser pulses via gated multiphoton intrapulse interference phase scans”. *Journal of the Optical Society of America B* 31 (2014), pp. 1118–1125.
- [87] V. V. Lozovoy, I. Pastirk, and M. Dantus. “Multiphoton intrapulse interference IV Ultrashort laser pulse spectral phase characterization and compensation”. *Optics Letters* 29 (2004), pp. 775–777.
- [88] A. Baltuška, T. Fuji, and T. Kobayashi. “Controlling the Carrier-Envelope Phase of Ultrashort Light Pulses with Optical Parametric Amplifiers”. *Physical Review Letters* 88 (2002), p. 133901.

- [89] G. Cerullo, A. Baltuška, O. D. Mücke, and C. Vozzi. “Few-optical-cycle light pulses with passive carrier-envelope phase stabilization”. *Laser & Photonics Reviews* 5 (2011), pp. 323–351.
- [90] S. Hadrich, J. Rothhardt, M. Krebs, S. Demmler, J. Limpert, and A. Tunnermann. “Improving carrier-envelope phase stability in optical parametric chirped-pulse amplifiers by control of timing jitter”. *Optics Letters* 37 (2012), pp. 4910–4912.
- [91] R. Budriūnas, T. Stanislauskas, J. Adamonis, A. Aleknavičius, G. Veitas, D. Gadonas, S. Balickas, A. Michailovas, and A. Varanavičius. “53 W average power CEP-stabilized OPCPA system delivering 55 TW few cycle pulses at 1 kHz repetition rate”. *Optics Express* 25 (2017), pp. 5797–5806.
- [92] A. Thai, M. Hemmer, P. K. Bates, O. Chalus, and J. Biegert. “Sub-250-mrad, passively carrier-envelope-phase-stable mid-infrared OPCPA source at high repetition rate”. *Optics Letters* 36 (2011), pp. 3918–3920.
- [93] N. Ishii, K. Kaneshima, K. Kitano, T. Kanai, S. Watanabe, and J. Itatani. “Sub-two-cycle, carrier-envelope phase-stable, intense optical pulses at 1.6 μm from a BiB₃O₆ optical parametric chirped-pulse amplifier”. *Optics Letters* 37 (2012), pp. 4182–4184.
- [94] M. Neuhaus. “Generation of passively CEP stable pulses at high repetition rates for strong-field photoionization”. Master thesis. München: Ludwig-Maximilians-Universität München, 2016.
- [95] S. Mitra. “Strong-field photoemission dynamics from metallic nanostructures”. Master thesis. Karlsruhe Institute of Technology, 2016.
- [96] N. B. Delone and V. P. Krainov. *Multiphoton Processes in Atoms*. Second Enlarged and Updated Edition. Vol. 13. Springer Series on Atoms+Plasmas. Berlin, Heidelberg: Springer Berlin Heidelberg, 2000.
- [97] Z. Chang. *Fundamentals of attosecond optics*. Boca Raton: CRC Press, 2011.
- [98] F. V. Bunkin and M. V. Fedorov. “Cold emission of electrons from the surface of a metal in a strong radiation field”. *Soviet Physics—Journal of Experimental and Theoretical Physics* 21 (1965), pp. 896–899.
- [99] M. Krüger. “Attosecond physics in strong-field photoemission from metal nanotips”. PhD thesis. Ludwig-Maximilians-Universität München, 2013.

- [100] G. Herink, D. R. Solli, M. Gulde, and C. Ropers. “Field-driven photoemission from nanostructures quenches the quiver motion”. *Nature* 483 (2012), pp. 190–193.
- [101] U. B. Szafruga. “Wavelength Dependent Strong Field Interactions with Atoms and Molecules”. PhD thesis. The Ohio State University, 2015.
- [102] I. Hargittai and M. Hargittai. *Stereochemical Applications of Gas-Phase Electron Diffraction, Part A*. John Wiley & Sons, 1988.
- [103] A. M. Perelomov, V. S. Popov, and M. V. Terent’ev. “Ionization of atoms in an alternating electric field”. *Soviet Physics—Journal of Experimental and Theoretical Physics* 23 (1966), pp. 924–934.
- [104] M. V. Ammosov, N. B. Delone, V. P. Krainov, A. M. Perelomov, V. S. Popov, M. V. Terent’ev, G. L. Yudin, and M. Y. Ivanov. “Tunnel ionization of complex atoms and of atomic ions in an alternating electric field”. *Soviet Physics—Journal of Experimental and Theoretical Physics* 64 (1986), p. 1191.
- [105] X. M. Tong, Z. X. Zhao, and C. D. Lin. “Theory of molecular tunneling ionization”. *Physical Review A* 66 (2002), p. 033402.
- [106] S.-F. Zhao, C. Jin, A.-T. Le, T. F. Jiang, and C. D. Lin. “Determination of structure parameters in strong-field tunneling ionization theory of molecules”. *Physical Review A* 81 (2010), p. 033423.
- [107] G. G. Paulus, W. Becker, W. Nicklich, and H. Walther. “Rescattering effects in above-threshold ionization: a classical model”. *Journal of Physics B: Atomic, Molecular and Optical Physics* 27 (1994), p. L703.
- [108] K. Zhang. “Atomic and Molecular dynamics in intense mid-infrared fields”. PhD thesis. The Ohio State University, 2015.
- [109] C. I. Blaga. “Atoms and Molecules in Strong Midinfrared Laser Fields”. PhD thesis. New York: Stony Brook University, 2009.
- [110] Z. Chen, A.-T. Le, T. Morishita, and C. D. Lin. “Quantitative rescattering theory for laser-induced high-energy plateau photoelectron spectra”. *Physical Review A* 79 (2009), p. 033409.
- [111] C. D. Lin, A.-T. Le, Z. Chen, T. Morishita, and R. Lucchese. “Strong-field rescattering physics—self-imaging of a molecule by its own electrons”. *Journal of Physics B: Atomic, Molecular and Optical Physics* 43 (2010), p. 122001.

- [112] Z. Chen, A.-T. Le, T. Morishita, and C. D. Lin. "Origin of species dependence of high-energy plateau photoelectron spectra". *Journal of Physics B: Atomic, Molecular and Optical Physics* 42 (2009), p. 061001.
- [113] J. Xu, C. I. Blaga, A. D. DiChiara, E. Sistrunk, K. Zhang, Z. Chen, A.-T. Le, T. Morishita, C. D. Lin, P. Agostini, and L. F. DiMauro. "Laser-Induced Electron Diffraction for Probing Rare Gas Atoms". *Physical Review Letters* 109 (2012), p. 233002.
- [114] J. Xu, Z. Chen, A.-T. Le, and C. D. Lin. "Self-imaging of molecules from diffraction spectra by laser-induced rescattering electrons". *Physical Review A* 82 (2010), p. 033403.
- [115] M. G. Pullen, B. Wolter, A.-T. Le, M. Baudisch, M. Hemmer, A. Senftleben, C. D. Schröter, J. Ullrich, R. Moshhammer, C. D. Lin, and J. Biegert. "Imaging an aligned polyatomic molecule with laser-induced electron diffraction". *Nature Communications* 6 (2015), p. 7262.
- [116] Y. Ito, C. Wang, A.-T. Le, M. Okunishi, D. Ding, C. D. Lin, and K. Ueda. "Extracting conformational structure information of benzene molecules via laser-induced electron diffraction". *Structural dynamics (Melville, N.Y.)* 3 (2016), p. 034303.
- [117] B. Wolter, M. G. Pullen, A.-T. Le, M. Baudisch, K. Doblhoff-Dier, A. Senftleben, M. Hemmer, C. D. Schroter, J. Ullrich, T. Pfeifer, R. Moshhammer, S. Grafe, O. Vendrell, C. D. Lin, and J. Biegert. "Ultrafast electron diffraction imaging of bond breaking in di-ionized acetylene". *Science (New York, N.Y.)* 354 (2016), pp. 308–312.
- [118] M. G. Pullen, B. Wolter, A.-T. Le, M. Baudisch, M. Sclafani, H. Pires, C. D. Schroter, J. Ullrich, R. Moshhammer, T. Pfeifer, C. D. Lin, and J. Biegert. "Influence of orbital symmetry on diffraction imaging with rescattering electron wave packets". *Nature communications* 7 (2016), p. 11922.
- [119] K. Hedberg, L. Hedberg, D. S. Bethune, C. A. Brown, H. C. Dorn, R. D. Johnson, and M. de Vries. "Bond lengths in free molecules of buckminsterfullerene, C₆₀, from gas-phase electron diffraction". *Science (New York, N.Y.)* 254 (1991), pp. 410–412.
- [120] L. R. Hargreaves, B. Lohmann, C. Winstead, and V. McKoy. "Elastic scattering of intermediate-energy electrons from C₆₀ molecules". *Physical Review A* 82 (2010), p. 062716.

- [121] Y. Huismans, E. Cormier, C. Cauchy, P.-A. Hervieux, G. Gademann, A. Gijbbers, O. Ghafur, P. Johnsson, P. Logman, T. Barillot, C. Bordas, F. Lépine, and M. J. J. Vrakking. “Macro-atom versus many-electron effects in ultrafast ionization of C₆₀”. *Physical Review A* 88 (2013), p. 013201.
- [122] M. Ruggenthaler, S. V. Popruzhenko, and D. Bauer. “Recollision-induced plasmon excitation in strong laser fields”. *Physical Review A* 78 (2008), p. 033413.
- [123] K. Hoffmann. “Femtosecond Laser Spectroscopy of Fullerenes”. PhD thesis. Freie Universität Berlin, 2000.
- [124] A. Jaroń-Becker, A. Becker, and F. H. M. Faisal. “Single-active-electron ionization of C₆₀ in intense laser pulses to high charge states”. *Journal of chemical physics* 126 (2007), p. 124310.
- [125] L. Maidich, D. Pontiroli, M. Gaboardi, S. Lenti, G. Magnani, G. Riva, P. Carretta, C. Milanese, A. Marini, M. Riccò, and S. Sanna. “Investigation of Li and H dynamics in Li₆C₆₀ and Li₆C₆₀H_y”. *Carbon* 96 (2016), pp. 276–284.
- [126] D. M. Guldi, B. M. Illescas, C. M. Atienza, M. Wielopolski, and N. Martin. “Fullerene for organic electronics”. *Chemical Society Reviews* 38 (2009), pp. 1587–1597.
- [127] C. Trinh, K. O. Kirlikovali, A. N. Bartynski, C. J. Tassone, M. F. Toney, G. F. Burkhard, M. D. McGehee, P. I. Djurovich, and M. E. Thompson. “Efficient energy sensitization of C₆₀ and application to organic photovoltaics”. *Journal of the American Chemical Society* 135 (2013), pp. 11920–11928.
- [128] M. Tchapyguine, K. Hoffmann, O. Dühr, H. Hohmann, G. Korn, H. Rottke, M. Wittmann, I. V. Hertel, and E. E. B. Campbell. “Ionization and fragmentation of C₆₀ with sub-50 fs laser pulses”. *The Journal of chemical physics* 112 (2000), pp. 2781–2789.
- [129] K. Yamanouchi. *Progress in ultrafast intense laser science III*. Vol. vol. 3. Progress in ultrafast intense laser science. Berlin: Springer, 2008.
- [130] V. R. Bhardwaj, P. B. Corkum, and D. M. Rayner. “Internal laser-induced dipole force at work in C₆₀ molecule”. *Physical Review Letters* 91 (2003), p. 203004.

- [131] T. Laarmann, I. Shchatsinin, A. Stalmashonak, M. Boyle, N. Zhavoronkov, J. Handt, R. Schmidt, C. P. Schulz, and I. V. Hertel. "Control of Giant Breathing Motion in C_{60} with Temporally Shaped Laser Pulses". *Physical Review Letters* 98 (2007), p. 058302.
- [132] M. Boyle, M. Hedén, C. P. Schulz, E. E. B. Campbell, and I. V. Hertel. "Two-color pump-probe study and internal-energy dependence of Rydberg-state excitation in C_{60} ". *Physical Review A* 70 (2004), p. 051201.
- [133] H. Li, B. Mignolet, Z. Wang, K. J. Betsch, K. D. Carnes, I. Ben-Itzhak, C. L. Cocke, F. Remacle, and M. F. Kling. "Transition from SAMO to Rydberg State Ionization in C_{60} in Femtosecond Laser Fields". *The Journal of chemical physics* 7 (2016), pp. 4677–4682.
- [134] A. Jaroń-Becker, A. Becker, and F. H. M. Faisal. "Saturated ionization of fullerenes in intense laser fields". *Physical Review Letters* 96 (2006), p. 143006.
- [135] I. Shchatsinin, T. Laarmann, G. Stibenz, G. Steinmeyer, A. Stalmashonak, N. Zhavoronkov, C. P. Schulz, and I. V. Hertel. " C_{60} in intense short pulse laser fields down to 9 fs: excitation on time scales below e-e and e-phonon coupling". *Journal of chemical physics* 125 (2006), p. 194320.
- [136] K. Nakai, H. Kono, Y. Sato, N. Niitsu, R. Sahnoun, M. Tanaka, and Y. Fujimura. "Ab initio molecular dynamics and wavepacket dynamics of highly charged fullerene cations produced with intense near-infrared laser pulses". *Chemical Physics* 338 (2007), pp. 127–134.
- [137] N. Niitsu, M. Kikuchi, H. Ikeda, K. Yamazaki, M. Kanno, H. Kono, K. Mitsuke, M. Toda, and K. Nakai. "Nanosecond simulations of the dynamics of C_{60} excited by intense near-infrared laser pulses: impulsive Raman excitation, rearrangement, and fragmentation". *The Journal of chemical physics* 136 (2012), p. 164304.
- [138] V. R. Bhardwaj, P. B. Corkum, and D. M. Rayner. "Recollision during the High Laser Intensity Ionization of C_{60} ". *Physical Review Letters* 93 (2004), p. 043001.
- [139] X. Zhou, Z. Lin, C. Jiang, M. Gao, and R. E. Allen. "Maximum relative excitation of a specific vibrational mode via optimum laser-pulse duration". *Physical Review B* 82 (2010), p. 075433.

- [140] F. Bach, M. Mero, M.-H. Chou, and V. Petrov. “Laser induced damage studies of LiNbO₃ using 1030-nm, ultrashort pulses at 10-1000 kHz”. *Optical Materials Express* 7 (2017), pp. 240–252.
- [141] A. Wirth, M. T. Hassan, I. Grguras, J. Gagnon, A. Moulet, T. T. Luu, S. Pabst, R. Santra, Z. A. Alahmed, A. M. Azzeer, V. S. Yakovlev, V. Pervak, F. Krausz, and E. Goulielmakis. “Synthesized light transients”. *Science (New York, N.Y.)* 334 (2011), pp. 195–200.
- [142] B. Ahn, J. Schötz, M. Kang, W. A. Okell, S. Mitra, B. Förg, S. Zherebtsov, F. Süßmann, C. Burger, M. Kübel, C. Liu, A. Wirth, E. Di Fabrizio, H. Yanagisawa, D. Kim, B. Kim, and M. F. Kling. “Attosecond-controlled photoemission from metal nanowire tips in the few-electron regime”. *APL Photonics* 2 (2017), p. 036104.
- [143] S. Zherebtsov, T. Fennel, J. Plenge, E. Antonsson, I. Znakovskaya, A. Wirth, O. Herrwerth, F. Süßmann, C. Peltz, I. Ahmad, S. A. Trushin, V. Pervak, S. Karsch, M. J. J. Vrakking, B. Langer, C. Graf, M. I. Stockman, F. Krausz, E. Rühl, and M. F. Kling. “Controlled near-field enhanced electron acceleration from dielectric nanospheres with intense few-cycle laser fields”. *Nature Physics* 7 (2011), pp. 656–662.
- [144] F. Süßmann, L. Seiffert, S. Zherebtsov, V. Mondes, J. Stierle, M. Arbeiter, J. Plenge, P. Rupp, C. Peltz, A. Kessel, S. A. Trushin, B. Ahn, D. Kim, C. Graf, E. Rühl, M. F. Kling, and T. Fennel. “Field propagation-induced directionality of carrier-envelope phase-controlled photoemission from nanospheres”. *Nature Communications* 6 (2015), p. 7944.
- [145] H. Yanagisawa, S. Schnepf, C. Hafner, M. Hengsberger, D. E. Kim, M. F. Kling, A. Landsman, L. Gallmann, and J. Osterwalder. “Delayed electron emission in strong-field driven tunnelling from a metallic nanotip in the multi-electron regime”. *Scientific reports* 6 (2016), p. 35877.

Data Archiving

The data shown in this thesis can be found on the Data Archive Server (DAS) of the laboratory for Attosecond physics located at the Max Planck Institute of Quantum Optics in Garching:

`/afs/rzg/mpq/lap/publication_archive`

Refer to the Readme.txt in the main folder for a detailed description.

List of Author's publications

Journal articles

- P. Wnuk, H. Fuest, M. Neuhaus, L. Lötscher, S. Zherebtsov, E. Riedle, Z. Major, and M. F. Kling. "Discrete dispersion scanning as a simple method for broadband femtosecond pulse characterization." *Optics Express* 24 (2016), p. 18551
- Harald Fuest, Y. H. Lai, C. I. Blaga, S. Kazuma, J. Xu, P. Rupp, H. Li, P. Wnuk, I. Ben-Itzhak, P. Agostini, H. Kono, M. F. Kling, and L. DiMauro. "Deformation of C₆₀ in intense mid-infrared laser fields probed by laser-induced electron diffraction" in preparation
- M. Neuhaus, H. Fuest, J. Schötz, V. Pervak, M. Trubetskov, P. Russbueldt, H. D. Hoffmann, E. Riedle, Z. Major, M. F. Kling, and P. Wnuk. "Two-cycle CEP-stable 2 μ m source based on fiber-laser seeded Innoslab with high repetition rate." in preparation
- J. Schötz, S. Mitra, H. Fuest, M. Neuhaus, W. A. Okell, M. Förster, T. Paschen, H. Yanagisawa, P. Wnuk, P. Hommelhoff, and M. F. Kling. "Non-adiabatic ponderomotive shifts in strong-field photoemission from nanotips." in preparation

Conference contributions

- Imaging of C₆₀ with laser-induced electron diffraction using strong mid-IR laser pulses H. Fuest, Y. H. Lai, J. Xu, P. Rupp, H. Li, C. I. Blaga, L. F. DiMauro, and M. F. Kling International Conference on Ultrafast Phenomena, 2016

Acknowledgments

First of all, I would like to thank my advisor Prof. Kling, for his supervision. I am very grateful for the possibility to develop a complete laser setup and his trust in my scientific, constructional and administrative skills. It was a great pleasure to be part of his group, where my special thanks go to Pawel Wnuk, who taught me so much about OPA development. Similarly, I have to mention Marcel Neuhaus who worked most of the time with me in the lab. The same applies to Johannes Schötz and Sambit Mitra, who did the nanotips experiments for so many long hours with me.

As the work in this thesis was not only done in Munich I especially have to thank Prof. Louis DiMauro at the OSU in Columbus, Ohio and his group for the great environment, they provided for the LIED experiments. Especially the LIED team with Dr. Cosmin Blaga, Dr. Junliang Xu, and Yu Hang (Marco) Lai I have to mention. They worked with me in the lab as well as on the theoretical calculations. Furthermore, I have to thank Prof. Jens Biegert, Matthias Baudisch, Benjamin Wolter and Ugaitz Elu Etxano for the possibility to take pump-probe data with their laser system at ICFO in Barcelona. My first station during my thesis was at the ILT in Aachen, where I learned much about laser amplifiers. Here, I have to thank Dr. Peter Rußbüldt for his supervision and Guido Rotarius and Thomas Sartorius for their help in the lab. I still remember the long days and the hard work in the lab. In addition, I have to thank Johannes Weitenberg, from the ILT, who is also now at MPQ and helped me with the installation of the Innoslab even two times.

For the good start into the work I additionally have to thank Lauryna Lötscher, who was a great help in the beginning, and the other PCs that were involved at that time in the project, namely: Dr. Zsuzsanna Major, Dr. Peter Baum and Dr. Alexander Apolonskiy. Therefore, my special thanks also go to Prof. Krausz, who made the whole work possible.

Besides the scientific personal my special thanks go to the administration of the LMU, with who I had to deal with quite a bit. My special thanks there go to

Katharina Adler and Dr. Martin Groß, with whom I had to solve many problems. Dr. Groß was also important during the "Bauamt-Sitzungen", a word which I guess, everybody knows in my group now. I am so happy that we managed to get a lab built, that is now used by the whole group, leading hopefully to new "cutting-edge" developments. At the end, I also want to thank my wife Johanna and my family, which helped me a lot when I reached some rock bottom during the thesis. I am so glad to have you by my side.